PHYSICAL BOUNDARY AS A SOURCE OF ANOMALIES

IN TRANSPORT PROCESSES IN ACOUSTICS AND ELECTRODYNAMICS

Andrii Bozhko, B.S., M.S.

Dissertation Prepared for the Degree of

DOCTOR OF PHILOSOPHY

UNIVERSITY OF NORTH TEXAS

December 2018

APPROVED:

Arkadii Krokhin, Major Professor
Vladimir Drachev, Committee Member
Yuankun Lin, Committee Member
Arup Neogi, Committee Member
Yuri Rostovtsev, Committee Member
Michael Monticino, Interim Chair of the
    Department of Physics
Su Gao, Dean of the College of Science
Victor Prybutok, Dean of the Toulouse
    Graduate School

# ACKNOWLEDGEMENTS

TABLE OF CONTENTS

# LIST OF TABLES

LIST OF FIGURES

xiii

CHAPTER 1

INTRODUCTION

## 1.1. Light and Sound

Lightning bolts piercing the sky, "magnesian stones" attracting iron shards, echoes reciting actors' words in a theater — millennia ago, these and other mysteries were inspiring mankind to seek answers to the nature of things. Over the time three different domains of knowledge — electricity, magnetism, and acoustics, — emerged to encompass the above-mentioned and a vast number of other similar phenomena. These domains were regarded as totally independent from one another, describing effects of absolutely different physical nature, and it was not until the early XIX century when Ørsted experimentally discovered the deflecting effect of an electric current in a wire on a suspended magnetic needle, thus laying the foundation for a unified electromagnetic theory. Further experiments and investigations unveiled the wave nature of light and established a connection between the propagating compressions and rarefactions of media, i.e., the sound waves, and the electromagnetic radiation.

Nowadays, the similarity between the two only grows, thanks to the studies of how light and sound interact with complex structures, revealing the counterparts of electromagnetic effects in acoustics and vice versa. A good example is the extraordinary transmission of light [21] and sound [58, 23, 16] through subwavelength apertures in a plate which in both cases is enabled by the surface waves squeezing the energy into the openings.

## 1.2. Interfaces between Media

The example of extraordinary transmission brings the question of what role the boundaries between various parts of a physical system play. We all know that boundaries separate regions occupied by different materials, but what does this imply? The existence of surface waves, which are confined to a narrow region along the interface between two media, is the evidence that the boundaries are not just auxiliary elements of a physical system. In fact, they can be treated as individual objects enabling the energy transmission in ways

1

that are impossible to realize inside the bulk. Moreover, on a microscopic level the atoms constituting surface layers of a material are known to have an electronic band structure that is completely different from that of the "bulk" atoms. Such special states of atoms (Shockley [87] or Tamm [93] states) cause the unusual response to the external excitations, which leads to the observation of miscellaneous anomalies in wave propagation close to the surfaces.

## 1.3. Recent Motivations

The past few decades were plentiful with the advances in the areas of nanophotonics and metamaterials. The nanophotonics research explores ways to concentrate electromagnetic fields of optical frequencies within the nanometer-sized structures, i.e., within regions shorter than the wavelength [62], and the metamaterials provide much needed unconventional material properties to assist with that [13]. The prospect of accumulating the energy and thus achieving the unprecedented field enhancement at nanoscale drives the development of optoelectronic devices and near-field imaging and conceives new applications for tumor treatment and solar cell design [2, 3, 84].

Underlying the nanophotonics is the field of plasmonics, which studies the phenomena associated with surface plasmons — electric charge excitations coupled with the electromagnetic field and bound to metallic surfaces. Interaction of light with surface plasmons makes the enhancement of linear and nonlinear optical processes possible [89], however, there is a certain downside to the plasmon-enabled processes [51]. It is known that scaling down the physical system raises the questions of surface plasmon radiation [50, 92] and stability [38]. The latter dissipative effects obviously limit the capabilities of the surface plasmons and ultimately impede the efficiency of the plasmonic devices.

In this work, I will direct my attention to a rather unusual aspect regarding surface plasmons, namely, the idea of the surface itself. The discovery of surface plasmons more than a century ago [62] triggered the rapid growth of plasmonics, yet it may seem as if the concept of an interface between two media froze in time. In theoretical studies the interface along which the surface plasmon propagates is still regarded as an infinitely thin surface or line separating one medium from another. Such status quo has to be reconsidered as one de-

scends into the nanoscale realm, where the atomic and electronic structures of matter start manifesting themselves. This brings me to the textbook problem of the surface plasmon propagation, which needs to be studied now without the approximation of an infinitely thin interface. Instead, a more physical interface — a relatively thin layer where the macroscopic material properties change smoothly — will be incorporated into the problem, and I will examine its implications on the properties of the surface plasmons.

The research problem outlined above does not constitute all of my interest in the topic as the diversity of the effects is beyond imagination. Moreover, numerous phenomena observed and predicted for plasmonic structures motivate the exploration of similar systems in acoustics. With the speed of sound in any material being orders of magnitude smaller than the speed of light, the research returns back to the macroscopic scale, abolishing the need to design the components of the system with the nanometer precision. In particular, the plasmonic-assisted effects of extraordinary optical transmission through subwavelength apertures [21] and energy transfer along the array of nanoparticles [74] connect with the respective effects of anomalous acoustic transmission through a narrow slit in a metal plate and through an array of microperforated shells. Recent experimental results [31, 32] demonstrate peculiar features in the transmission spectra, which arise due to excitation of surface localized waves and thus demand a detailed theoretical analysis.

1.4. Dissertation Description

In this dissertation I study the phenomena that are caused by the interaction of sound or light with the interfaces between media.

The second chapter presents the study of the sound transmission through a fluid-immersed metallic plate with a rectangular channel pierced in it. When the elasticity of solid is included in the picture, the system gains the ability to support elastic surface waves (Rayleigh waves) at the metal-fluid interfaces. In order to calculate the transmission properties of the plates with the channel, I extend the typical approaches used to address the diffraction of sound on a slit and propagation of sound in a waveguide. I introduce the notion of acoustic potentials which are used to derive the dispersion relation for coupled Rayleigh

waves and the transmission coefficient. Also, I discuss how different — propagating and leaky — coupled Rayleigh modes of the channel allow propagation and redirection of sound.

In the third chapter the process in question is the scattering of acoustic waves by a linear chain of weak scattering units, with every unit being a perforated metal sheet rolled into a cylindrical shape. I consider each scatterer in the approximation of effective impedance, and I formulate the scattering problem for the periodic arrangement of perforated shells in cylindrical geometry. Solving the scattering problem yields the transmission spectrum of the chain and the dispersion of the acoustic modes supported by the chain. Analysis of both reveals the correspondence between the strong suppression of sound transmission and the excitation of the chain's eigenmodes. Based on the obtained results, I demonstrate how the system studied can serve as a passive redirecting antenna or a passive splitter of sound.

In the fourth chapter I challenge the used-by-default model of the infinitely thin interface between the two media and look at the implications of employing the more realistic model with continuous transitions of media properties. In particular, I revise the problem of the surface plasmon polariton propagation along metal-dielectric interfaces. I solve Maxwell's equations to obtain the plasmonic dispersion and electromagnetic field and analytically show that this commonly disregarded transition layer between media actually affects the properties of the surface plasmon. Namely, I establish that the plasmon within the transition layer is forced to decay nonradiatively, which adds to the usual Joule dissipation, and derive the respective formulas. I also present numerical simulations of the surface plasmon excitation by a laser beam in Kretschmann and Otto configurations to prove that the spectra of the reflected light are modified when the width of the transition layer is changed.

The final chapter concludes the dissertation, summarizes the work done and explains the results obtained.

CHAPTER 2

REDIRECTION OF SOUND IN A FLUID CHANNEL WITH ELASTIC WALLS VIA
THE RAYLEIGH WAVES

2.1. Introduction

Among the variety of phenomena that may occur at the interface between the two
media, the propagation of surface waves is of particular interest. The key concern of this
chapter is the special type of surface waves that are known as Rayleigh waves. The Rayleigh
waves are the elastic waves that propagate inside the solid medium and are confined to
the region close to its surface. Lord Rayleigh was the first to predict the existence of these
waves in the semi-infinite homogeneous solids and to describe their properties [77]. Since
then, a number of disciplines, such as geophysics and seismology, advanced significantly after
they adopted the concept of the Rayleigh waves.

Below, I will consider the problem of the ultrasound transmission through the narrow
fluid channel formed between two elastic media and show that the elastic surface waves add
qualitatively novel features to the scope.

2.1.1. History of the Problem

The problem of the transmission of sound through narrow apertures has been occu-
pying the researchers' minds for several decades. In the simplest case, where an opening
is punctured in an ideally rigid and infinitesimally thin screen, the behavior of acoustic
waves is dictated by the classical theory of diffraction [88, 52]. In the subsequent stud-
ies [106, 94], the finite thickness of a rigid wall was added into picture, which significantly
altered the pattern of diffracted sound and allowed to observe new resonances in the trans-
mission spectra. These resonances are related to the so-called Fabry-Perot resonances which
originate from the constructive interference of the transmitted and reflected waves bouncing
inside a medium (a phenomenon similar to the thin-film interference in optics). As a re-
sult, when the thickness $d$ of the solid screen is close to an integer of the wavelength of
incoming sound, $d \approx n\lambda$, $n = 1, 2, 3, ...$, the transmission through the slit is resonantly am-

plified. In the case of the subwavelength apertures, the transmission was shown to behave as $T \sim \lambda/d$ for the resonant wavelengths [16]. When arranging a number of slits periodically in the rigid screen, one may achieve an almost 100% transmission of the incident sound [58], which is guided through the openings in a way that resembles that in the phenomenon of the extraordinary optical transmission [21]. Namely, the enhanced transmission is enabled by the excitation of the surface waves on either face of the screen, which are coupled by the Fabry-Perot cavity modes excited inside the slits. It is quite peculiar that the acoustic surface wave still may propagate along the surface that is not perfectly smooth, but rather periodically corrugated [49] or even perforated [16, 109, 41].

The other phenomena that were predicted and observed for sound transmission through the perforated rigid screens are the effective collimation of sound [15, 17, 111] and the ideal reflection of the incident wave [71, 23, 24, 22].

In the latter studies, a rigid screen with a periodic arrangement of holes becomes opaque to the incident sound due to destructive interference between the Fabry-Perot cavity mode and the specific Fourier component of the acoustic field in the fluid which has the wavelength comparable with the perforation period.

### 2.1.2. Rigid-Body Approximation

In all previously described situations, one typically assumes the background to be air. The acoustic interactions between the media are characterized by their characteristic impedances $Z = \rho c$, where $\rho$ is the density and $c$ is the typical speed of sound. The contrast between the impedances of air and metal screen is very high, $Z_{air}/Z_m \approx 10^{-5} \div 10^{-4}$, hence, the solid regions are treated as ideally rigid ($Z_m \to \infty$). In this approximation, the acoustic field does not penetrate the solid, so at the surface of the solid one demands that the normal velocity of the surrounding medium be zero. The pressure of sound in the regions excluding the solid is found by solving the wave equation, which yields the waveguide-type solutions inside the slits. Further expansion of the pressure field over the waveguide modes allows to analytically calculate the transmission properties of the screen. For acoustical applications, this method was demonstrated in [15, 17], and, naturally, its counterpart was proposed for

electrodynamics [69, 34, 91].

### 2.1.3. Phenomena beyond the Rigid-Body Approximation

However, the approximation of an ideally rigid body may not always hold. Even for the air-metal systems with high impedance mismatch, the energy exchange between the media can still be quite effective. This enhancement of acoustic coupling occurs close to the frequencies of the Fabry-Perot resonances of the system. As a result, the vibrations in the elastic solid are synchronized with the oscillations of the fluid and cause the deformation of the channel walls. This wave behavior is similar to a regular propagating Rayleigh wave [103], with a few key distinctions. Namely, the surface wave is not anymore dispersionless like the Rayleigh wave, and the actual dispersion relation becomes nonlinear. Due to that, the wave does not necessarily exhibit the evanescent into the metal behavior and, therefore, can propagate energy at an angle to the interface, resulting in nonzero acoustic flux between the fluid and the metal. Such waves — so-called leaky waves — are similar to quasisurface waves at the solid-fluid interfaces studied in [103, 37, 7]. Also, a recent study [79] of the sound transmission through a glass plate with periodically attached polymer spheres demonstrated how the resonant contribution to the transmission can be due to the leaky (or quasi-guided) elastic modes only.

Increasing the interplay between the media makes the rigid-body approximation invalid. In [31], a system with a low fluid-metal impedance mismatch was experimentally studied. A narrow channel formed between the two metal plates was submerged in water, which reduced the value of $Z_f/Z_m$ to approximately $10^{-2} \div 10^{-1}$. The transmission of sound was experimentally measured for the channel, and the obtained spectra appeared to contain unusual deep minima (see Fig. 2.1). The nature of those minima will be examined in this chapter.

Intuitively, the reason for the emergence of the unexpected minima in Fig. 2.1 has to be the destructive interference of waves that propagate in the channel — the same reason that explains the Fabry-Perot resonances. Of course, the interfering waves must now be the proper eigenmodes of the system, that is, of the channel between the plates. Further,
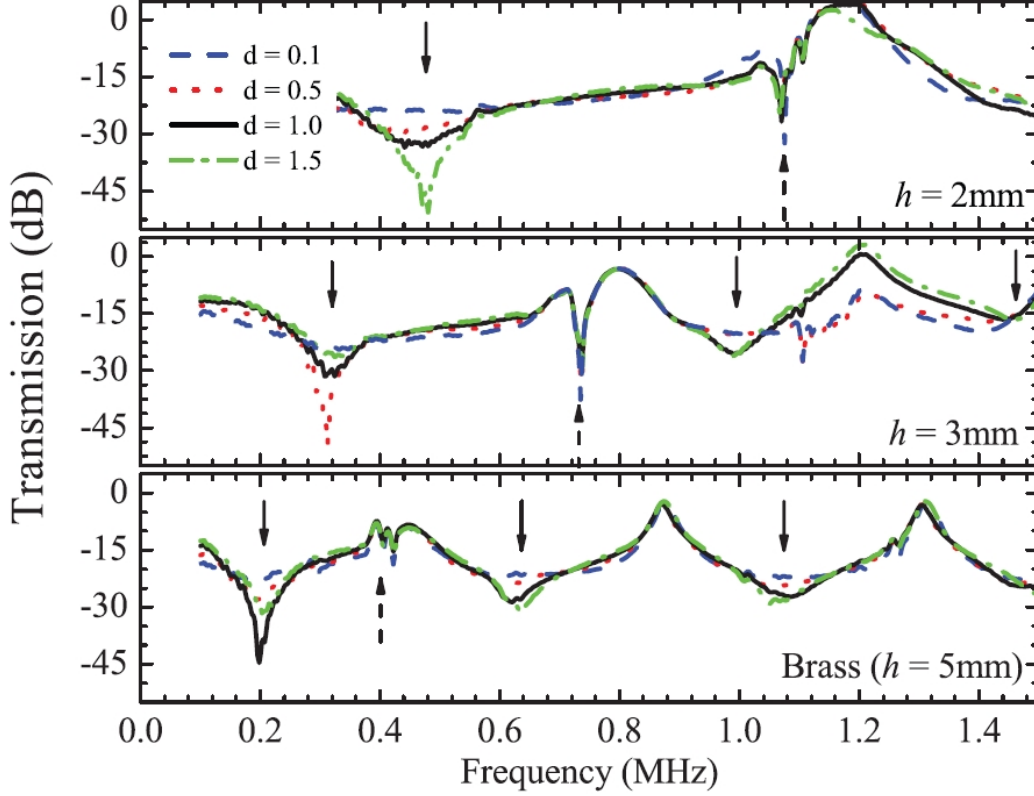
FIGURE 2.1. Experimental sound transmission spectra of a water slit between two brass plates for different channel width $d$ and length $h$, reported in [30]. The vertical arrows indicate the frequencies at which the transmission is extraordinarily low. *Image reprinted from [30], CC BY 3.0.*

I will present the theory of sound transmission through a slit formed by two solid plates, taking into account the elastic nature of the latter. The eigenmodes of the system in question are essentially the Rayleigh waves modified by coupling to the fluid environment. This modification makes the eigenmodes lose their orthogonality with respect to each other. Having a nonorthogonal basis of eigenfunctions is quite typical for problems involving elastic solids, e.g., it is known that the elastic modes of an isolated solid plate (the Rayleigh-Lamb modes) are not orthogonal as well [5]. Moreover, the channel eigenmodes belong to two main categories: the true surface, or propagating, modes, and the leaky modes, though the nonorthogonality makes explicit separation of modes impossible. The latter observation applies also to electromagnetic domain, see, for example, discussion in [90] regarding

the metal-dielectric waveguides.

The analytical solution to the scattering problem relies on the expansion of the acoustic fields in series over both types of those coupled Rayleigh modes propagating in the channel. I also generalize the approach to account for the nonorthogonality of the eigenmodes. Ultimately, I will demonstrate how the fluid channel that partially transmits sound via the leaky waves effectively serves as a redirecting acoustic antenna, and that the effect of redirection of sound causes the suppression of both transmission and reflection. In the rigid-body approximation, producing such an effect is clearly infeasible. For that reason, this effect should not be confused with other previously mentioned manifestations of the strong suppression of sound [71, 23, 24, 22], which introduce Fano-like resonances into the transmission spectrum even in the rigid-body approximation.

## 2.2. Acoustic Potentials

### 2.2.1. Scalar Potential for Pressure Waves in Fluids

In this chapter, I neglect the effects of viscosity and treat the propagation of sound as a laminar (nonturbulent) process in the fluid which is otherwise stationary. With that, only longitudinal pressure waves can exist within the volume of the fluid, and the resulting pressure oscillations are known to be adiabatic, meaning that the wave does not lose or gain energy from the background.

The complete description of the fluid dynamics requires knowledge of either the local velocity $\mathbf{v}_f(\mathbf{r}, t)$ or both the local pressure $p_f(\mathbf{r}, t)$ and density $\rho_f(\mathbf{r}, t)$ at any given position $\mathbf{r}$ and moment of time $t$. These quantities are related since one must satisfy both the continuity equation

$$(2.1) \qquad \frac{\partial \rho_f}{\partial t} + \nabla \cdot (\rho_f \mathbf{v}_f) = 0,$$

which guarantees the conservation of mass in the system, and the momentum equation

$$(2.2) \qquad \frac{\partial \rho_f \mathbf{v}_f}{\partial t} + \nabla p_f = 0,$$

which is essentially the Newton's second law applied to a unit volume of fluid.

9

Assuming the propagating wave is only a small perturbation of the fluid stationary state, the dynamic properties of the fluid are linearized as

$$(2.3) \qquad p_f(\mathbf{r}, t) = p_0 + p(\mathbf{r}, t),$$

$$(2.4) \qquad \rho_f(\mathbf{r}, t) = \rho_0 + \rho(\mathbf{r}, t),$$

$$(2.5) \qquad \mathbf{v}_f(\mathbf{r}, t) = \mathbf{v}_0 + \mathbf{v}(\mathbf{r}, t),$$

where $p_0$, $\rho_0$, and $\mathbf{v}_0$ describe the background acoustic field, and the smallness of perturbations can be understood, for example, as $|p(\mathbf{r}, t)| \ll p_0$. The assumption of no background flow gives $\mathbf{v}_0 = 0$, and the absence of the vortices yields $\nabla \times \mathbf{v}(\mathbf{r}, t) = 0$.

The longitudinal sound wave propagates with a constant phase speed, which is given by

$$(2.6) \qquad c_f = \sqrt{\left(\frac{\partial p_f}{\partial \rho_f}\right)_s},$$

where the derivative is calculated for an adiabatic process, i.e., at constant entropy. Using (2.3)-(2.4), one can relate the local variations of pressure and density as

$$(2.7) \qquad p(\mathbf{r}, t) = \rho(\mathbf{r}, t)c_f^2.$$

Consequently, the wave equation for the pressure $p(\mathbf{r}, t)$,

$$(2.8) \qquad \Delta p - \frac{1}{c_f^2}\frac{\partial^2 p}{\partial t^2} = 0,$$

is immediately obtained after one substitutes (2.2) into (2.1) and uses the linearizations (2.3)-(2.5) while discarding the terms that are quadratic over small perturbation. The condition $\nabla \times \mathbf{v}(\mathbf{r}, t) = 0$ allows to represent the velocity as a gradient of a scalar function (fluid is then said to be in a state of a potential flow):

$$(2.9) \qquad \mathbf{v}(\mathbf{r}, t) = \nabla B(\mathbf{r}, t).$$

For monochromatic waves with the time dependence given by $e^{-i\omega t}$ factor, the equation (2.2) relates the velocity to the gradient of pressure

$$(2.10) \qquad i\omega\rho_0\mathbf{v}(\mathbf{r}, t) = \nabla p(\mathbf{r}, t),$$

and, therefore, one may define the acoustic potential $B(\mathbf{r}, t)$ as

$$(2.11) \qquad\qquad B(\mathbf{r}, t) = \frac{p(\mathbf{r}, t)}{i\omega\rho_0}.$$

From (2.8)-(2.11) it is obvious that the potential $B(\mathbf{r}, t)$ satisfies the wave equation

$$(2.12) \qquad\qquad \Delta B - \frac{1}{c_f^2}\frac{\partial^2 B}{\partial t^2} = 0,$$

and that it uniquely defines the local pressure and velocity of the fluid.

Since the density variations are small, the approximate equality $\rho_f(\mathbf{r}, t) \approx \rho_0$ holds, and in the sections below I will not distinguish between these two quantities and will use the notation $\rho_f$ instead of $\rho_0$.

### 2.2.2. Scalar and Vector Potentials for Elastic Waves in Solids

Unlike fluids which take the shape of the volume they occupy, the elastic properties of solids allow them to resist the changes to their shape in order to reestablish their original form and size. As a result, two distinct types of waves can propagate in the bulk of a solid — longitudinal (compressional) and transverse (shear). In these waves, the particle oscillations occur either along or perpendicular to the direction of wave propagation, respectively. The local displacement field $\mathbf{u}(\mathbf{r}, t)$ and stress tensor $\sigma_{ik}(\mathbf{r}, t)$ are typically used to describe the dynamics of a solid. The Newton's second law applied to a unit volume of the solid

$$(2.13) \qquad\qquad \rho_m\frac{\partial u_i}{\partial t} = \frac{\partial \sigma_{ik}}{\partial x_k},$$

where the Einstein summation convention for tensors is implied, ultimately leads to the following general wave equation for elastic waves [53]:

$$(2.14) \qquad\qquad \frac{\partial^2 \mathbf{u}}{\partial t^2} = c_t^2\Delta\mathbf{u} + \left(c_l^2 - c_t^2\right)\nabla\left(\nabla\cdot\mathbf{u}\right).$$

Here $\rho_m$ is the density of the solid and $c_l(c_t)$ is the speed of the pure longitudinal (transverse) acoustic wave. The two speeds of sound are expressed through the so-called Lamé parameters of the solid, $\lambda$ and $\mu$:

$$(2.15) \qquad\qquad c_l = \sqrt{\frac{\lambda + 2\mu}{\rho}}, \qquad c_t = \sqrt{\frac{\mu}{\rho}},$$

11

which in their turn represent the bulk and shear moduli $K$ and $G$:

$$(2.16) \qquad K \;=\; \lambda + \frac{2}{3}\mu, \qquad G \;=\; \mu.$$

Since, according to the Helmholtz decomposition theorem, the vector quantity $\mathbf{u}(\mathbf{r},t)$ can always be represented as a sum of a potential and a solenoidal field:

$$(2.17) \qquad \mathbf{u} = \mathbf{u}_l + \mathbf{u}_t,$$

where $\nabla \times \mathbf{u}_l = 0$ and $\nabla \cdot \mathbf{u}_t = 0$, it allows splitting (2.14) into two independent wave equations

$$(2.18) \qquad \Delta \mathbf{u}_{l,t} - \frac{1}{c_{l,t}^2} \frac{\partial^2 \mathbf{u}_{l,t}}{\partial t^2} \;=\; 0$$

for both longitudinal and transverse components of the elastic wave and introduce the scalar potential $L(\mathbf{r},t)$ and the vector potential $\mathbf{S}(\mathbf{r},t)$ as

$$(2.19) \qquad \mathbf{u}_l(\mathbf{r},t) \;=\; \nabla L(\mathbf{r},t), \qquad \mathbf{u}_t(\mathbf{r},t) \;=\; \nabla \times \mathbf{S}(\mathbf{r},t).$$

With the scalar potential $L$ corresponding to the pressure wave and the vector potential $\mathbf{S}$ representing the shear wave, naturally, they satisfy the respective wave equations:

$$(2.20) \qquad \Delta L - \frac{1}{c_l^2} \frac{\partial^2 L}{\partial t^2} \;=\; 0,$$

$$(2.21) \qquad \Delta \mathbf{S} - \frac{1}{c_t^2} \frac{\partial^2 \mathbf{S}}{\partial t^2} \;=\; 0,$$

and uniquely define the local displacement of the solid

$$(2.22) \qquad \mathbf{u}(\mathbf{r},t) \;=\; \nabla L(\mathbf{r},t) + \nabla \times \mathbf{S}(\mathbf{r},t)$$

and stress tensor (through Hooke's law)

$$(2.23) \qquad \sigma_{ik}(\mathbf{r},t) \;=\; \lambda u_{ll}(\mathbf{r},t)\delta_{ik} + 2\mu u_{ik}(\mathbf{r},t).$$

Here $u_{ik}$ denotes the strain tensor $u_{ik} = \frac{1}{2}\left(\frac{\partial u_i}{\partial x_k} + \frac{\partial u_k}{\partial x_i}\right)$, and $\delta_{ik}$ is the Kronecker delta.

Note that the potentials themselves are not defined uniquely, specifically, adding a curl of an arbitrary vector function to $L(\mathbf{r},t)$ or adding a gradient of an arbitrary scalar function to $\mathbf{S}(\mathbf{r},t)$ does not change the displacement field $\mathbf{u}(\mathbf{r},t)$.

### 2.2.3. Fluid-Solid Boundary Conditions

When a fluid and a solid occupy adjacent regions of space, the boundary conditions must be specified at the fluid-solid interface (see [57], for example). The continuity of the normal component of the local velocity

$$(2.24) \qquad v_n|_\Sigma \;=\; \dot{u}_n|_\Sigma$$

ensures that the two media neither permeate each other nor produce void regions between them along the interface $\Sigma$. As the fluid is nonviscous, there is no binding between the tangential components of velocities, and the particles of the fluid do not stick to the surface of the solid.

Other than that, the balance between the stress of the solid and the pressure in the fluid

$$(2.25) \qquad \sigma_{ik}n_k|_\Sigma = -\,pn_i|_\Sigma$$

must be enforced. Here the vector $n_i$ is the external normal to the surface $\Sigma$, and due to the absence of shear interactions in fluid its pressure is acting perpendicular to $\Sigma$: $p_i = -pn_i$.

### 2.3. Rayleigh Waves on the Surface of a Solid

When considering the propagation of elastic waves in the bulk of a solid, one infers the independence of pressure waves from shear waves in the sense that the wave amplitudes are not tied to each other. However, a specific relationship between the amplitudes arises when the waves propagate close to the surface of the solid, which requires satisfying the boundary conditions (2.24)-(2.25). In particular, the wave equation (2.14) was shown to have a surface wave solution — the so-called Rayleigh wave [77], which intertwines both longitudinal and transverse particle motion and is concentrated in the vicinity of the surface, exponentially vanishing away from it. The Rayleigh waves are typically distinguished from the Lamb waves, which are the elastic surface waves as well, but are specific for the thin solid plates.

The concept of Rayleigh waves is normally demonstrated in the simplified situation, where the solid borders with the vacuum [53]. Here I assume the planar interface that coincides with the plane $z = 0$ (where the region $z > 0$ is occupied by solid), and I seek the monochromatic solution to (2.20)-(2.21) which propagates in the $x$-direction and exponentially decays with $z$. This solution is only valid in the region $z \geq 0$, as in the vacuum the sound does not propagate.

The independent of the coordinate $y$ acoustic potentials can thus be written down as

$$(2.26) \qquad L(x, z, t) \;=\; l\, e^{i\beta x - \nu z - i\omega t}, \qquad z \geq 0,$$

$$(2.27) \qquad \mathbf{S}(x, z, t) \;=\; \mathbf{s}\, e^{i\beta x - \eta z - i\omega t}, \qquad z \geq 0,$$

where $\beta$ is the $x$-component of the wavevector, $l$ and $\mathbf{s} = (s_x, s_y, s_z)$ are the amplitudes of the potentials. The quantities $\nu$ and $\eta$ are defined as

$$(2.28) \qquad \nu \;=\; \sqrt{\beta^2 - k_l^2}, \qquad\qquad \beta \geq k_l = \frac{\omega}{c_l},$$

$$(2.29) \qquad \eta \;=\; \sqrt{\beta^2 - k_t^2}, \qquad\qquad \beta \geq k_t = \frac{\omega}{c_t}.$$

The components of the displacement field are calculated from the potentials using (2.22):

$$(2.30) \qquad u_x \;=\; \frac{\partial L}{\partial x} - \frac{\partial S_y}{\partial z} \;=\; \left( i\beta e^{-\nu z} \cdot l + \eta e^{-\eta z} \cdot s_y \right) e^{i\beta x - i\omega t},$$

$$(2.31) \qquad u_y \;=\; \frac{\partial S_x}{\partial z} - \frac{\partial S_z}{\partial x} \;=\; -\left( \eta \cdot s_x + i\beta \cdot s_z \right) e^{-\eta z} e^{i\beta x - i\omega t},$$

$$(2.32) \qquad u_z \;=\; \frac{\partial L}{\partial z} + \frac{\partial S_y}{\partial x} \;=\; \left( -\nu e^{-\nu z} \cdot l + i\beta e^{-\eta z} \cdot s_y \right) e^{i\beta x - i\omega t}.$$

The solid-vacuum boundary is a free boundary, so one may only demand that any infinitesimal part of the interface is stress-free, namely, that

$$(2.33) \qquad \sigma_{xz} \;=\; \sigma_{yz} \;=\; \sigma_{zz} \;=\; 0,$$

at the interface $z = 0$, or, more explicitly,

(2.34)
$$
\begin{cases}
0 = \sigma_{xz} = 2\mu u_{xz} = \mu\left(\dfrac{\partial u_x}{\partial z} + \dfrac{\partial u_z}{\partial x}\right), \\[2mm]
0 = \sigma_{yz} = 2\mu u_{yz} = \mu\dfrac{\partial u_y}{\partial z}, \\[2mm]
0 = \sigma_{zz} = 2\mu u_{zz} + \lambda\nabla\cdot\mathbf{u} = 2\mu\dfrac{\partial u_z}{\partial z} + \lambda\left(\dfrac{\partial u_x}{\partial x} + \dfrac{\partial u_z}{\partial z}\right).
\end{cases}
$$

The second equation in the system suggests that $u_y = 0$, and without any loss of generality one may equate both $s_x$ and $s_z$ to zero, thus leaving $s_y$ as the only nonzero component of the coefficient $\mathbf{s}$. This becomes possible due to the fact that one may add a gradient of any scalar function to $\mathbf{S}(\mathbf{r}, t)$ without any effect on the displacement field. If one now selects this scalar function to be $f(\mathbf{r}, t) = (s_z/\eta)\, e^{i\beta x - \eta z - \imath\omega t}$, then the redefined potential $\mathbf{S}'(\mathbf{r}, t) = \mathbf{S}(\mathbf{r}, t) + \nabla f(\mathbf{r}, t)$ will automatically have $S'_z = 0$, and it will also have $S'_x = 0$ due to the relation (2.31) and the condition $u_y = 0$. With this, I will further assume the vector potential to have only nonzero $y$-component, $\mathbf{S}(\mathbf{r}, t) = (0, S(\mathbf{r}, t), 0)$, and $\mathbf{s} = (0, s, 0)$. It is worth mentioning that even though the wave is propagating along the $x$-axis, its amplitude, nevertheless, varies with the coordinate $z$, causing the vector potential to give a nonzero contribution to the displacement $u_x$, and it is thus impossible to break down the Rayleigh wave into independent longitudinal and transverse components.

Now, using (2.30)-(2.32), the first and the third equations from (2.34) are reduced to

(2.35)
$$
\begin{cases}
(\beta^2 + \eta^2)\cdot s + 2i\beta\nu\cdot l = 0, \\[2mm]
-2i\mu\beta\eta\cdot s + (2\mu\nu^2 - \lambda k_l^2)\cdot l = 0,
\end{cases}
$$

The obtained system has a nontrivial solution if and only if its determinant equals zero, namely, if

(2.36)
$$
\frac{1}{\mu}\left(2\mu\nu^2 - \lambda k_l^2\right)\left(\beta^2 + \eta^2\right) - 4\beta^2\eta\nu = 0,
$$

or, when simplified,

(2.37)
$$
\left(\eta^2 + \beta^2\right)^2 - 4\nu\eta\beta^2 = 0.
$$

15
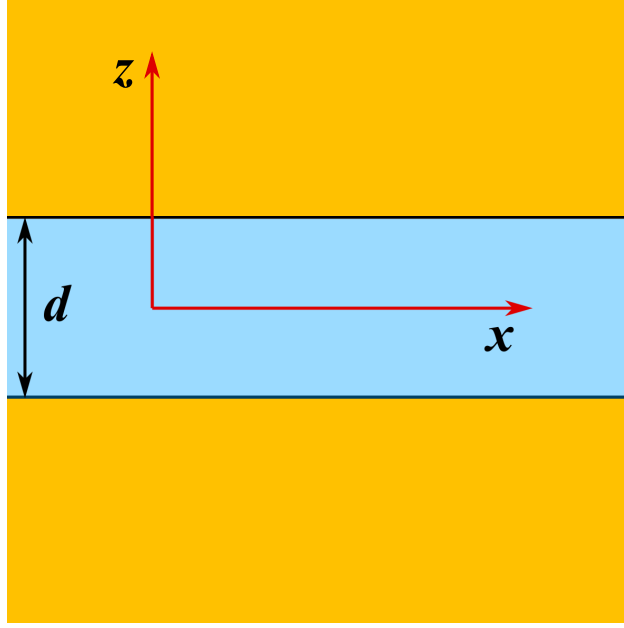
FIGURE 2.2. An infinite fluid channel between two elastic plates.

The latter expression implicitly relates the frequency of the wave $\omega$ and its wavevector $\beta$, and it can be rewritten for the dimensionless phase velocity $\xi = \omega/\beta c_t$ as

$$(2.38) \qquad \left(2 - \xi^2\right)^2 - 4\sqrt{1 - \xi^2}\sqrt{1 - \frac{c_t^2}{c_l^2}\xi^2} \;=\; 0.$$

Since typically $c_t < c_l$ in solids, the equation (2.38) has only one real root for any value of $c_t/c_l$ which lies in the range $0 < \xi < 1$; for most common solids, the dimensionless phase speed is restricted to the range $0.874 \leq \xi \leq 0.955$ [53]. Such values of $\xi$ describe surface waves which propagate slower than either the pure pressure or shear wave in the bulk of the solid. For any given solid, the speed of the Rayleigh wave is uniquely defined by the ratio of its transverse and longitudinal speeds of sound, and does not depend on the wave frequency.

2.4. Coupled Rayleigh Waves in the Fluid Channel between Two Solid Plates

Now I consider a monochromatic sound wave propagating along an infinite straight fluid channel of the width $d$ between two elastic plates (see Fig. 2.2). The elastic plates are made from the same material and they are occupying the regions $|z| > d/2$. The wave is propagating in the positive $x$-direction. The mirror symmetry with respect to the $xOy$ plane

16

suggests that the eigenmodes of the system are either even or odd functions of the coordinate $z$. More precisely, I will be using the term "even" to describe the eigenmodes with $u_x$ being an even and $u_z$ being an odd function of $z$. The term "odd" will then refer to any mode with $u_x$ being an odd function of $z$. In terms of potentials, the even mode corresponds to all potentials being even functions of $z$.

Below, I will analyze only the even modes and pay no attention to the odd modes. The reason for that is the mirror symmetry with respect to the $x$-axis that will be enforced everywhere in the subsequent sections. For the scattering problem it means that the impinging wave should be incident only normally at the system, along the $x$-axis. The excitation of the odd modes will not be possible at all as they violate the symmetry. However, the odd modes can be excited if the problem loses its symmetry with respect to $xOy$ plane, either by allowing the oblique incidence of the sound wave or by having the elastic plates made from different materials [30].

### 2.4.1. Dispersion Relation

The symmetric solution of the wave equations (2.12), (2.20), and (2.21) is as follows (the factor $e^{-i\omega t}$ is omitted everywhere below):

$$(2.39) \qquad B(x,z) \;=\; b\,e^{i\beta x}\cos kz, \qquad\qquad\qquad |z| < d/2,$$

$$(2.40) \qquad L(x,z) \;=\; l\,e^{i\beta x - \nu|z|}, \qquad\qquad\qquad\qquad |z| > d/2,$$

$$(2.41) \qquad S_y(x,z) \;=\; s\,e^{i\beta x - \eta|z|}, \qquad S_x = S_z = 0, \qquad |z| > d/2,$$

where $k = \sqrt{k_f^2 - \beta^2}$, $k_f = \omega/c_f$. Both $\nu$ and $\beta$ are defined as earlier in (2.28)-(2.29) except that no restriction is placed on the value of $\beta$.

Because of the symmetry, it is sufficient to write the boundary conditions only for, e.g. $z = d/2$. At this fluid-metal interface the stress and the normal component of the velocity are continuous:

$$(2.42) \qquad\qquad\qquad \sigma_{zz} \;=\; -p, \qquad \sigma_{xz} \;=\; 0, \qquad \dot{u}_z \;=\; v_z,$$

17

as follows from (2.24)-(2.25). The stress tensor component $\sigma_{yz}$ is identically zero due to the choice of the vector potential $\mathbf{S}$.

Similarly to the derivations in the previous section, the boundary conditions yield the following system where all the potentials are evaluated at $z = d/2$:

(2.43)
$$\begin{cases} -\lambda k_l^2 L + 2\mu\left(\dfrac{\partial^2 L}{\partial z^2} + \dfrac{\partial^2 S}{\partial x \partial z}\right) &= -i\omega\rho_f B, \\[2mm] \mu\left(2\dfrac{\partial^2 L}{\partial x \partial z} + \dfrac{\partial^2 S}{\partial x^2} - \dfrac{\partial^2 S}{\partial z^2}\right) &= 0, \\[2mm] -i\omega\left(\dfrac{\partial L}{\partial z} + \dfrac{\partial S_y}{\partial x}\right) &= \dfrac{\partial B}{\partial z}, \end{cases}$$

which is reduced to

(2.44)
$$\begin{cases} (2\mu\nu^2 - \lambda k_l^2)\,e^{-\nu d/2} \cdot l &- &2i\mu\eta\beta\,e^{-\eta d/2} \cdot s &+ &i\omega\rho_f\cos(kd/2) \cdot b &= 0, \\[2mm] 2i\nu\beta\,e^{-\nu d/2} \cdot l &+ &(\beta^2 + \eta^2)\,e^{-\eta d/2} \cdot s & & &= 0, \\[2mm] i\omega\nu\,e^{-\nu d/2} \cdot l &+ &\omega\beta\,e^{-\eta d/2} \cdot s &+ &k\sin(kd/2) \cdot b &= 0. \end{cases}$$

This set of homogeneous linear equations has a nontrivial solution if its determinant vanishes, which is expressed by the condition

(2.45)
$$\left(\eta^2 + \beta^2\right)^2 - 4\nu\eta\beta^2 = \frac{\rho_f}{\rho_m}\frac{\omega^4}{c_t^4}\frac{\nu}{k}\cot\frac{kd}{2}.$$

Since all the quantities $k$, $\nu$, and $\eta$ are expressed through $\omega$ and $\beta$, the latter equation is essentially the dispersion relation for the coupled Rayleigh waves propagating in the fluid channel. This relation can be rewritten in terms of the dimensionless frequency $\Omega = \omega d/c_t$ and wavevector $q = \beta d$, which allows to eliminate the dependence on the channel width $d$ from the picture:

(2.46)
$$\left(2q^2 - \Omega^2\right)^2 - 4q^2\sqrt{q^2 - (c_t/c_l)^2\Omega^2}\sqrt{q^2 - \Omega^2} = \frac{\rho_f}{\rho_m}\Omega^4\sqrt{\frac{q^2 - (c_t/c_l)^2\Omega^2}{(c_t/c_f)^2\Omega^2 - q^2}}\cot\left(\frac{1}{2}\sqrt{\frac{c_t^2}{c_f^2}\Omega^2 - q^2}\right).$$

Also, the dispersion relation for the dimensionless phase velocity $\xi = \omega/\beta c_t$ can be obtained from the latter by substituting $q = \Omega/\xi$:

(2.47) $\quad \left(2 - \xi^2\right)^2 - 4\sqrt{1 - \xi^2}\sqrt{1 - \dfrac{c_t^2}{c_l^2}\xi^2} = \dfrac{\rho_f}{\rho_m}\xi^4\sqrt{\dfrac{1 - (c_t/c_l)^2\,\xi^2}{(c_t/c_f)^2\,\xi^2 - 1}}\cot\left(\dfrac{\Omega}{2\xi}\sqrt{\dfrac{c_t^2}{c_f^2}\xi^2 - 1}\right).$

18

Real and complex solutions of the dispersion relation (2.46) define the allowed values of the wave vector $q = q(\Omega)$ for each frequency $\Omega$, and (2.47) gives the allowed phase velocities $\xi = \xi(\Omega)$.

## 2.4.2. Analysis of the Dispersion Branches

For any frequency $\Omega$, the dispersion equation (2.47) has a finite number of real ($\xi = \text{Re } \xi > 0$) and an infinite number of complex (Re $\xi > 0$, Im $\xi < 0$) roots. The condition Re $\xi > 0$ ensures that the eigenmodes found indeed propagate forward in the $+x$-direction. Since the phase speed $\xi$ enters (2.47) only as $\xi^2$, it is obvious that a negative of any root $\xi$ with a positive real part also satisfies the dispersion equation. Such roots describe the backward propagating Rayleigh waves, i.e., in the $-x$-direction.

In the numerical analysis below, I will be using the parameters of water ($\rho_f = 1000$ kg/m$^3$, $c_f = 1500$ m/s) and brass ($\rho_m = 8400$ kg/m$^3$, $c_t = 2000$ m/s, $c_l = 4250$ m/s).

## 2.4.3. Real Eigenmodes

The eigenmodes with real $\xi$ have real wavevector $q$, and, therefore, they are propagating modes. If the losses in the media are neglected, these true modes will never decay as they propagate along the channel. Due to the term $\sqrt{1 - \xi^2}$ in (2.47), the value of $\xi$ must be restricted to the range $0 < \xi \leq 1$. This means that in (2.39)-(2.41) the values of $\beta$, $\nu$, and $\eta$ are purely real which provides the oscillating behavior along the channel and the decay of the acoustic field into the solid away from the channel. As for the value of $k$, it may be either purely real (when $c_f/c_t < \xi \leq 1$) or purely imaginary (when $0 < \xi < c_f/c_t$). Here I assume that $c_f < c_{l,t}$, since the speed of sound in fluids is considerably lower than the speed of sound in solids. In the first case, the acoustic potential in the fluid oscillates along $z$ as well and the sound wave has a wavefront of constant amplitude inside the channel. The two Rayleigh waves on each fluid-solid interface are strongly coupled as the sound energy is not concentrated in the vicinity of either interface but rather confined to the whole width of the channel. In the second case, the potential (2.39) becomes $B(x, z) = b\, e^{ibx} \cos kz = b\, e^{ibx} \cosh |kz|$, so that the sound energy both in the solid and in the fluid is mostly concentrated near the in-

terfaces.

These two types of true eigenmodes will further be referred to as fast and slow modes since the former propagate faster than the speed of sound in fluid, and the latter propagate slower, respectively.

The dispersion equation (2.47) is transcendental and can only be solved numerically. Nevertheless, a certain asymptotic analysis of the eigenmode dispersion is still possible. I start by considering the fast modes. I note that the left-hand side of (2.47) is clearly identical to that of (2.38). Its right-hand side thus describes the coupling of two individual Rayleigh waves on each interface through the fluid. The coupling strength is proportional to the ratio $\rho_f/\rho_m$. In the absence of the fluid, $\rho_f = 0$, the coupling term disappears and the surface waves in each plate become uncoupled. These surface waves are the same Rayleigh waves described by (2.38), with their phase speed $\xi = \xi_R$ independent from the frequency. Thus in the limit $\rho_f/\rho_m \ll 1$, when the right-hand side of (2.47) is small, the coupled Rayleigh waves should be almost dispersionless.

However, the previous argument cannot be valid if the argument of the cotangent $kd/2$ is close to an integer of $\pi$, in which case the value of the cotangent outmatches the smallness of $\rho_f/\rho_m$. The condition $kd/2\pi = 0, 1, 2, ...$ corresponds to the potential (2.39) being a standing wave with its velocity nodes at the channel walls, which can be seen by calculating $v_z$:

$$(2.48) \qquad v_z(x, z)|_{z=\frac{d}{2}} = \left.\frac{\partial B}{\partial z}\right|_{z=\frac{d}{2}} = -kbe^{i\beta x}\sin\frac{kd}{2} = 0.$$

In other words, the coupled Rayleigh wave behaves identically to a waveguide mode of a channel with ideally rigid walls. The dispersion of the symmetric waveguide modes consists of an infinite number of branches

$$(2.49) \qquad \omega_n = c_f\sqrt{\left(\frac{2\pi n}{d}\right)^2 + \beta^2}, \qquad n = 0, 1, 2, ...$$

These branches serve as asymptotic boundaries for the dispersion branches of the coupled Rayleigh waves. Each waveguide mode appears after its respective cutoff frequency with the wavevector $\beta = 0$, and features an infinite phase velocity $\omega_n/\beta$ (except for the mode $n = 0$).

Similar to the waveguide modes, each individual Rayleigh modes also emerges only after a corresponding cutoff frequency. However, the condition $\beta = 0$ does not define the cutoff frequency in this case since the phase speed $\xi$ of the fast modes cannot be infinite: $c_f/c_t < \xi \leq 1$. Clearly, every new dispersion branch must then start with $\xi = 1$, which gives the dimensionless cutoff frequencies

(2.50)
$$\Omega_n = \frac{\omega_n d}{c_t} = \frac{2}{\sqrt{(c_t/c_f)^2 - 1}} \left[ \pi (n-1) + \arctan \left( \frac{\rho_f}{\rho_m} \sqrt{\frac{1 - (c_t/c_l)^2}{(c_t/c_f)^2 - 1}} \right) \right], \quad n = 1, 2, \ldots$$

and the corresponding dimensionless wavevectors $q_n = \Omega_n/\xi = \Omega_n$.

Even for the first fast mode the cutoff frequency $\Omega_1$ is nonzero, and thus in the limit of low frequencies no fast modes can be excited to propagate in the fluid channel.

Unlike the fast modes, the single slow coupled Rayleigh mode exists in the whole frequency range starting from $\Omega = 0$ with $\xi = 0$ and asymptotically approaching $\xi = c_f/c_t$ when $\Omega \to \infty$. The slow mode is characterized by purely imaginary $k$, and its dispersion equation

(2.51) $\left(2 - \xi^2\right)^2 - 4\sqrt{1 - \xi^2}\sqrt{1 - \frac{c_t^2}{c_l^2}\xi^2} = -\frac{\rho_f}{\rho_m}\xi^4\sqrt{\frac{1 - (c_t/c_l)^2\,\xi^2}{1 - (c_t/c_f)^2\,\xi^2}}\coth\left(\frac{\Omega}{2\xi}\sqrt{1 - \frac{c_t^2}{c_f^2}\xi^2}\right)$

is derived using (2.39)-(2.45), where $k = i|k|$ and $\cos kz$ is replaced with $\cosh |kz|$ in the expression for the potential $B(x, z)$.

For $\xi \ll 1$ and $\Omega \ll 1$, I expand the left-hand side of the latter dispersion equation in series over $\xi$ and keep the most significant term only:

(2.52)
$$-2\left(1 - \frac{c_t^2}{c_l^2}\right)\xi^2 \approx -\frac{\rho_f}{\rho_m}\xi^4\coth\frac{\Omega}{2\xi}.$$

Under the additional assumption $\Omega \ll \xi$ (which is justified by solving the dispersion equation at low frequencies numerically) the cotangent $\coth\dfrac{\Omega}{2\xi}$ can be replaced by its approximate value $\dfrac{2\xi}{\Omega}$, and one obtains

(2.53)
$$\xi^3 \approx \frac{\rho_m}{\rho_f}\left(1 - \frac{c_t^2}{c_l^2}\right)\Omega$$

21

or, in terms of the wavevector $q = \Omega/\xi$,

$$(2.54) \qquad \Omega \approx \sqrt{\frac{\rho_m}{\rho_f}\left(1 - \frac{c_t^2}{c_l^2}\right)} \, q^{3/2}.$$

It appears that the slow mode exhibits an essentially nonlinear dispersion in the long-wavelength limit, with the vanishing phase and group velocities for $\Omega = 0$. The low-frequency waveguide mode (2.49), however, features purely linear dispersion (for $n = 0$). This means that the subwavelength propagation of sound through a fluid channel is drastically different for the cases of a real channel with vibrating walls and of an ideal channel with rigid walls. The same is known for the transmission of electromagnetic waves through a deeply subwavelength metallic slit, in which case some interesting features arise that do not exist for perfectly conducting screens [85, 14].

In the high-frequency limit the phase speed of the slow mode is bound by the condition $\xi < c_f/c_t$. More precisely, the phase speed $\xi$ asymptotically approaches a specific value $\xi_a$: $\xi \to \xi_a < c_f/c_t$. This limiting phase speed $\xi_a$ satisfies the equation

$$(2.55) \qquad \left(2 - \xi_a^2\right)^2 - 4\sqrt{1 - \xi_a^2}\sqrt{1 - \frac{c_t^2}{c_l^2}\xi_a^2} = -\frac{\rho_f}{\rho_m}\xi_a^4\sqrt{\frac{1 - (c_t/c_l)^2\,\xi_a^2}{1 - (c_t/c_f)^2\,\xi_a^2}},$$

which is obtained from (2.51) for high frequencies $\Omega$, where the value of hyperbolic cotangent is approximately 1 for large arguments. The deviation of $\xi_a$ from $c_f/c_t$ is small whenever the ratio $\rho_f/\rho_m$ is small. To demonstrate this, I rearrange the latter equation as

$$(2.56) \qquad \sqrt{c_f/c_t - \xi_a}\sqrt{c_f/c_t + \xi_a} = \frac{\rho_f}{\rho_m}\frac{(c_f/c_t)\,\xi_a^4\sqrt{1 - (c_t/c_l)^2\,\xi_a^2}}{4\sqrt{1 - \xi_a^2}\sqrt{1 - (c_t/c_l)^2\,\xi_a^2} - \left(2 - \xi_a^2\right)^2},$$

and for $\rho_f/\rho_m \ll 1$ the value of $\xi_a$ can be replaced by $c_f/c_t$ everywhere except under the first square root in the left-hand side. This yields

$$(2.57) \qquad \frac{c_f}{c_t} - \xi_a \approx \frac{1}{2}\left(\frac{\rho_f}{\rho_m}\right)^2\left(\frac{(c_f/c_t)^{9/2}\sqrt{1 - (c_f/c_l)^2}}{4\sqrt{1 - (c_f/c_t)^2}\sqrt{1 - (c_f/c_l)^2} - \left(2 - (c_f/c_t)^2\right)^2}\right)^2.$$
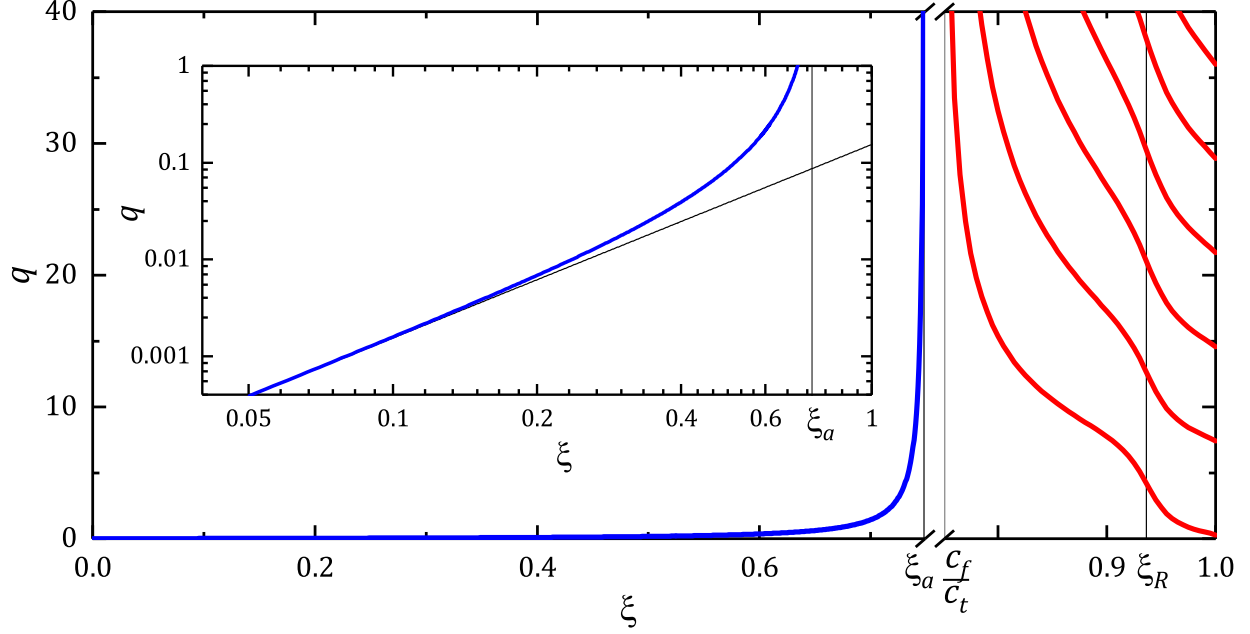
FIGURE 2.3. Dimensionless phase velocity $\xi = \Omega/q$ vs wave vector $q = \beta d$ for the infinite water channel between two brass plates, $\rho_f/\rho_m = 0.12$. The fast mode is represented by an infinite number of waveguide branches above the speed of sound in water, $c_f/c_t < \xi \leq 1$ (red curves). The phase velocity of the slow mode grows very fast (blue line near the vertical axis) and saturates below the level $\xi = c_f/c_t$ for very small $q = \beta d \approx 0.2$. Insert is the blowup of this narrow region where the phase velocity behaves as $\xi \sim \sqrt{q}$ (note the logarithmic scale of both axes). The dashed line is the asymptotic dependence obtained from (2.54).

The phase speed of the slow mode then has the following asymptotic dependence on the frequency:

$$(2.58) \qquad\qquad (\xi_a - \xi) \sim e^{-\Omega}, \qquad \Omega \to \infty,$$

which originates from the approximation $\coth(\Omega/2) \approx 1+2e^{-\Omega}$ for large values of $\Omega$. The dispersion of the slow mode is then almost linear, $\Omega \approx \xi_a q$, and the mode propagates slightly slower than the pure pressure wave in the fluid.

The numerically calculated dispersion of the real eigenmodes given by (2.45) is shown
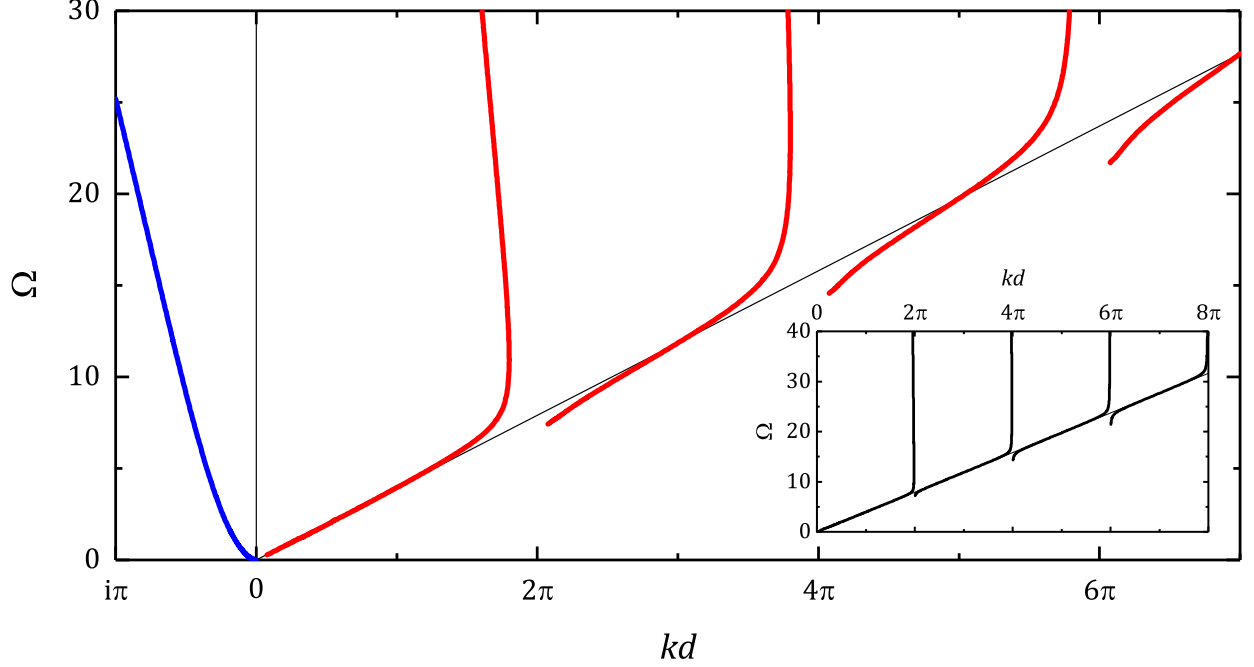
FIGURE 2.4. Dispersion relation between dimensionless frequency $\Omega = c_t\omega/d$ and transverse wavevector $kd/2$ obtained from (2.47) for the infinite water channel between two brass plates, $\rho_f/\rho_m = 0.12$. The linear dispersion for the case of $\rho_f/\rho_m = 0$ (Rayleigh wave) is shown by a thin line. The inset shows the dispersion of the fast mode for very weak coupling, $\rho_f/\rho_m = 0.01$. In this case the waveguide modes are reduced to almost vertical lines at $kd/2 = \pi n$. Dispersion of the slow mode obtained from (2.47) for purely imaginary values of $k$ is plotted to the left of the origin.

in Fig. 2.3 and Fig. 2.4. The Fig. 2.3 shows the dimensionless phase speed $\xi$ versus the wavevector $q$. The fast eigenmodes are enumerated by the integer $n$, with the lower number corresponding to the branch with lower cutoff frequency. The slow mode is labeled by 0.

All the fast-mode branches lie between the two horizontal lines, $\xi = c_f/c_t$ and $\xi = 1$, and emerge at their corresponding cutoff frequency $\Omega_n$ given by (2.50). Close to the level of the phase velocity of the Rayleigh wave, $\xi = \xi_R$, the dispersion curves flatten and then become steep again. Eventually, they saturate at the level $\xi = c_f/c_t$.

The line displaced below $\xi = c_f/c_t$ in Fig. 2.3 represents the slow Rayleigh mode. This

24

branch starts from zero frequency with zero phase speed. For $q > 5$, the phase speed already saturates to the level $\xi = \xi_a$ given by (2.57). This leaves only the short subwavelength region, where the phase speed grows rapidly. In this region, the channel width is smaller than the wavelength of sound, $\lambda \geq 2\pi d/5$, where the wavelength is $\lambda = 2\pi/\beta = 2\pi d/q$.

In the limit of very long wavelengths, $\lambda > 100\pi d$, the asymptotic approximation (2.54) is valid and agrees well with the numerically calculated spectrum.

The Fig. 2.4 shows the dimensionless frequency $\Omega$ versus $kd/2$. Here the horizontal axis does not represent the wavevector in the direction of propagation, and thus the slope of the curves is unrelated to either phase or group velocity.

For $\rho_f/\rho_m \ll 1$, the dispersion of the fast modes strictly follows the linear Rayleigh wave dispersion (given by (2.38)), except for the points $kd/2 = \pi n$ $(n = 1, 2, \ldots)$, where the coupled Rayleigh waves become waveguide modes of the channel with rigid walls. The dispersion curves are practically vertical for those values of $k$.

In the case of $\rho_f/\rho_m = 0.12$, the fast-mode branches emerge below the Rayleigh wave dispersion (2.38) and do not follow the dispersion curves for either limiting case as accurately as it was for $\rho_f/\rho_m \ll 1$.

The slow mode is plotted separately since it is characterized by purely imaginary values of $k$ in (2.45). For the sake of visualization, the corresponding values of $k$ are plotted along the negative direction of the horizontal axis. When the value of $k$ is large, $|k|d/2 \gg 1$, the dispersion of the slow mode becomes practically linear.

2.4.4. Complex Eigenmodes

The dispersion equation (2.47) has an infinite number of complex roots with $\mathrm{Re}\,\xi > 0$ for any frequency $\omega = \Omega d/c_t$ (which is assumed to be purely real). The wavevectors $\beta$ of the corresponding coupled Rayleigh waves acquire imaginary part, $\beta = \omega/c_t\xi = \beta' + i\beta''$. As a result, the eigenmodes either exponentially grow or decay as they propagate into the channel, as described by the term $e^{i\beta x} = e^{i\beta' x - \beta'' x}$ in the acoustic potentials. Since the exponential growth of the amplitude is physically unreasonable, only the roots with $\xi'' = \mathrm{Im}\,\xi < 0$ must be considered in order to guarantee that $\beta'' > 0$.

The decay of the eigenmode into the channel implies that the acoustic energy is radiated away from the channel (as the media themselves are lossless). The Rayleigh wave in the solid plates must then be a propagating wave in $z$-direction, which can be realized if the coefficients $\nu$ and $\eta$ acquire imaginary parts as well. Indeed, from the definitions (2.28)-(2.29) it is clear that both $\nu$ and $\eta$ are complex if the wavevector $\beta$ is complex. By analyzing the terms in the potentials (2.40)-(2.41) that describe the $z$ dependence, $e^{-\nu z} = e^{-\nu' z - i\nu'' z}$ and $e^{-\eta z} = e^{-\eta' z - i\eta'' z}$, one can see that the imaginary parts of both coefficients $\nu$ and $\eta$ must be negative. Moreover, their real parts need to be negative as well. The Rayleigh wave amplitude will then oscillate and exponentially grow along $z$ and oscillate and exponentially decay along $x$. Such inhomogeneous plane wave is a so-called leaky wave, which radiates energy in the direction at a certain angle from the channel. It also maintains constant amplitude along that direction due to the mutual balancing of the exponential grow and decay along $z$ and $x$.

It is crucial, however, to specify how the square roots in these definitions need to be calculated in order to ensure the desired propagating behavior along $z$. One way to redefine coefficients (2.28) and (2.29) to ensure the leaky-wave behavior is to choose a second branch of the complex square root function:

$$\text{(2.59)} \qquad \nu = -\sqrt{\beta^2 - k_l^2}, \qquad\qquad \text{Re } \beta \geq k_l = \frac{\omega}{c_l},$$

$$\text{(2.60)} \qquad \eta = -\sqrt{\beta^2 - k_t^2}, \qquad\qquad \text{Re } \beta \geq k_t = \frac{\omega}{c_t}.$$

A more detailed discussion on the leaky waves and the corresponding revision of the square root function can be found in Appendix A.

The dispersion equation for the coupled Rayleigh leaky modes will then differ from (2.47) by having an additional negative sign in its right-hand side:

$$\text{(2.61)} \quad \left(2 - \xi^2\right)^2 - 4\sqrt{1 - \xi^2}\sqrt{1 - \frac{c_t^2}{c_l^2}\xi^2} = -\frac{\rho_f}{\rho_m}\xi^4\sqrt{\frac{1 - (c_t/c_l)^2\,\xi^2}{(c_t/c_f)^2\,\xi^2 - 1}}\cot\left(\frac{\Omega}{2\xi}\sqrt{\frac{c_t^2}{c_f^2}\xi^2 - 1}\right).$$

The frequency dispersion of several complex roots of (2.61) is shown in Fig. 2.5. These roots are ordered according to their imaginary parts, meaning that they are assigned

26
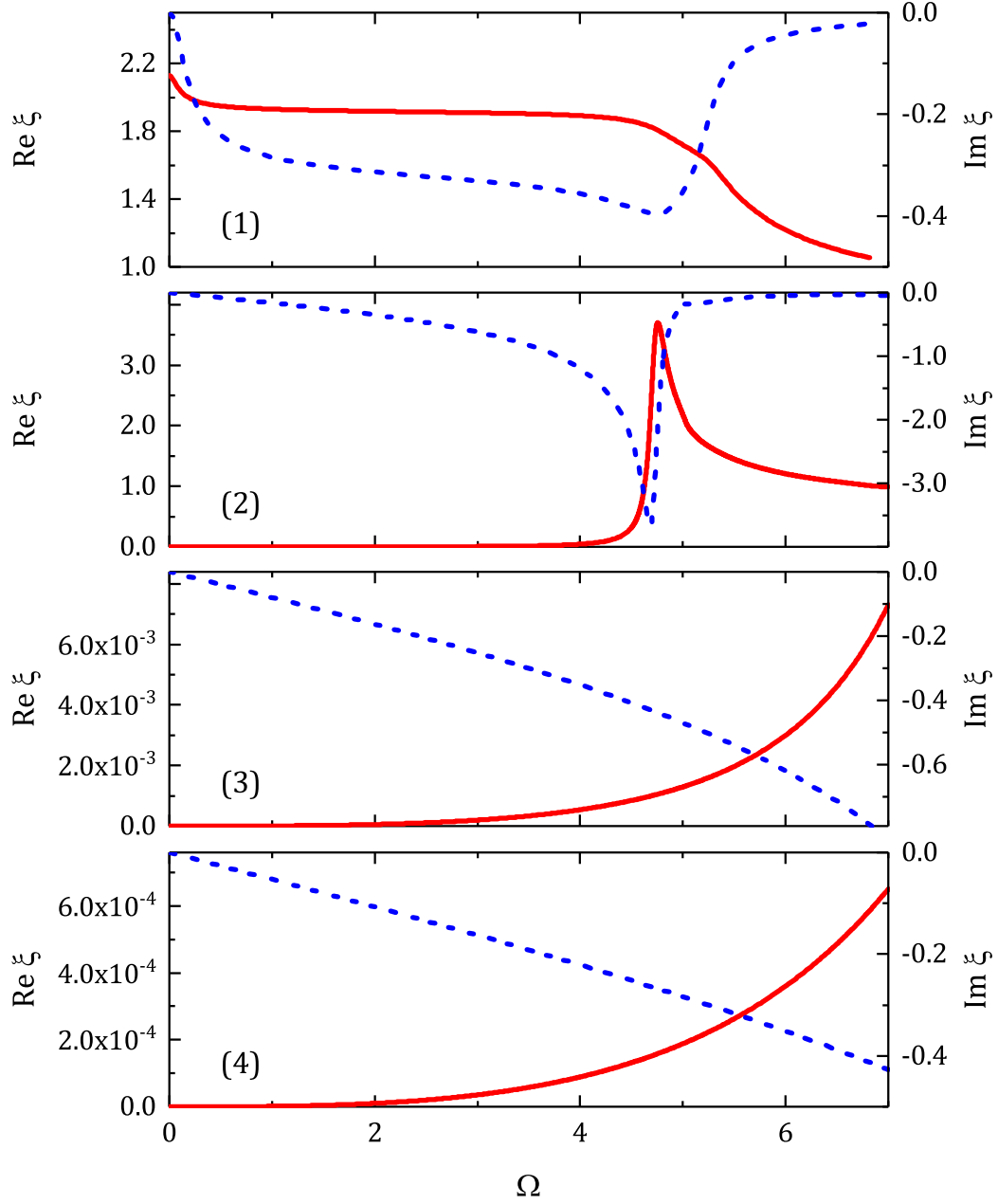
FIGURE 2.5. Frequency dependence of the first four complex roots of the dispersion equation (2.61) for a water channel between two brass plates. The real and imaginary parts of each root are shown with solid red and dashed blue curves, respectively.

the ordinal number $n$ to satisfy the ordering Im $\beta_n <$ Im $\beta_{n+1}$. The first complex root has a negligible imaginary part at low frequencies. Because of that, the corresponding weakly leaky mode contributes to subwavelength transmission of sound through the metal plates and can compete with the transmission through the channel via the slow Rayleigh mode.

Note that in the limit of zero channel width there must be a quasi-longitudinal Rayleigh mode. Such mode should be only a slight modification of a pure longitudinal wave that propagates in the bulk of the solid. Obviously, none of the real Rayleigh eigenmodes fits this role as their phase speeds are smaller that $c_t$ ($\xi \leq 1$). This means that a pure longitudinal wave cannot propagate in a solid plate with a slit: the longitudinal vibrations lead to the inevitable shear displacements in the solid in the vicinity of the slit. The corresponding Rayleigh eigenmode must then be necessarily complex and, actually, the first leaky mode is the eigenmode in question. Indeed, in the limit of zero frequency the real part of its phase speed approaches Re $\xi = c_l/c_t$, which exactly corresponds to the speed of longitudinal waves, and its imaginary part vanishes. Consequently, when considering the transmission of sound through a finite sample, the first leaky mode will be responsible for the maxima in the transmission spectrum that would resemble the Fabry-Perot maxima for the bulk plate of the same thickness.

### 2.4.5. Eigenmode Orthogonality

An eigenmode (eigenfunction) $f_n$ of a physical system is always a nontrivial solution of a certain *homogeneous* problem, in which there is no external influence on the system. The set of eigenmodes forms a complete basis in the function space. Then any process (given by a function $f$) occurring in the system can be represented as a superposition of the eigenmodes, or in other words, it can be expanded over the known basis:

$$(2.62) \qquad\qquad f = \sum C_n f_n.$$

The coefficients of the expansion can easily be found if the eigenmodes are orthogonal:

$$(2.63) \qquad\qquad \langle f_n, f_m \rangle = ||f_n||^2 \delta_{n,m}.$$

Here the term in the left-hand side is a generalized inner product of two eigenmodes, $||\cdot||$ gives the norm of its argument, and $\delta_{n,m}$ is the Kronecker symbol. The coefficients of the expansion $C_m$ are then immediately obtained as

$$(2.64) \qquad C_m = \frac{\langle f, f_m \rangle}{||f_m||^2}.$$

For the problem of sound transmission through a finite-sized fluid channel between two metal plates, determining the unknown coefficients in the expansion of the signal over the coupled Rayleigh modes will be crucial for obtaining the solution. However, the Rayleigh eigenmodes are not orthogonal, for the reason that the boundary conditions at the fluid-solid interface (2.44) explicitly contain the wavevector $\beta$ [9]. Moreover, the eigenmodes of any problem where the elastic waves are confined to a finite volume are known to be nonorthogonal. For example, the Lamb waves (normal vibrations) in an elastic slab are not mutually orthogonal over the slab width [59]. Even though a lot of efforts were put to redefine the orthogonality for Lamb waves from the reciprocity principles [9, 5, 107, 26], the proposed new relations do not facilitate calculating the coefficients of the expansion $C_m$.

The nonorthogonal basis can always be transformed into an orthogonal one by, e.g., employing the Gram-Schmidt procedure, however, I will not be using this procedure for several reasons. One of them is that this orthogonalization process is quite difficult to perform in regards to the Rayleigh eigenmodes, and using it would significantly increase the complexity of the problem. Another reason is that it will be much easier to calculate the unknown coefficients $C_m$ if one expands both the function $f$ and the eigenmodes $f_n$ over some simple orthogonal basis $g_n$:

$$(2.65) \qquad f = \sum f^{(m)} g_m, \qquad f_n = \sum f_n^{(m)} g_m,$$

with the coefficients $f^{(m)}$ and $f_n^{(m)}$, respectively. After substituting the latter relations to (2.62) and calculating the inner product with every $g_m$ for each part of the equation, the following set of equations is obtained:

$$(2.66) \qquad f^{(m)} = \sum C_n f_n^{(m)}.$$

The linear system can now be solved numerically, for example. This discussion clearly shows that the use of the nonorthogonal basis is not too much of an inconvenience in solving a problem.

## 2.5. Scattering Problem

The knowledge of the eigenmodes of the infinite fluid channel allows to tackle the problem of sound transmission through a finite sample. Namely, the acoustic field inside the channel and the plates can be now expressed as a superposition of the channel eigenmodes. In this approach the boundary conditions at the channel walls are automatically satisfied. Also, one obtains a practically exact analytical solution since the acoustic potentials account for the *total* field at any given point.

The only limiting factor here is the number of the eigenmodes used in the potentials expansion. The exact solution requires writing an infinite series over all possible eigenmodes. Practically, the series in question converges quite fast and it is sufficient to consider only the first few of the coupled Rayleigh eigenmodes.

### 2.5.1. Geometry

I will be considering a problem that closely imitates the conditions of the experiment reported in [30]. In this experiment, two brass or aluminum plates of length $L = 12$ cm and thickness $h$ were separated by a distance $d$ (the slit aperture). The system was immersed in a water tank, and two transducers of diameter $2R_d = 1.5''$ were used to produce and detect the sound. Both transducers were positioned at a distance $l = 8$ cm from the plates, centered with respect to the channel, and the sound was incident normally on the slit. This experimental setup is schematically shown in Fig. 2.6, as well as the values of $d$ and $h$ for which the experiment was performed. Note that the gravity is acting along the $y$-direction. Any effect of gravity is, however, omitted and the problem is assumed uniform along the $y$-axis.

Since the size of each transducer is much larger than the channel width, $d \ll R_d$, I will model the incoming sound by a plane wave.
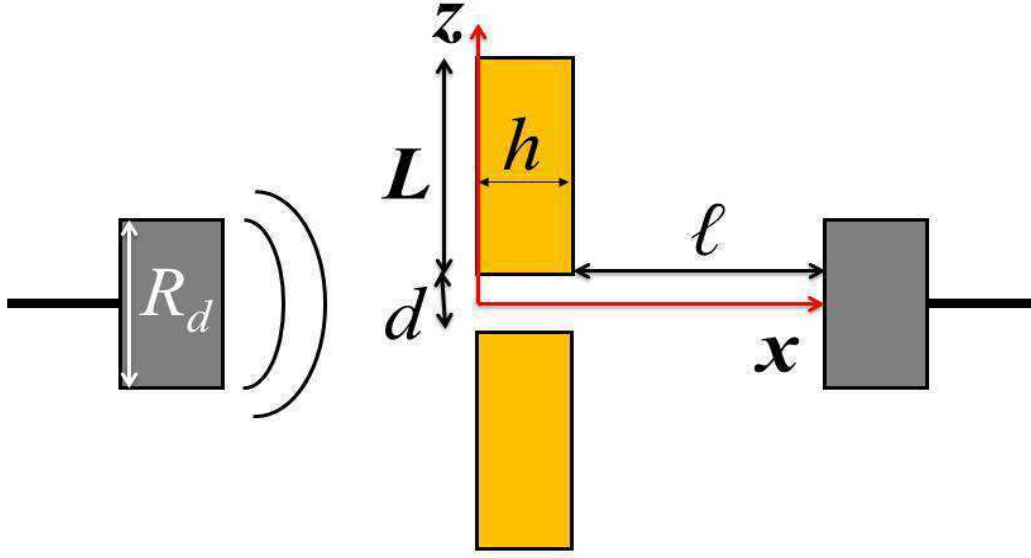
FIGURE 2.6. Experimental setup showing the geometrical parameters of the fluid channel between the metal plates and the configuration of transducers.

### 2.5.2. Acoustic Potentials of Transmitted and Reflected Waves

The plane acoustic wave that is normally incident on the slit and the plates from the left is described by the acoustic potential $(p_0/i\omega\rho_f)\exp(ik_f x - i\omega t)$. The reflected and the transmitted acoustic fields are denoted as $R(x, z)$ $(x < 0)$ and $T(x, z)$ $(x > h)$, respectively. Since the channel scatters the sound in every possible direction, I write the potentials $R(x, z)$ and $T(x, z)$ as Fourier integrals

$$(2.67) \qquad R(x, z) = \int_{-\infty}^{+\infty} r(k)e^{ikz - i\beta(k)x}dk, \qquad x \leq 0,$$

$$(2.68) \qquad T(x, z) = \int_{-\infty}^{+\infty} t(k)e^{ikz + i\beta(k)(x-h)}dk, \qquad x \geq h,$$

where the amplitudes $r(k)$ and $t(k)$ are

$$(2.69) \qquad r(k) = \frac{1}{2\pi}\int_{-\infty}^{+\infty} R(0, z)e^{-ikz}dz,$$

31

$$(2.70) \qquad t(k) = \frac{1}{2\pi} \int\limits_{-\infty}^{+\infty} T(h,z)e^{-ikz}dz.$$

The longitudinal (along $x$) component of the wave vector is defined as $\beta(k) = \sqrt{k_f^2 - k^2}$ for $|k| < k_f$ and $\beta(k) = i\sqrt{k^2 - k_f^2}$ for $|k| > k_f$. Each Fourier integrals essentially represents a combination of all possible plane ($|k| < k_f$) and evanescent ($|k| > k_f$) waves that contribute to either reflection or transmission.

In the region $0 \leq x \leq h$, i.e., inside the fluid channel and the elastic plates, the potentials are superpositions of forward and backward propagating eigenmodes of the corresponding infinite channel:

$$(2.71) \qquad B(x,z) = \sum_n (b_n^+ e^{i\beta_n x} + b_n^- e^{-i\beta_n x})\cos k_n z, \qquad\qquad |z| < d/2,$$

$$(2.72) \qquad L(x,z) = \sum_n (l_n^+ e^{i\beta_n x} + l_n^- e^{-i\beta_n x})e^{-\nu_n|z|}, \qquad\qquad |z| > d/2,$$

$$(2.73) \qquad S(x,z) = \sum_n (s_n^+ e^{i\beta_n x} - s_n^- e^{-i\beta_n x})e^{-\eta_n|z|}, \qquad\qquad |z| > d/2.$$

The summation runs over all possible eigenmodes (propagating and leaky) of the system for a given frequency. The superindices "+" and "−" indicate propagation in the $+x$ or $-x$ direction. The potentials for the backpropagating Rayleigh waves are obtained from those describing the propagation forward by applying the symmetry transformation $x \to -x$, $y \to -y$, which is essentially the $180^o$ rotation around the $z$-axis.

The unknown amplitudes $t(k)$ and $r(k)$ in (2.67)-(2.68) and the coefficients $b_n$, $l_n$, and $s_n$ in (2.71)-(2.73) can be determined after the appropriate boundary conditions at both vertical ($x = 0, h$) surfaces of the structure are established.

2.5.3. Solution of the Scattering Problem

The coefficients $l_n^{\pm}$, $s_n^{\pm}$, and $b_n^{\pm}$ describe a particular coupled Rayleigh wave, so the relationship between them is established by (2.44), namely,

$$(2.74) \qquad l_n^{\pm} = -\frac{ik_n c_t^2}{\nu_n \omega^3}(\eta_n^2 + \beta_n^2)\sin\frac{k_n d}{2}e^{\nu_n d/2}b_n^{\pm},$$

$$(2.75) \qquad s_n^{\pm} = -\frac{2k_n \beta_n c_t^2}{\omega^3} \sin \frac{k_n d}{2} e^{\eta_n d/2} b_n^{\pm}.$$

Both (2.74) and (2.75) can now be used to eliminate the unknown coefficients $l_n^{\pm}$ and $s_n^{\pm}$ of the acoustic potentials in plates from all subsequent calculations. The remaining unknowns $t(k)$, $r(k)$, and $b_n^{\pm}$ need to be related via the boundary conditions at the vertical boundaries $x = 0$ and $x = h$ that were not used so far. These four conditions for velocity and pressure are as follows:

$$(2.76) \qquad p_0 + i\omega\rho_f \left. R(x,z)\right|_{x=0} = \begin{bmatrix} i\omega\rho_f B\,(x,z)|_{x=0}, & |z| < d/2, \\[2mm] \sigma_{xx}\,(x,z)|_{x=0}, & |z| > d/2, \end{bmatrix}$$

$$(2.77) \qquad \frac{p_0}{\rho_f c_f} + \left.\frac{\partial R(x,z)}{\partial x}\right|_{x=0} = \begin{bmatrix} \left.\dfrac{\partial B(x,z)}{\partial x}\right|_{x=0}, & |z| < d/2, \\[3mm] -i\omega\, u_x(x,z)|_{x=0}, & |z| > d/2, \end{bmatrix}$$

$$(2.78) \qquad i\omega\rho_f \left. T(x,z)\right|_{x=h} = \begin{bmatrix} i\omega\rho_f B\,(x,z)|_{x=h}, & |z| < d/2, \\[2mm] -\sigma_{xx}\,(x,z)|_{x=h}, & |z| > d/2, \end{bmatrix}$$

$$(2.79) \qquad \left.\frac{\partial T(x,z)}{\partial x}\right|_{x=h} = \begin{bmatrix} \left.\dfrac{\partial B(x,z)}{\partial x}\right|_{x=h}, & |z| < d/2, \\[3mm] -i\omega\, u_x(x,z)|_{x=h}, & |z| > d/2. \end{bmatrix}$$

Here the acoustic field for $x < 0$ is a sum of the incident and reflected fields, the displacement vector $u_i$ and the stress tensor $\sigma_{ij}$ are calculated from the potentials (2.72)-(2.73) using the definitions (2.22) and (2.23).

Now the potentials $R(x,z)$, $T(x,z)$, and $B(x,z)$ in their explicit forms (2.71)-(2.73)

33

can be substituted into the boundary conditions (2.76)-(2.79):

(2.80)

$$
\frac{p_0}{i\omega\rho_f} + \int\limits_{-\infty}^{+\infty} r(k)e^{ikz}dk =
\begin{cases}
\displaystyle\sum_{n=1}^{\infty}(b_n^+ + b_n^-)\cos k_n z, & |z| < d/2, \\[2ex]
\displaystyle\frac{1}{i\omega\rho_f}\sum_{n=1}^{\infty}(l_n^+ + l_n^-)\left(\lambda k_l^2 + 2\mu\beta_n^2\right)e^{-\nu_n|z|}- \\[2ex]
\displaystyle\quad -\frac{2\mu}{\omega\rho_f}\sum_{n=1}^{\infty}\eta_n\beta_n(s_n^+ + s_n^-)e^{-\eta_n|z|}, & |z| > d/2,
\end{cases}
$$

(2.81)

$$
\frac{p_0}{ic_f\rho_f} - \int\limits_{-\infty}^{+\infty} r(k)\beta(k)e^{ikz}dk =
\begin{cases}
\displaystyle\sum_{n=1}^{\infty}(b_n^+ - b_n^-)\beta_n\cos k_n z, & |z| < d/2, \\[2ex]
\displaystyle-i\omega\sum_{n=1}^{\infty}(l_n^+ - l_n^-)\beta_n e^{-\nu_n|z|} - \omega\sum_{n=1}^{\infty}(s_n^+ - s_n^-)\eta_n e^{-\eta_n|z|}, & |z| > d/2,
\end{cases}
$$

(2.82)

$$
\int\limits_{-\infty}^{+\infty} t(k)e^{ikz}dk =
\begin{cases}
\displaystyle\sum_{n=1}^{\infty}(b_n^+ e^{i\beta_n h} + b_n^- e^{-i\beta_n h})\cos k_n z, & |z| < d/2, \\[2ex]
\displaystyle\frac{1}{i\omega\rho_f}\sum_{n=1}^{\infty}(l_n^+ e^{i\beta_n h} + l_n^- e^{-i\beta_n h})\left(\lambda k_l^2 + 2\mu\beta_n^2\right)e^{-\nu_n|z|}- \\[2ex]
\displaystyle\quad -\frac{2\mu}{\omega\rho_f}\sum_{n=1}^{\infty}\eta_n\beta_n(s_n^+ e^{i\beta_n h} + s_n^- e^{-i\beta_n h})e^{-\eta_n|z|}, & |z| > d/2,
\end{cases}
$$

(2.83)

$$
\int\limits_{-\infty}^{+\infty} t(k)\beta(k)e^{ikz}dk =
\begin{cases}
\displaystyle\sum_{n=1}^{\infty}(b_n^+ e^{i\beta_n h} - b_n^- e^{-i\beta_n h})\beta_n\cos k_n z, & |z| < d/2, \\[2ex]
\displaystyle-i\omega\sum_{n=1}^{\infty}(l_n^+ e^{i\beta_n h} - l_n^- e^{-i\beta_n h})\beta_n e^{-\nu_n|z|}- \\[2ex]
\displaystyle\quad -\omega\sum_{n=1}^{\infty}(s_n^+ e^{i\beta_n h} - s_n^- e^{-i\beta_n h})\eta_n e^{-\eta_n|z|}, & |z| > d/2.
\end{cases}
$$

Next, one needs to eliminate the unknown functions $r(k)$ and $t(k)$. This can be done, e.g., by calculating the inverse Fourier transforms (see (2.69)-(2.70)) of equations (2.81) and

34

(2.83), which give

(2.84)

$$
r(k) = \frac{p_0}{i\omega\rho_f}\delta(k) - \frac{1}{2\pi}\sum_{n=1}^{N}\frac{\beta_n}{\beta(k)}(b_n^+ - b_n^-)\left[\left(\frac{\sin((k_n+k)d/2)}{k_n+k} + \frac{\sin((k_n-k)d/2)}{k_n-k}\right) - \frac{2k_n c_t^2(\eta_n^2+\beta_n^2)}{\nu_n\omega^2}\sin\frac{k_n d}{2}\mathcal{F}(k,\nu_n) + \frac{4\eta_n k_n c_t^2}{\omega^2}\sin\frac{k_n d}{2}\mathcal{F}(k,\eta_n)\right],
$$

and

(2.85)

$$
t(k) = \frac{1}{2\pi}\sum_{n=1}^{N}\frac{\beta_n}{\beta(k)}(b_n^+ e^{i\beta_n h} - b_n^- e^{-i\beta_n h})\left[\left(\frac{\sin((k_n+k)d/2)}{k_n+k} + \frac{\sin((k_n-k)d/2)}{k_n-k}\right) - \frac{2k_n c_t^2(\eta_n^2+\beta_n^2)}{\nu_n\omega^2}\sin\frac{k_n d}{2}\mathcal{F}(k,\nu_n) + \frac{4\eta_n k_n c_t^2}{\omega^2}\sin\frac{k_n d}{2}\mathcal{F}(k,\eta_n)\right].
$$

The equations (2.74) and (2.75) were used to express the coefficients $l_n^{\pm}$ and $s_n^{\pm}$ in terms of $b_n^{\pm}$, and the function $\mathcal{F}(k,\varkappa)$ is denoting the integral

(2.86)
$$
\mathcal{F}(k,\varkappa) = \frac{e^{\varkappa d/2}}{2}\left(\int_{-\infty}^{-d/2}e^{-ikz+\varkappa z}dz + \int_{+d/2}^{+\infty}e^{-ikz-\varkappa z}dz\right) =
$$
$$
= \frac{1}{k^2+\varkappa^2}\left(\varkappa\cos\frac{kd}{2} - k\sin\frac{kd}{2}\right).
$$

The evaluation of this integral for real and complex values of $\varkappa$ is discussed in detail in Appendix B.

After the amplitudes $r(k)$ and $t(k)$ in (2.80) and (2.82) are replaced with their respective series (2.84)-(2.85), one obtains the two equations that contain only the unknowns $b_n^+$ and $b_n^-$:

(2.87)

$$
\frac{2p_0}{i\omega\rho_f} - \frac{1}{2\pi}\sum_{n=1}^{\infty}(b_n^+ - b_n^-)\int_{-\infty}^{+\infty}\frac{\beta_n}{\beta(k)}\left[\frac{\sin((k_n+k)d/2)}{k_n+k} + \frac{\sin((k_n-k)d/2)}{k_n-k} - \right.
$$
$$
\left. - \frac{2k_n c_t^2(\eta_n^2+\beta_n^2)}{\nu_n\omega^2(\nu_n^2+k^2)}\sin\frac{k_n d}{2}\left(\nu_n\cos\frac{kd}{2} - k\sin\frac{kd}{2}\right) + \right.
$$

$$+\frac{4\eta_n k_n c_t^2}{\omega^2(\eta_n^2+k^2)}\sin\frac{k_n d}{2}\left(\eta_n\cos\frac{kd}{2}-k\sin\frac{kd}{2}\right)\Bigg]e^{ikz}dk=$$

$$=\begin{cases}\displaystyle\sum_{n=1}^{\infty}(b_n^++b_n^-)\cos k_n z, & |z|<d/2,\\[2em]\displaystyle-\sum_{n=1}^{\infty}\frac{k_n c_t^2}{\omega^4\rho_f}(b_n^++b_n^-)\sin\frac{k_n d}{2}\left[\frac{\eta_n^2+\beta_n^2}{\nu_n}\left(\lambda k_l^2+2\mu\beta_n^2\right)e^{-\nu_n(|z|-\frac{d}{2})}-4\mu\eta_n\beta_n^2 e^{-\eta_n(|z|-\frac{d}{2})}\right], & |z|>d/2,\end{cases}$$

(2.88)

$$\frac{1}{2\pi}\sum_{n=1}^{\infty}(b_n^+ e^{i\beta_n h}-b_n^- e^{-i\beta_n h})\int_{-\infty}^{+\infty}\frac{\beta_n}{\beta(k)}\left[\frac{\sin((k_n+k)d/2)}{k_n+k}+\frac{\sin((k_n-k)d/2)}{k_n-k}-\right.$$

$$-\frac{2k_n c_t^2(\eta_n^2+\beta_n^2)}{\nu_n\omega^2(\nu_n^2+k^2)}\sin\frac{k_n d}{2}\left(\nu_n\cos\frac{kd}{2}-k\sin\frac{kd}{2}\right)+$$

$$\left.+\frac{4\eta_n k_n c_t^2}{\omega^2(\eta_n^2+k^2)}\sin\frac{k_n d}{2}\left(\eta_n\cos\frac{kd}{2}-k\sin\frac{kd}{2}\right)\right]e^{ikz}dk=$$

$$=\begin{cases}\displaystyle\sum_{n=1}^{\infty}(b_n^+ e^{i\beta_n h}+b_n^- e^{-i\beta_n h})\cos k_n z,\ |z|<d/2,\\[2em]\displaystyle-\sum_{n=1}^{\infty}\frac{k_n c_t^2}{\omega^4\rho_f}(b_n^+ e^{i\beta_n h}+b_n^- e^{-i\beta_n h})\sin\frac{k_n d}{2}\times\\[2em]\displaystyle\qquad\times\left[\frac{\eta_n^2+\beta_n^2}{\nu_n}\left(\lambda k_l^2+2\mu\beta_n^2\right)e^{-\nu_n(|z|-\frac{d}{2})}-4\mu\eta_n\beta_n^2 e^{-\eta_n(|z|-\frac{d}{2})}\right],\ |z|>d/2.\end{cases}$$

In the latter equations, however, both sides are still functions of $z$. If the coupled Rayleigh modes were orthogonal to each other, one would be able to multiply each equation by a certain function, describing the conjugate of an $n'$-th eigenmode, and integrate over $z$-axis. By doing this, all terms proportional to $b_n^{\pm}$, $n\neq n'$ would identically vanish and only the amplitudes $b_{n'}^{\pm}$ would remain in each equation. Solving the two linear equations with two unknowns $b_{n'}^+$ and $b_{n'}^-$ is then trivial, and all remaining unknowns are found in exactly the same fashion.

Unfortunately, the Rayleigh eigenmodes are not orthogonal, so attempting to derive an equation for the amplitudes of a specific eigenmode may present a considerable difficulty. Instead, I will expand (2.87) and (2.88) in series over some *orthogonal* basis, e.g., the basis

of trigonometric functions. Ultimately, the transmission through the system is determined by the total intensity detected by the transducer of radius $R_d$. Thus in the region $|z| \leq R_d$ a Fourier transform

$$(2.89) \qquad f(z) = \frac{F_0}{2} + \sum_{m=1}^{\infty} F_m \cos\left(\frac{\pi m}{R_d} z\right), \quad |z| < R_d,$$

with the coefficients

$$(2.90) \qquad F_m = \frac{2}{R_d} \int_0^{R_d} f(z) \cos\left(\frac{\pi m}{R_d} z\right) dz,$$

can be used to represent any even function $f(z)$. The equality of two functions on $|z| \leq R_d$ is then guaranteed if their respective Fourier coefficients (2.90) are equal. Also, the total number of unknown coefficients in (2.87)-(2.88) is $2N$, where $N$ is the number of eigenmodes with phase speeds $\xi_n(\omega)$ used in the potentials expansion, so it is sufficient to consider only the first $N$ $(m = 0, ..., N-1)$ Fourier coefficients (2.90).

With that, one arrives at the $2N \times 2N$ system of inhomogeneous linear equations for the unknowns $b_n^{\pm}$:

(2.91)

$$\frac{2p_0}{i\omega\rho_f} R_d \delta_{m,0} - \frac{1}{2\pi} \sum_{n=1}^{N} (b_n^+ - b_n^-) \int_{-\infty}^{+\infty} \frac{\beta_n}{\beta(k)} \left[ \frac{\sin((k_n+k)d/2)}{k_n+k} + \frac{\sin((k_n-k)d/2)}{k_n-k} - \right.$$

$$-\frac{2k_n c_t^2(\eta_n^2 + \beta_n^2)}{\nu_n \omega^2(\nu_n^2 + k^2)} \sin\frac{k_n d}{2} \left(\nu_n \cos\frac{kd}{2} - k \sin\frac{kd}{2}\right) +$$

$$\left. + \frac{4\eta_n k_n c_t^2}{\omega^2(\eta_n^2 + k^2)} \sin\frac{k_n d}{2} \left(\eta_n \cos\frac{kd}{2} - k \sin\frac{kd}{2}\right) \right] \left(\int_0^{R_d} e^{ikz} \cos\frac{\pi m z}{R_d} dz\right) dk =$$

$$= \sum_{n=1}^{N} (b_n^+ + b_n^-) \left[ \left(\int_0^{d/2} \cos k_n z \cos\frac{\pi m z}{R_d} dz\right) - \right.$$

$$\left. - \frac{k_n c_t^2}{\nu_n \omega^4 \rho_f} (\eta_n^2 + \beta_n^2) \left(\lambda k_l^2 + 2\mu\beta_n^2\right) \sin\frac{k_n d}{2} \left(\int_{d/2}^{R_d} e^{-\nu_n(|z|-\frac{d}{2})} \cos\frac{\pi m z}{R_d} dz\right) + \right.$$

37

$$+\frac{4\mu\eta_n k_n \beta_n^2 c_t^2}{\omega^4 \rho_f}\sin\frac{k_n d}{2}\left(\int_{d/2}^{R_d}e^{-\eta_n(|z|-\frac{d}{2})}\cos\frac{\pi m z}{R_d}dz\right)\Bigg]\,,\ m=0,1,2,\ldots,N-1,$$

(2.92)

$$\frac{1}{2\pi}\sum_{n=1}^{N}(b_n^+ e^{i\beta_n h}-b_n^- e^{-i\beta_n h})\int_{-\infty}^{+\infty}\frac{\beta_n}{\beta(k)}\Bigg[\frac{\sin((k_n+k)d/2)}{k_n+k}+\frac{\sin((k_n-k)d/2)}{k_n-k}-$$

$$-\frac{2k_n c_t^2(\eta_n^2+\beta_n^2)}{\nu_n\omega^2(\nu_n^2+k^2)}\sin\frac{k_n d}{2}\left(\nu_n\cos\frac{kd}{2}-k\sin\frac{kd}{2}\right)+$$

$$+\frac{4\eta_n k_n c_t^2}{\omega^2(\eta_n^2+k^2)}\sin\frac{k_n d}{2}\left(\eta_n\cos\frac{kd}{2}-k\sin\frac{kd}{2}\right)\Bigg]\left(\int_0^{R_d}e^{ikz}\cos\frac{\pi m z}{R_d}dz\right)dk=$$

$$=\sum_{n=1}^{N}(b_n^+ e^{i\beta_n h}+b_n^- e^{-i\beta_n h})\Bigg[\left(\int_0^{d/2}\cos k_n z\cos\frac{\pi m z}{R_d}dz\right)-$$

$$-\frac{k_n c_t^2}{\nu_n\omega^4\rho_f}(\eta_n^2+\beta_n^2)\left(\lambda k_l^2+2\mu\beta_n^2\right)\sin\frac{k_n d}{2}\left(\int_{d/2}^{R_d}e^{-\nu_n(|z|-\frac{d}{2})}\cos\frac{\pi m z}{R_d}dz\right)+$$

$$+\frac{4\mu\eta_n k_n \beta_n^2 c_t^2}{\omega^4\rho_f}\sin\frac{k_n d}{2}\left(\int_{d/2}^{R_d}e^{-\eta_n(|z|-\frac{d}{2})}\cos\frac{\pi m z}{R_d}dz\right)\Bigg]\,,m=0,1,2,\ldots,N-1.$$

The coefficients $b_n^\pm$ are found by solving the obtained system numerically. The solution of the system is unique due to the inhomogeneous terms which represent the incident plane wave. Then, from (2.84)-(2.85) one immediately finds the reflected and transmitted amplitudes $r(k)$ and $t(k)$, i.e., the total reflected (2.67) and transmitted (2.68) acoustic fields are now known.

## 2.6. Transmission, Reflection and Redirection of Sound

### 2.6.1. Comparison of the Theoretical Results with the Experiment

In order to compare the experimental transmission spectra [30] with the theoretical ones, the transmission coefficient must be properly defined first. The conditions of the experiment imply that only the energy flux towards the transducer surface is detected, so
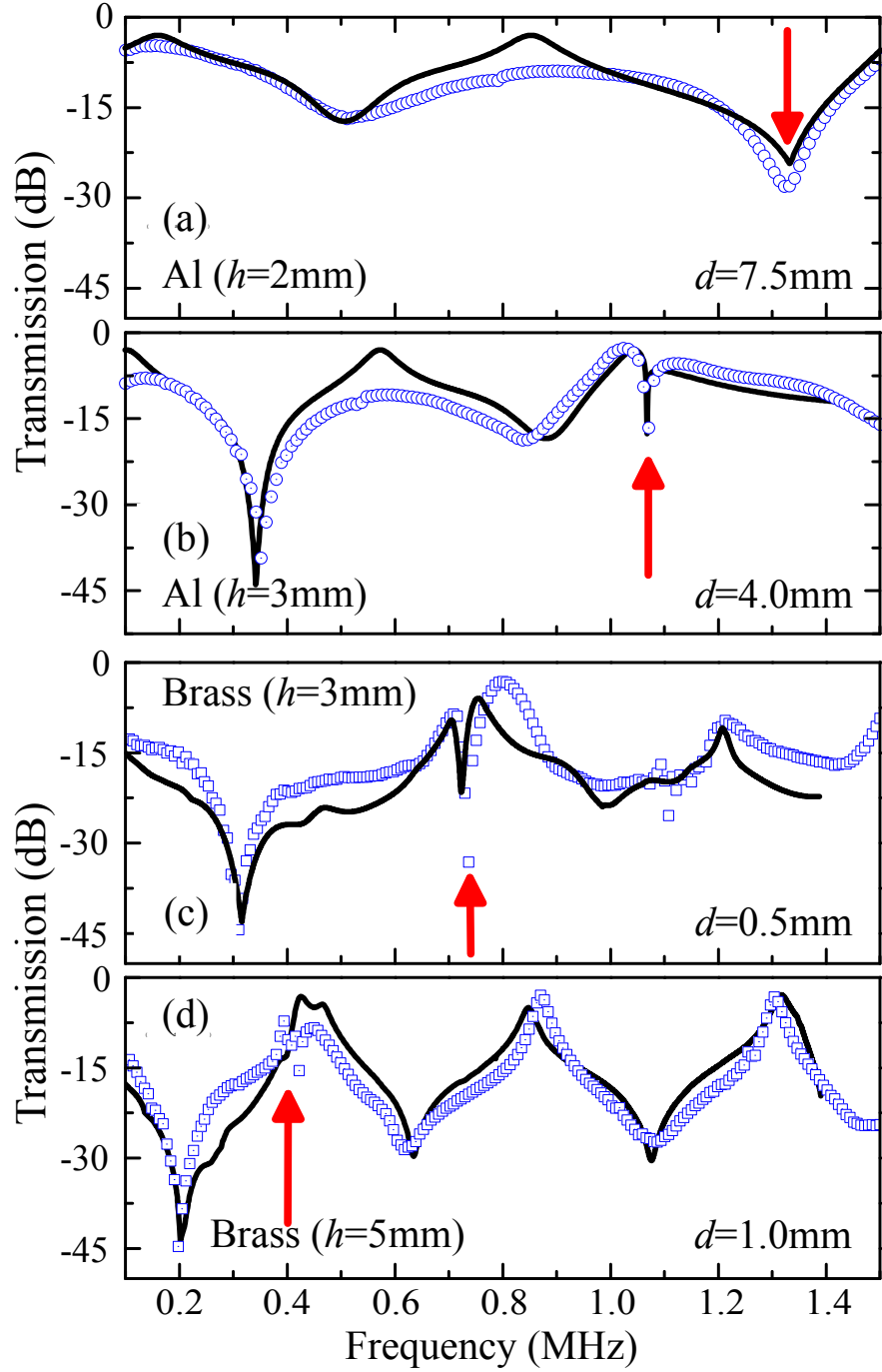
FIGURE 2.7. Sound transmission spectra of a water slit between two aluminum (a,b) and brass (c,d) plates. Experimental results are shown by circles for aluminum and by squares for brass. Calculated spectra are shown by solid lines. The vertical arrows mark the minima due to the excitation of the slow mode.

the transmission coefficient should be calculated as

$$(2.93) \qquad \mathcal{T}_{\parallel}(\omega) = \frac{1}{A p_0 v_{0x}} \int_A I_x(x=l,z) dy dz = \frac{1}{\pi R_d^2 p_0 v_{0x}} \int_{-R_d}^{R_d} I_x(x=l,z)\sqrt{R_d^2 - z^2} dz.$$

Here $A = \pi R_d^2$ is the area of the transducer antenna, $l = 8$ cm is the $x$-coordinate of the receiver, $p_0 v_{0x}$ is the energy flux in the incident wave, and

$$(2.94) \qquad I_x = p(x,z)v_x^*(x,z) = i\omega \rho_f T(x,z)\frac{\partial T^*(x,z)}{\partial x}$$

is the $x$-component of the transmitted acoustic flux.

As shown in the Fig. 2.7, the theoretical spectra given by (2.93) agree remarkably well with the experimental data in a wide frequency range for a water ($\rho_f = 1000$ kg/m$^3$, $c_f = 1500$ m/s) channel. The fine structure of the spectra and the correct depth of the minima observed at the frequencies indicated by the arrows are also recovered. The agreement is preserved when the length and width of the channel are varied to simulate both short and wide channels, $h < d$, Fig. 2.7 (a,b), and long and narrow ones, $d < h$, Fig. 2.7 (c,d), and also when the material of the plates is alternated between brass ($\rho_m = 8400$ kg/m$^3$, $c_t = 2000$ m/s, $c_l = 4250$ m/s) and aluminum ($\rho_m = 2700$ kg/m$^3$, $c_t = 3130$ m/s, $c_l = 6230$ m/s).

Indeed, as long as the linear Hooke's law is applicable and the viscous effects are negligible, the calculations outlined above are guaranteed to be exact since they are based on the exact solutions of the wave equations. The stress-strain relationship is, of course, linear if the amplitudes of the incident wave and, consequently, of the media vibrations are not too large. As for the viscous phenomena, it is known that they are manifested mainly within the viscous layers at the fluid-solid interfaces. In water with the viscosity coefficient $\nu = 0.01$ cm$^2$/s these layers have a typical thickness of approximately $\sqrt{2\nu/\omega} \approx 10^{-4}$ cm in the frequency range studied. The scale of the viscous layers then appear to be several orders of magnitude smaller than the scale of the channel, and for that reason, the accuracy of the obtained results practically does not suffer if the fluid is treated as inviscid.

The factor that impacts the accuracy the most is the number of eigenmodes that are accounted for in the series (2.71)-(2.73). As was mentioned earlier, any propagating eigenmode that exists for a given frequency must always be included. On the contrary,

among the infinite number of leaky modes choosing only the first few in the increasing order of their decay rates Im $\beta_n$ is sufficient. The actual number of leaky modes for each frequency is determined based on the convergence of the resulting transmission spectrum. Naturally, the series (2.71)-(2.73) converge slower for wider channels. This is due to the scaling $\omega_n \sim 1/d$ of the mode eigenfrequencies. For example, increasing the channel width $d$ red-shifts the cutoff frequencies (2.50) of the propagating fast modes, so for a wider channel a larger number of fast modes may emerge within the same frequency range. In other words, the wider the channel the more coupled Rayleigh modes it can support.

Specifically, the spectra shown in Fig. 2.7 (a)-(d) correspond to the channels which support up to 8, 5, 2, and 2 propagating Rayleigh modes, respectively, in the frequency range from 0.1 MHz to 1.4 MHz. The first of these modes is a slow mode that exists for any frequency, and the remaining fast modes start at their own cutoff frequencies (2.50). For the channel of width $d = 1.0$ mm between the two brass plates, for example, the fast mode with $n = 2$ emerges at the frequency 2.35 MHz, so obviously it cannot contribute to the transmission below 1.4 MHz. However, in the twice wider channel the same mode would appear at 1.17 MHz, and its contribution then could not be ignored. The number of leaky modes necessary to achieve convergence in the cases of Fig. 2.7 (a)-(d) was 11, 11, 7, and 7, respectively. The next leaky mode, if included in the calculations, leads to the variation in the result which is considerably less than 1%.

### 2.6.2. Redirection of Sound into Elastic Plates

Additional insights into the physical reasons for the extraordinary low transmission in Fig. 2.7 can be gained by the examination of how the acoustic energy is scattered in the system. For the water channel with $h = 3$ mm and $d = 0.5$ mm with the spectrum shown in Fig. 2.7(c) I calculate both the transmission and the reflection spectra. These two coefficients are redefined here in order to account for the total flux in the $x$-direction through the entire solid boundaries $x = 0$ and $x = h$:

$$(2.95) \qquad T_{\parallel} = 2\frac{i\omega\rho_f^2 c_f}{p_0^2 L} \int_{d/2}^{\infty} T(h, z) \left.\frac{\partial T^*(x, z)}{\partial x}\right|_{x=h} dz,$$

41
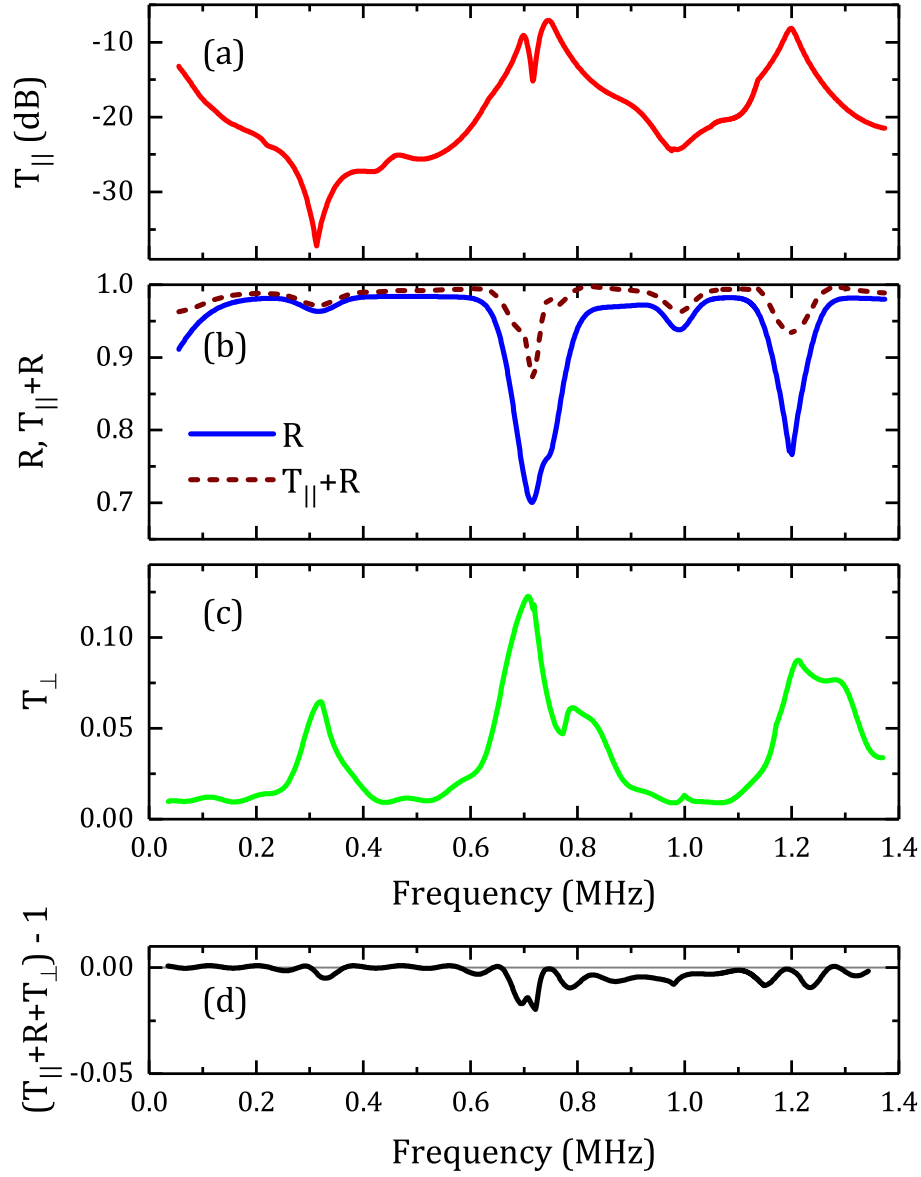
FIGURE 2.8. Calculated transmission and reflection spectra for two brass plates with sides of length $L = 12$ cm separated by a channel with $h = 3$ mm and $d = 0.5$ mm. (a) Transmission through the solid vertical boundary $x = h$ (solid red line) in log scale. (b) Reflection from the solid vertical boundary $x = 0$ (blue), and the sum $T_\parallel + R$ (brown dashed line). (c) Transmission through the horizontal boundary $z = d/2$. (d) The conservation of energy as demonstrated by the sum $T_\parallel + T_\perp + R$, which does not deviate from 1 by more than 2%.

$$(2.96) \qquad R = -2\frac{i\omega\rho_f^2 c_f}{p_0^2 L} \int_{d/2}^{\infty} R(0,z) \left.\frac{\partial R^*(x,z)}{\partial x}\right|_{x=0} dz.$$

Also, I calculate the flux that is transmitted from the water channel into the plates through the boundaries $z = \pm d/2$:

$$(2.97) \qquad T_\perp = 2\frac{i\omega\rho_f^2 c_f}{p_0^2 L} \int_0^h B(x,z) \left.\left(\frac{\partial B^*(x,z)}{\partial z}\right)\right|_{z=\frac{d}{2}} dx.$$

The three curves are shown in Fig. 2.8. Interestingly, at the frequencies where the minima in transmission are observed the reflection is also suppressed (see Fig. 2.8 (b)). Calculation of the sum of the fluxes exiting from either vertical side of the plate reveals that there must be an additional energy supplied to the plates as the sum $T_\parallel + R$ falls considerably below 1 for a wide range of frequencies. Clearly, this additional portion of energy has to be coming from the fluid channel through the channel walls. The spectrum of this vertical flux, $T_\perp$, is shown in Fig. 2.8 (c). The minima of $T_\parallel$ and $R$ coincide with the maxima of $T_\perp$, and the total flux that goes through the sides of the plates is very close to 1 which is expected as the total energy must be conserved in the system (see Fig. 2.8 (d)). The flux through the other end of the plate, at $z = \infty$, is negligible as all of the leaky Rayleigh modes carrying energy will necessarily be scattered through the vertical sides in a sufficiently long plate. The minor fluctuations of $T_\parallel + R + T_\perp$ around 1 are due to the numerical error that builds up during the calculations. The analysis performed here stresses that the channel system cannot be regarded as an aligned along $z$-axis 1D scatterer of acoustic waves.

The elastic nature of plates in the 2D system studied allows for an interesting ability to redirect the acoustic excitation into the plates. The waves in the plates may then propagate perpendicular to the direction of the incident wave. This feature can not be described in the models employing the rigid-body approximation which is quite commonly used in a great number of acoustic studies. Therefore, only the elastic screens have the capability to redirect sound into metal at an almost $90^o$ angle. The redirected flux can be observed to be as high as 12%, as can be seen from Fig. 2.8 (c) for the frequency of around 0.7 MHz. This is quite a strong effect, and the amount of redirected flux can be comparable with the flux
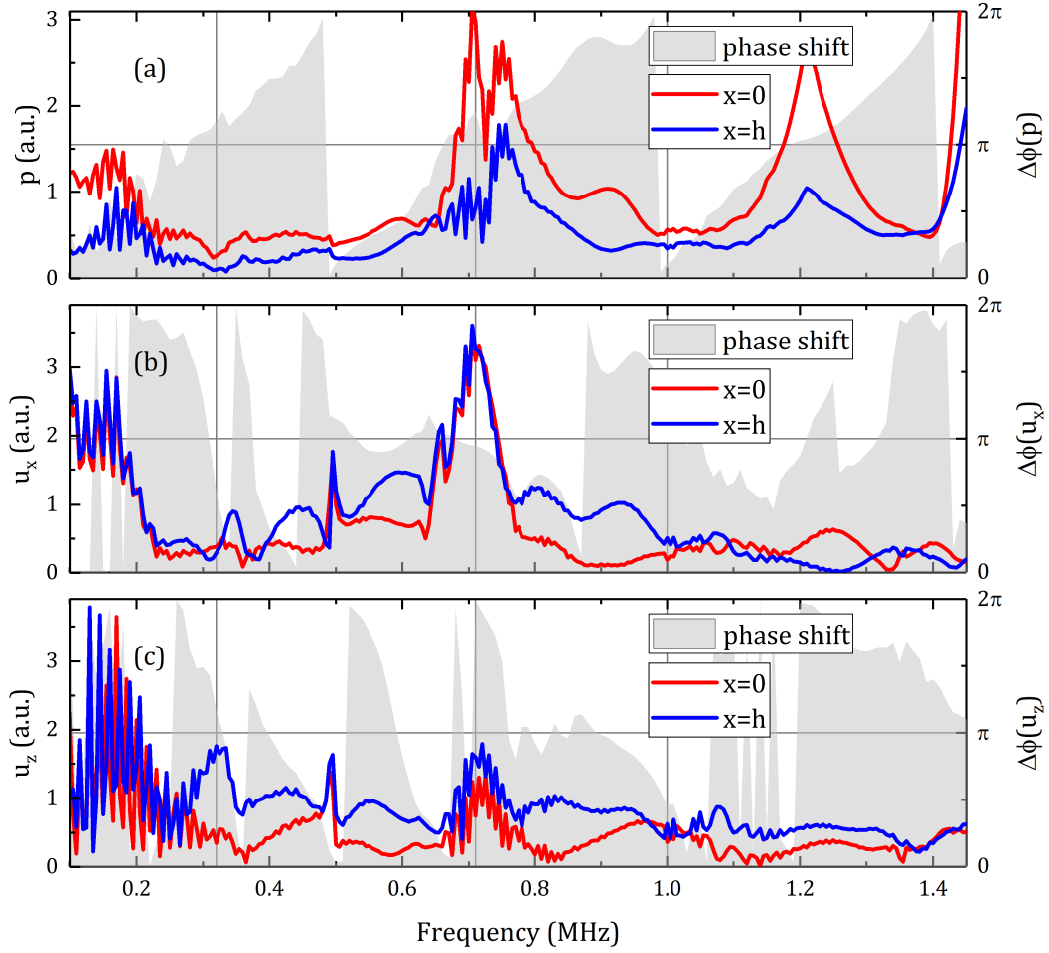
FIGURE 2.9. Frequency dependence of the pressure, $x$ and $z$ displacement of the plates at the left and right ends of the same channel as in Fig. 2.8. The solid curves show the amplitude of the respective quantity calculated at the points $x = 0$ (red) and $x = h$ (blue). The shaded regions represent the phase shifts $\Delta\phi(g) = \arg g|_{x=0} - \arg g|_{x=h}$ for each quantity $g = p, u_x, u_z$ whose amplitudes are plotted in the same panel. Straight vertical lines mark the positions of the deep minima in the transmission shown in Fig. 2.7 (c).

transmitted through a brass plate in water (as low as 8%, or $-11$ dB, for the frequency of the Fabry-Perot minimum).

In order to understand how individual Rayleigh eigenmodes enhance the radiation

of energy into the plates, I analyze frequency dependence of the pressure and both $x$- and $z$-components of the displacement vector evaluated at the corners of the channel ($x = 0, h$, and $z = d/2$). The respective graphs are visualized in Fig. 2.9. Each panel of the figure is dedicated to a certain physical quantity. The solid lines show the amplitudes of that quantity for either corner of the channel as a function of frequency, and the shaded area gives the relative phase shift between the two.

For the resonant frequencies that correspond to the minima in transmission (0.32 MHz, 0.71 MHz, and 0.98 MHz) the horizontal displacement appears to have very small amplitudes close to the first and third resonances (which are basically the Fabry-Perot minima). In the second resonance the amplitudes are quite large, and the phase shift is close to $\pi$, meaning the vibrations are out of phase. This corresponds to high transmission of sound, so the appearance of the dip must be caused by another factor. Namely, the pressure at both ends of the channel in the resonances is close to zero or exhibits a sharp dip. As for the vertical displacement, its contribution to the redirection of sound is due either to the amplitudes at each corner being close and in phase (close to 0 or $2\pi$), or one amplitude being much larger than the other.

Both the suppressed direct transmission and the suppressed reflection are necessary conditions to have the strong redirection of flux into the metal plates. This requires having simultaneously low pressure $p(x, z)$ and small amplitudes of horizontal vibrations $u_x(x, z)$ of the plate boundaries at the channel ends. Naturally, when the pressure minima occur at the same (or very close) frequencies as the displacement minima, the extraordinary low transmission of sound ensues. The sharpness of the dip in Fig. 2.7 correlates with the amount of energy being redirected. The closer the frequencies for which both $p$ and $u_x$ are low, and the closer these quantities are to zero, the sharper becomes the dip, and, consequently, the more energy veers into the metal. Moreover, it helps to have the local maxima for the $z$-component of the displacement at the resonant frequency to facilitate the redirection of energy into the metal. While the frequency dependence on every individual panel in Fig. 2.9 exhibits the described behavior for multiple frequencies, the effect builds up when

45

this behavior is manifested simultaneously, i.e., at the same frequency. For example, the third resonance is much broader than the other due to quite weak vertical oscillations of the plate boundaries.

Qualitatively, one can conclude about the strength of the effect based on how different eigenmodes propagating in opposite directions in the channel interfere to form standing (or, better to say, quasi-standing) waves across the length of the channel $h$. Indeed, since the propagating Rayleigh eigenmodes exhibit usual oscillating behavior along the $x$-axis, the low pressure at the channel ends occurs when the modes interfere destructively. Specifically, the most suppression of transmission results from the destructive interference of the eigenmode which would otherwise contribute the most to the transmission. If at the same frequency another eigenmode interferes destructively as well, the dip in the spectrum becomes even sharper. Even though it is possible to conclude how the modes interfere, it is, nevertheless, quite challenging to determine how much energy is redirected as a function of the channel geometry since it explicitly depends on the dispersion (2.47) of each involved Rayleigh eigenmode.

The two principal maxima in transmission, at 0.71 MHz and 1.22 MHz, are the maxima of the Fabry-Perot resonances, and they simply coincide with the minima in the reflection spectrum. Also, the amplitude of the transmitted pressure is quite large (see Fig. 2.9(a)). Since these Fabry-Perot maxima result from the constructive interference of the quasi-longitudinal leaky Rayleigh mode, their positions are strongly affected by the mode dispersion. The Fabry-Perot resonances of the bulk metal plate are equidistant in the frequency spectrum, where as for the system with the channel the maxima get closer to each other for higher frequencies. This is due to the phase speed of the quasi-longitudinal mode decreasing with frequency, as shown in Fig. 2.5.

In Fig. 2.7(c) the two minima in transmission at 0.32 MHz and 0.71 MHz in transmission arise due to the constructive interference of the propagating eigenmodes with the phase speeds $\xi_1 = 0.99$ and $\xi_2 = 0.715$, respectively. The mode responsible for the minimum at 0.32 MHz is a fast mode that could be excited only above its cutoff frequency of about 0.3 MHz.

Its phase velocity is greater than the speed of sound in water, $c = c_t\xi_1 > c_f$. This minimum coincides with the Fabry-Perot maximum, thus producing an asymmetric fine structure in the transmission spectrum.

The second minimum is created by a slow mode, which propagates slower than the pressure wave in water. Both minima caused by the respective eigenmodes are quite sharp due to the suppression of the principal mode that is responsible of transmitting the most energy through the channel.

The results described above were independently verified by simulating the transmission of sound using the finite element method (FEM) [10]. The simulated spectra provided the agreement with both the theory and the experiment and illustrated how the elastic waves initially localized near the channel walls are transformed into the leaky waves as they propagate in the channel. The viscous effects were omitted in the simulations, which confirmed that the observed transmission features are not due to the unaccounted dissipation in water.

## 2.7. Summary

A comprehensive study of sound transmission through a fluid channel surrounded by elastic regions is presented in this chapter. The rigorous analytical solution of the scattering problem allows to calculate the transmission spectrum that almost coincides with the experimental transmission data. It is theoretically discovered that the system exhibits an unusual behavior — the behavior of a redirecting acoustic antenna. The ability of the fluid channel to redirect the acoustic energy at an almost $90^o$ angle into the surrounding elastic media is quite strong, allowing to affect up to approximately 10% of the incoming flux. The phenomenon discussed above was previously unknown for the fluid channels, and it is explained in terms of the mutually interfering coupled Rayleigh eigenmodes of the channel. Simply put, whenever the vibrations of the fluid and the elastic media become synchronized and form one or several quasi-standing waves in the system, the transmission forward and the reflection backward are suppressed and the acoustic flux escapes in the remaining unusual direction.

The analytical approach developed for this problem employs the method of expanding the acoustic fields over the set of eigenmodes of the system. The lack of orthogonality of

the eigenmodes does not allow for the completely analytical solution, nevertheless, the obtained numerical solution is practically exact. This approach can be applied to other problems with more complicated geometries, such as elastic screens with periodically arranged apertures.

The effect of the redirection of sound is important for designing of the acoustic devices that are able to manipulate the propagation of sound, such as acoustic waveguides or acoustic antennas.

CHAPTER 3

REDIRECTION OF SOUND BY A PERIODIC CHAIN OF PERFORATED METALLIC
CYLINDRICAL SHELLS

3.1. Introduction

This chapter provides insights into the phenomena of sound manipulation that are
achievable with the periodic chain of highly symmetric scatterers.

It is known that in the case of electromagnetic waves, such chains composed of cylin-
ders or spheres may serve as waveguides [74, 12, 63]. They can also efficiently transverse
electromagnetic energy provided the scatterers are close enough so that they couple via
the plasmonic near-field. However, in such structures, especially in linear chains, the dissipa-
tion of energy may be quite large as there are not only the Joule losses, but also the radiative
[105, 98, 66, 18, 8] and collisionless nonradiative [11] losses (Landau damping).

In acoustics, one cannot achieve very strong coupling between two neighboring scat-
terers as it would require the existence of some analog of the gap plasmon resonance. Still,
the fact that it is much easier to manipulate the density, elasticity, and viscosity of the me-
dia than their dielectric permittivity, allows predicting and observing transport properties
specific for acoustic waves.

3.1.1. Phenomena in Periodic Arrangements of Scatterers

Earlier studies of the periodic chains where the scatterers had internal structure (ba-
sically, mass-in-mass units) demonstrated that such scatterers exhibit negative mass density
and the mechanical energy can be guided along the chain [42]. In the case of elastic mass-
in-mass units having lateral resonances, the chain was predicted to exhibit the metamaterial
behavior, with both the effective mass and the elastic modulus being negative [43]. Also,
the negative effective index of refraction for sound waves can be achieved, as was shown in
[48] for the structure containing two acoustic Helmholtz resonators (soda cans) per unit cell
of the chain. This becomes possible if the dispersion of the chain is engineered to have its
passing band within a hybridization gap. Other examples [40, 20] demonstrate as well that

once the acoustic interactions between scatterers is sufficiently strong, the system amasses a variety of metamaterial properties.

Now, the scatterers do not necessarily have to be built to feature strong coupling. In fact, periodic structures with artificially *weak* scatterers may be of great interest for researchers, since the interference between the scattered waves from a single unit and the collective wave motion resulting from periodicity allows observation of some very delicate effects [67]. As an example, [97] predicts a Poisson-like effect in the scattering of sound by a periodic composition of cylindrical shells, where the acoustic energy experiences a 90°-redirection of its direction of propagation. Responsible for such effect is the resonant excitation of an antisymmetric mode with polarization perpendicular to the direction of incoming sound. In an elastic solid, a behavior similar to the Poisson effect is exhibited by a cylindrical surface displacing periodically at the resonance, elongating while being squeezed and vice versa. In order to excite the antisymmetric mode, one needs to alter the sound-matter interaction by switching off its strongest monopole and dipole contributions, which can be achieved by matching the density and elastic modulus of the solid shell to those of the background fluid [95, 96]. The interactions are thus occurring via the nonisotropic quadrupole term, which leads to the excitation of the normally deaf antisymmetric collective mode and, ultimately, to the generation of sound waves in the direction perpendicular to the incident wave [97]. It is worth mentioning that the weakness of scattering is not itself responsible for the Poisson-like effect, yet it poses as a necessary condition for its observation.

### 3.1.2. Redirecting Acoustic Antenna from Weak Scatterers

A similar effect of 90°-redirection of sound by a linear chain of perforated metallic cylindrical shells was predicted in [32], however, the physical reason behind it is quite different. Any perforated shell behaves as a weak scatterer when the thickness of the viscous layer in the surrounding fluid is much smaller than the size of perforations. This makes the considered chain practically transparent for the normally incident sound as the weakly scattering shells have no internal resonances (at least, in the kHz frequency range) [32]. Nevertheless, for the frequencies associated with the Wood's anomaly, i.e., when the wavelength

of sound closely matches the period of the chain, the transmission becomes anomalously low. In this chapter, I will examine the microscopic mechanism behind such low transmission and show that the primary cause of the effect is the resonant interaction of the incoming sound with the symmetric leaky eigenmodes of the chain. Specifically, I will consider scattering of incoming plane waves by a linear chain of perforated cylindrical shells (with the parameters similar to those in [32]) with either finite or infinite number of scatterers in both ideal and viscous fluids.

### 3.1.3. Properties of the Redirecting Antenna

There are, however, several properties of the system that can be deduced immediately. First of all, the dispersion equation, which is yet to be derived for the eigenmodes of the chain, will undoubtedly produce the band structure similar to that in the empty-lattice model, as the scattering on every unit is weak. The dispersion will then be practically linear, and the eigenmodes will propagate with the speed equal to the speed of sound in the background fluid, except for the vicinity of the points of degeneracy (the $\Gamma$-point and the edges of the Brillouin zone) where the level repulsion yields a doublet of levels. The two eigenfunctions describing to the components of the doublet are symmetric and antisymmetric functions of coordinates, respectively. It is known that only the symmetric mode can be excited at normal incidence, while the antisymmetric one becomes a deaf mode [82, 104]. When the frequency of the external wave matches the eigenfrequency of the symmetric mode, the transmission of sound is strongly suppressed as the eigenmode is resonantly excited.

In general, only when the spectrum of eigenfrequencies is complex, the external plane wave can excite the eigenmodes. Such modes with complex eigenfrequencies are the so-called leaky modes which carry the acoustic energy away into the background fluid. If the imaginary part of the frequency is small, the acoustic energy is mainly transmitted along the chain, meaning that the the part of the initial energy flux is redirected by 90°. The effects of redirection of sound were studied for periodic systems of scatterers [32, 97, 100], and similar effect exists for a narrow fluid channel between two solid elastic plates, as was discussed in the previous chapter.

One can also resonantly excite both symmetric and antisymmetric modes by an obliquely incident wave. No matter how small the angle of incidence, the nonzero component of the wave vector along the chain ensures that the incoming front does not have any symmetry and thus there is no restriction as to which mode can be excited and which cannot. In addition, addressing the properties of the dispersion law for the eigenmodes is crucial. Namely, the dispersion of each level in the empty-lattice model alternates between normal and anomalous, the property which is preserved in the 1D system with weak periodic scattering potential. Near the $\Gamma$-point, the upper (high-frequency) level of the doublet exhibits normal dispersion, whereas the dispersion of the lower (low-frequency) level is anomalous. The phase and group velocities in the case of normal dispersion are parallel, and in the case of anomalous dispersion — anti-parallel. This dictates an essentially different behavior for the scattered waves for the two frequencies of the doublet.

Since the excitation of the eigenmode in the chain occurs when its Bloch vector $\mathbf{q}$ matches the parallel component $\mathbf{k}_{||}$ of the wave vector in the incoming wave, and since the group velocity indicates the direction of propagation of acoustic energy, the eigenmode with normal dispersion will carry energy in the direction of $\mathbf{k}_{||}$ along the chain. The mode with anomalous dispersion, on the contrary, redirects energy to run against $\mathbf{k}_{||}$ along the chain. For the small angle of incidence, the two levels of the doublet are close to each other, thus enabling the chain of perforated shells to serve as a splitting antenna. An incoming signal consisting of two harmonics matching the doublet frequencies will have its higher- and lower-frequency components redirected by such antenna by almost 90° with respect to their original direction and in the opposite directions to each other. The anticipated phenomena are robust with respect to the viscosity of the fluid, with the only differences being quantitative, not qualitative, provided the viscosity is not too large.

3.2. Single Scatterer Characterization

Each cylindrical shell is produced by rolling a perforated metal plate into a cylindrical shape (see Fig. 3.1). In this chapter, I will be using the same material and geometry

FIGURE 3.1. The perforated metallic cylindrical shell fabricated and used in the experiments in [32, 33, 81].

parameters that were adopted for the experimental and numerical studies in [32, 81], namely:

- outer radius of the shell                     $a = 4.00$ cm,
- inner radius of the shell                      $b = 3.95$ cm,
- thickness of the shell $(h = a - b)$    $h = 0.05$ cm,
- radius of the circular perforation    $r = 0.25$ mm,
- filling fraction of the perforations    $\sigma = 0.145$.

53

The metal from which the shells were made of was aluminum, and the parameters of the air environment are as follows:

- density of air $\rho_0 = 1.25$ kg/m$^3$,
- speed of sound in air $c_0 = 343$ m/s,
- viscosity of air (dynamic) $\eta_0 = 17.8\,\mu$Pa $\cdot$ s.

The interaction of the perforated shell with the sound, specifically, the boundary conditions at the metal-air interfaces, will be described by the effective impedance $Z_p$ of the shell.

### 3.3. Impedance of the Perforated Scatterer

The notion of effective impedance was introduced in the works [61, 60] for flat thin perforated plates, and it differs essentially from the notion of the acoustic impedance of the medium $Z = \rho c$. For a plate of thickness $h$ coinciding with the $xOy$ plane, the effective impedance was defined as

$$(3.1) \qquad Z_p = \frac{p|_{z=-\frac{h}{2}} - p|_{z=+\frac{h}{2}}}{\bar{v}_z},$$

where the pressures in the numerator are evaluated on either side of the plate, and the denominator expresses the $z$-component of the average velocity of the fluid inside the perforation.

This idea of the effective impedance comes with additional assumptions. First of all, it relies on the high contrast between the material of the plate and the environment. This condition is satisfied when experimenting with metal plates in air, and therefore one may assume the metal regions to be ideally rigid. Then, the transmission of sound through the perforated plate occurs mostly through the perforations. The plate is assumed to be perforated uniformly with a quite high perforation constant, so that a single boundary condition would apply for the entire plate regardless of where the openings are actually located. This boundary condition takes the form of

$$(3.2) \qquad v_z|_{z=-\frac{h}{2}} = v_z|_{z=+\frac{h}{2}} = \frac{p|_{z=-\frac{h}{2}} - p|_{z=+\frac{h}{2}}}{Z_p},$$

where due to the small thickness of the plate the velocities on either side of the plate are approximately equal. Also, the wavelength of sound that penetrates through the plate must be much larger than the perforation size.

The expression for $Z_p$ through the material parameters and the perforation geometry is typically represented as a sum of internal and external terms which capture different physical aspects of the sound propagation.

### 3.3.1. Internal Contribution of a Single Perforation

The internal term is the most important for the total effective impedance since it describes the propagation of sound through the perforation. The derivation of this term outlined in [61] is based on the studies of wave propagation inside infinitely long tubes [78].

The motion of the fluid inside the perforation can be described by the linearized Navier-Stokes equation

$$(3.3) \qquad -\nabla p + \eta_0 \Delta \mathbf{v} \;=\; \rho_0 \frac{\partial \mathbf{v}}{\partial t}$$

which accounts for the friction losses due to the dynamic viscosity of the fluid. The equation of motion along $z$ (in the axial direction) is conveniently expressed in cylindrical coordinates $(r', \varphi, z)$ as

$$(3.4) \qquad -\nabla_z p + \frac{\eta_0}{r'} \frac{\partial}{\partial r'} \left( r' \frac{\partial v_z}{\partial r'} \right) \;=\; \rho_0 \frac{\partial v_z}{\partial t}.$$

For a monochromatic vibration (with time dependence $e^{-i\omega t}$) inside the circular tube of radius $r$, the latter equation becomes

$$(3.5) \qquad \left( \frac{\partial^2}{\partial r'^2} + \frac{1}{r'} \frac{\partial}{\partial r'} + i \frac{s^2}{r^2} \right) v_z \;=\; \frac{1}{\eta_0} \frac{\partial p}{\partial z},$$

where $s = r/\delta = r\sqrt{\omega \rho_0/\eta_0}$ has the meaning of the perforate constant of the metal plate. The parameter $s$ relates the radius of the perforation to the characteristic thickness of the viscous boundary layer $\delta = \sqrt{\eta_0/\omega\rho_0}$. For the large values of $s$ ($s \gg 1$) the viscous dissipation occurs within the negligibly thin layers near the metal surface.

The boundary condition for the viscous flow requires vanishing of the axial velocity at the walls of the tube, $v_z|_{r'=r} = 0$, and this results in the velocity profile

(3.6)
$$v_z = \frac{1}{i\omega\rho_0}\frac{\partial p}{\partial z}\left(1 - \frac{J_0\left(s\sqrt{i}\,\frac{r'}{r}\right)}{J_0\left(s\sqrt{i}\right)}\right).$$

Averaging the velocity over the cross section of the tube gives

(3.7)
$$\bar{v}_z = \frac{2}{r^2}\int_0^r v_z r'dr' = \frac{1}{i\omega\rho_0}\frac{\partial p}{\partial z}\left(1 - \frac{2}{s\sqrt{i}}\frac{J_1\left(s\sqrt{i}\right)}{J_0\left(s\sqrt{i}\right)}\right),$$

and since for a thin perforated plate one can replace the pressure gradient with the ratio of the pressure difference to the plate thickness, the internal term of the effective impedance (3.1) becomes equal

(3.8)
$$Z_1^{(int)} = -i\omega\rho_0 h\left(1 - \frac{2}{s\sqrt{i}}\frac{J_1\left(s\sqrt{i}\right)}{J_0\left(s\sqrt{i}\right)}\right)^{-1}.$$

3.3.2. External Contribution of a Single Perforation

I write the external term of the effective impedance as

(3.9)
$$Z_1^{(ext)} = 4\sqrt{2\eta_0\omega\rho_0} - i\omega\rho_0\frac{16r}{3\pi}\left(1 - 2.5\sqrt{\frac{\sigma}{\pi}}\right).$$

The first contribution is a viscous end correction [39] which is due to the dissipation of acoustic energy near (not inside) the opening. The second term appears as a result of the air motion outside the hole. Qualitatively, the latter effect is accounted for by increasing the effective depth of the perforation and is viewed as an extra mass attachment to the edges of the hole [19, 44].

Other possible additions to the impedance may be due to the nonlinear or the grazing flow effects, which are disregarded in this chapter.

3.3.3. Total Impedance

Now, the impedance $Z_1 = Z_1^{(int)} + Z_1^{(ext)}$ of a single perforation needs to be related to the impedance of the whole plate. In order to do that, I separately consider the points on

both surfaces of the plate that correspond to either the hole or the metal, and write down how the velocities of the acoustic vibrations in air at these points are related.

Namely, I conclude that

(3.10)
$$v_z|_{z=\pm\frac{h}{2}} = \begin{cases} 0, & \text{(for metal)}, \\ \dfrac{p|_{z=-\frac{h}{2}} - p|_{z=+\frac{h}{2}}}{Z_1}, & \text{(for holes)}. \end{cases}$$

The first relation is dictated by the rigid-body approximation, and for the rest of the points I make use of the introduced impedance $Z_1$.

In the case of large wavelengths of sound, $\lambda \gg r/\sqrt{\sigma}$, it is possible to average (3.10) over the element of the plate surface which has its linear size much smaller than $\lambda$ but nevertheless contains a large number of perforations.

The averaging results in the uniform boundary condition

(3.11)
$$v_z|_{z=\pm\frac{h}{2}} = \frac{p|_{z=-\frac{h}{2}} - p|_{z=+\frac{h}{2}}}{Z_p},$$

where the effective impedance of the perforated plate is expressed as

(3.12) $\quad Z_p = \dfrac{Z_1}{\sigma} = -\dfrac{i\omega\rho_0}{\sigma}\left[h\left(1 - \dfrac{2}{s\sqrt{i}}\dfrac{J_1\left(s\sqrt{i}\right)}{J_0\left(s\sqrt{i}\right)}\right)^{-1} + 4i\sqrt{2}\delta + \dfrac{16r}{3\pi}\left(1 - 2.5\sqrt{\dfrac{\sigma}{\pi}}\right)\right].$

In the limit of an ideal fluid, for which the viscosity is negligible, $\eta_0 \to 0$, the perforate constant approaches infinity, $s \to \infty$, and the impedance (3.12) becomes purely imaginary

(3.13)
$$Z_p = -\frac{i\omega\rho_0}{\sigma}\left[h + \frac{16r}{3\pi}\left(1 - 2.5\sqrt{\frac{\sigma}{\pi}}\right)\right].$$

The latter expression for the effective impedance assumes that the perforated plate is perfectly flat, however, it may still be approximately valid after the plate is rolled up to form a cylindrical shell, at least, in the long-wavelength limit. The evidence for this was reported in [33, 101], where the scattering of sound from the perforated shell was measured experimentally and compared with the numerical simulations that employed the effective impedance (3.12). The obtained spectra of the scattered sound agreed well in the frequency range from 0 to 5 kHz.
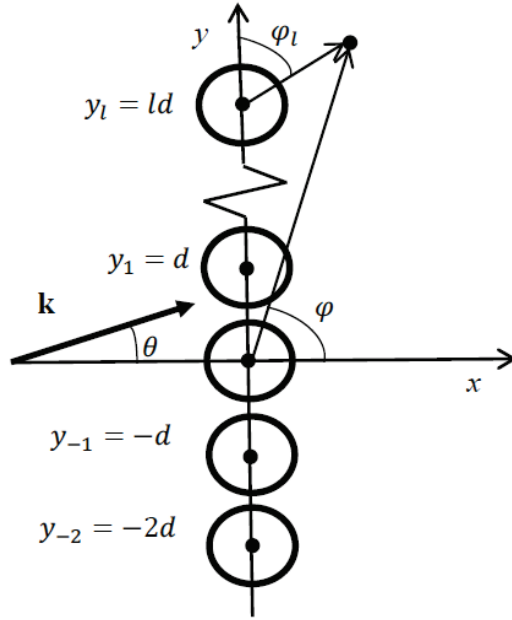
FIGURE 3.2. Top view of the perforated cylindrical shells aligned along the $y$-axis with the period $d$. Polar angles are shown for the central $(l = 0)$ and $l$-th units. The acoustic plane wave is incident at the angle $\theta$ on the chain.

## 3.4. Scattering Problem

### 3.4.1. Geometry

I start with the analysis of the sound interaction with the finite chain of $2N + 1$ scatterers. The scatterers are spread along a straight line, with their axes intersecting the $y$-axis at the points $y_n = nd$, $n = 0, \pm1, \pm2, \ldots, \pm N$ (see Fig. 3.2). The neighboring shells are separated by a distance $d = 11.0$ cm, which serves as the period of the chain. The incoming sound is modeled by a monochromatic plane wave which approaches from the left at an angle $\theta$. Namely, the pressure of the incident wave is $p(\mathbf{r}, t) = p_0 \exp(i\mathbf{k} \cdot \mathbf{r} - i\omega t)$, where the wave vector $\mathbf{k}$ has the components of $\mathbf{k} = (k_x, k_y, 0) = (k \cos\theta, k \sin\theta, 0)$.

The solution to the scattering problem will be obtained for both finite and infinite chains of perforated shells. The latter only requires taking the limit of $N \to \infty$, and allows for additional simplifications as the Bloch theorem becomes applicable. Similar problems were

investigated in [80, 110]. The two dealt with the scattering of acoustic waves at a periodic array of solid spheres in fluid and at a monolayer of elastic spheres in air, respectively. Also, such scattering problems are of interest in electrodynamics as well, namely, the work [8] presented an analysis of the reflection of electromagnetic waves from an infinite line of conducting cylinders.

In general, scattering of waves by an infinite periodic array of cylinders constitutes one of the classical problems in the theory of diffraction.

### 3.4.2. Scattered and Transmitted Pressure Fields

Based on the geometry of the problem, it is convenient to develop the solution in the cylindrical coordinate system. Each cylindrical shell will have a separate coordinate system associated with it, and I will use the notion of $(r_l, \varphi_l, z)$ for the coordinates of a point in space with respect to the $l$-th coordinate system. The origin of each system is located at the point $y_l = ld$, i.e., the axis of each cylinder coincides with the $z$-axis of the respective coordinate system, as shown in Fig. 3.2.

The incoming pressure plane wave

$$(3.14) \qquad p(\mathbf{r}, t) = p_0 \exp(i\mathbf{k} \cdot \mathbf{r} - i\omega t)$$

is represented in each of those coordinate systems by the series

$$(3.15) \qquad p(\mathbf{r}, t) = p(r_l, \varphi_l, t) = p_0 e^{ikr_l \cos(\varphi_l - \theta) - i\omega t} = p_0 \sum_{n=-\infty}^{\infty} i^n J_n(kr_l) e^{in(\varphi_l - \theta) - i\omega t}.$$

where the wave vector $k$ is $k = \omega/c_0$. The harmonic time dependence $e^{-i\omega t}$ will be omitted further below.

The pressure field obeys the wave equation (2.8), which in the cylindrical coordinates is expressed as

$$(3.16) \qquad \frac{1}{r}\frac{\partial}{\partial r}\left(r\frac{\partial p}{\partial r}\right) + \frac{1}{r^2}\frac{\partial p}{\partial \varphi^2} + k^2 p(r, \varphi) = 0.$$

The derivative with respect to $z$ does not appear above as the problem is assumed to be uniform along $z$. If the angular dependence is eliminated by assuming the proportional to

$e^{in\varphi}$, $n = 0, \pm1, \pm2, ...$, behavior of pressure, then the solutions of the radial part of the wave equation (3.16) are the Bessel functions of the order $n$.

This knowledge allows to write down the acoustic field scattered by an array of shells as a superposition of cylindrical waves:

$$(3.17) \qquad p_{sc}(r, \varphi) = \sum_{l'} \sum_{n=-\infty}^{+\infty} B_{l'n} H_n^{(1)}(kr_{l'}) e^{in\varphi_{l'}}, \qquad r_l' \geq a.$$

The inner sum over $n$ represents the total field radiated by each $l'$-th shell with respect to the coordinate system aligned with that shell. The outer sum over $l'$ adds those contributions together to produce the total scattered field. The value of $l'$ runs from $-N$ to $N$ for a finite chain, or from $-\infty$ to $+\infty$ for an infinite chain. The Hankel functions of the first kind $H_n^{(1)}(kr)$ (or simply $H_n(kr)$) are chosen for the expansion (3.17) as they describe the outgoing waves due to their asymptotic behavior $H_n^{(1)}(kr) \sim e^{ikr}/\sqrt{kr}$ at infinity.

The use of multiple coordinate systems within the same equation (3.17) is perplexing and undesirable, and it is best to rewrite the expression of the scattered pressure field in terms of only the coordinates $(r_l, \varphi_l)$ of the certain $l$-th system. Fortunately, since one has a trivial relation between the Cartesian coordinates $\mathbf{r} = (x, y)$ and the polar coordinates $(r_l, \varphi_l)$ in the form of

$$(3.18) \qquad x = r_l \cos \varphi_l,$$

$$(3.19) \qquad y = ld + r_l \sin \varphi_l,$$

then the transformation between $(r_l, \varphi_l)$ and $(r_{l'}, \varphi_{l'})$ is as follows:

$$(3.20) \qquad r_{l'} \cos \varphi_{l'} = r_l \cos \varphi_l,$$

$$(3.21) \qquad r_{l'} \sin \varphi_{l'} = (l - l')d + r_l \sin \varphi_l,$$

For the polar coordinates related by (3.20)-(3.21), the Graf's addition theorem (see Appendix C) applies:

$$(3.22) \qquad H_n(kr_{l'}) e^{in\varphi_{l'}} = \sum_{n'=-\infty}^{\infty} i^{(n+n')\mathrm{sign}(l-l')} H_{n+n'}(k|l-l'|d) J_{n'}(kr_l) e^{in'(\pi-\varphi_l)},$$

60

given that the conditions $l' \neq l$ and $r_l < |l - l'|d$ are met.

As a result, one arrives at the expression for the scattered field (3.17) that involves only one pair of coordinates $(r_l, \varphi_l)$ and is valid for $r_l < d$, i.e., only in the vicinity of the $l$-th perforated shell:

$$(3.23) \quad p_{sc}(r_l, \varphi_l) = \sum_{n=-\infty}^{+\infty} \left[ B_{ln} H_n(kr_l) e^{in\varphi_l} + \right.$$

$$\left. + \sum_{l' \neq l} B_{l'n} \sum_{n'=-\infty}^{+\infty} i^{(n+n')\operatorname{sign}(l-l')} H_{n+n'}(k|l-l'|d) J_{n'}(kr_l) e^{in'(\pi-\varphi_l)} \right].$$

The obtained expansion will prove extremely useful for the purpose of dealing with the boundary conditions at the surfaces of the shells.

As for the pressure fields inside each $l$-th cylinder, I write their expansions over the Bessel functions

$$(3.24) \qquad\qquad p_{in}^{(l)}(r_l, \varphi_l) = \sum_{n=-\infty}^{\infty} C_{ln} J_n(kr_l) e^{in\varphi_l}, \qquad r_l \leq b.$$

All other cylinder functions are still valid solutions of the wave equation (3.16), but they cannot enter the series (3.24) as they diverge when $r_l \to 0$ and therefore do not describe any physically reasonable field behavior.

### 3.4.3. Boundary Conditions at the Surfaces of the Shells

As was discussed earlier, the acoustic fields on either side of the perforations are related in a simplified fashion which, nevertheless, does not undermine the resulting accuracy of calculations. Namely, even though each perforated shell has a finite thickness $h$, its value is much smaller than either of the radii $a$ and $b$, and thus one can view the two cylindrical faces of each shell as a virtually single interface. The fluid-metal interactions are already encompassed inside the effective impedance (3.12), and one only needs to relate the pressure fields outside the shells with those inside the shells.

The condition (3.2) prescribes to assume the radial component of the velocity of the fluid (that is, normal to the interface) to be unchanged across the thickness of the metal,

and also relates it to the pressure discontinuity between the faces of the shells:

$$(3.25) \qquad v_r|_{r=a} = v_r|_{r=b} = \frac{p|_{r=b} - p|_{r=a}}{Z_p}$$

The radial velocity in fluid is derived from the local pressure according to (2.10):

$$(3.26) \qquad v_r = \frac{1}{i\omega\rho_0} \frac{\partial p}{\partial r}.$$

From the three equations that appear in (3.25), I will be using the following two independent relations:

$$(3.27) \qquad v_r|_{r=a} = v_r|_{r=b},$$

$$(3.28) \qquad p|_{r=a} = p|_{r=b} - Z_p v_r|_{r=b},$$

where the place of the pressure outside the shell $p|_{r=a}$ will be taken by the superposition of the incoming and scattered waves $p + p_{sc}$, and the pressure inside the shell $p|_{r=b}$ is exactly the pressure field $p_{in}^{(l)}$.

The method of expressing the acoustic fields in terms of series over cylinder functions and matching them via the boundary conditions is exact since its solution is the total *true* field. As opposed to this, the approach based on the $T$-matrix method and the multiple scattering theory used in [33, 32] is only approximate as it discards the high-order scatterings of the waves.

The dissipation of energy due to the viscous effects in air is accounted for via the effective impedance $Z_p$ of the perforated shells. The viscous friction at the air-metal interfaces is practically the only reason for the energy loss. The dissipation within the bulk volume of air is almost nonexistent at the frequencies of several kHz, the typical decay length being on the order of several kilometers.

Note that since the elastic vibrations of the metal are not considered explicitly in this approach, there is neither need nor advantage in using the notion of acoustic potentials (2.12), (2.20) and (2.21) in solving this problem.

## 3.5. Solution for the Scattered Acoustic Field

### 3.5.1. Finite Chain of Perforated Shells

The equations (3.15), (3.23), and (3.24) express the pressure fields basically in the form of Fourier expansions over $e^{in\varphi_l}$. Because of that, the angular dependence in the boundary conditions (3.26) can be eliminated by applying the Fourier transform, splitting each condition into a set of equations for the respective Fourier coefficients. This results in the following set of linear equations for the unknowns $B_{ln}$ and $C_{ln}$:

(3.29)

$$
\begin{cases}
C_{ln}\dfrac{J_n'(kb)}{J_n'(ka)} = p_0 i^n e^{-in\theta} \ +B_{ln}\dfrac{H_n'(ka)}{J_n'(ka)}+ \\
\qquad\qquad\qquad +\displaystyle\sum_{l'\neq l}\sum_{n'=-\infty}^{\infty} i^{(n-n')\mathrm{sign}(l-l')} H_{n-n'}(k|l-l'|)d)B_{l'n'}, \\[2em]
\dfrac{ikZ_p}{\omega\rho_0}C_{ln}\dfrac{J_n'(kb)}{J_n(ka)} + C_{ln}\dfrac{J_n(kb)}{J_n(ka)} = p_0 i^n e^{-in\theta} \ +B_{ln}\dfrac{H_n(ka)}{J_n(ka)}+ \\
\qquad\qquad\qquad +\displaystyle\sum_{l'\neq l}\sum_{n'=-\infty}^{\infty} i^{(n-n')\mathrm{sign}(l-l')} H_{n-n'}(k|l-l'|)d)B_{l'n'}.
\end{cases}
$$

The index $n$ indicates which specific Fourier component the equations are written for, and the index $l$ enumerates the shells, meaning that the equations containing $C_{ln}$ resulted from applying the boundary conditions to the $l$-th shell.

The scattered acoustic field depends only on the unknown $B_{ln}$, so one may substitute the value of $C_{ln}$ obtained from the first row of (3.29) into the second row, and obtain the system of linear inhomogeneous equations for $B_{ln}$ only:

(3.30)
$$
S_n B_{ln} + \sum_{l'\neq l}\sum_{n'=-\infty}^{\infty} i^{(n-n')\mathrm{sign}(l-l')} H_{n-n'}\left(k|l-l'|d\right)B_{l'n'} = -p_0 i^n e^{-in\theta},
$$

where $S_n$ denotes the fraction

(3.31)
$$
S_n = \frac{H_n(ka) - H_n'(ka)\left(\dfrac{iZ_p}{\rho_0 c_0} + \dfrac{J_n(kb)}{J_n'(kb)}\right)}{J_n(ka) - J_n'(ka)\left(\dfrac{iZ_p}{\rho_0 c_0} + \dfrac{J_n(kb)}{J_n'(kb)}\right)}.
$$

The last step in calculating the distribution of the scattered field (3.17) from a finite chain of perforated shells is solving the linear set (3.30), which will be done numerically.

### 3.5.2. Infinite Chain of Perforated Shells

For an infinite periodic chain of scatterers ($N = \infty$), the obtained system (3.30) still remains valid. Moreover, it can be now further simplified since it is imperative to benefit from the established periodicity of the system along the $y$-axis. The Bloch theorem guarantees that in a periodic environment a propagating wave $\psi(x, y)$ is represented as $\psi(x, y) = e^{iqy}v(x, y)$, where the function $v(x, y)$ is periodic, $v(x, y) = v(x, y + d)$, and $q$ is the $y$-component of the wavevector of the wave.

The incident at the chain plane wave determines the wavevector $q$:

$$(3.32) \qquad q \;=\; k_y \;=\; k\sin\theta,$$

and to satisfy the inferences of the Bloch theorem, the unknown amplitudes $B_{ln}$ must be related to the values $B_{0n}$ associated with the shell in the middle of the chain:

$$(3.33) \qquad B_{ln} = e^{ik_y ld} B_{0n}.$$

I substitute the latter relation into (3.30), redefine the unknowns as $b_n = i^{-n} B_{0n}$, and arrive at the following set of linear equations:

$$(3.34) \qquad \mathcal{S}_n b_n + \sum_{n'=-\infty}^{\infty} F(n'-n) b'_n = -p_0 e^{-in\theta}, \;\; n = 0, \pm 1, \pm 2, \ldots$$

Here the lattice sum $F(n)$ is an infinite series

$$(3.35) \qquad F(n) = \sum_{l'=1}^{+\infty} H_n\left(kl'd\right) \left[ e^{ik_y l'd} + (-1)^n e^{-ik_y l'd} \right],$$

the calculation of which is discussed in Appendix D.

A similar set of equations was obtained in [8, 25] for scattering of waves at an infinite periodic chain of metallic cylinders.
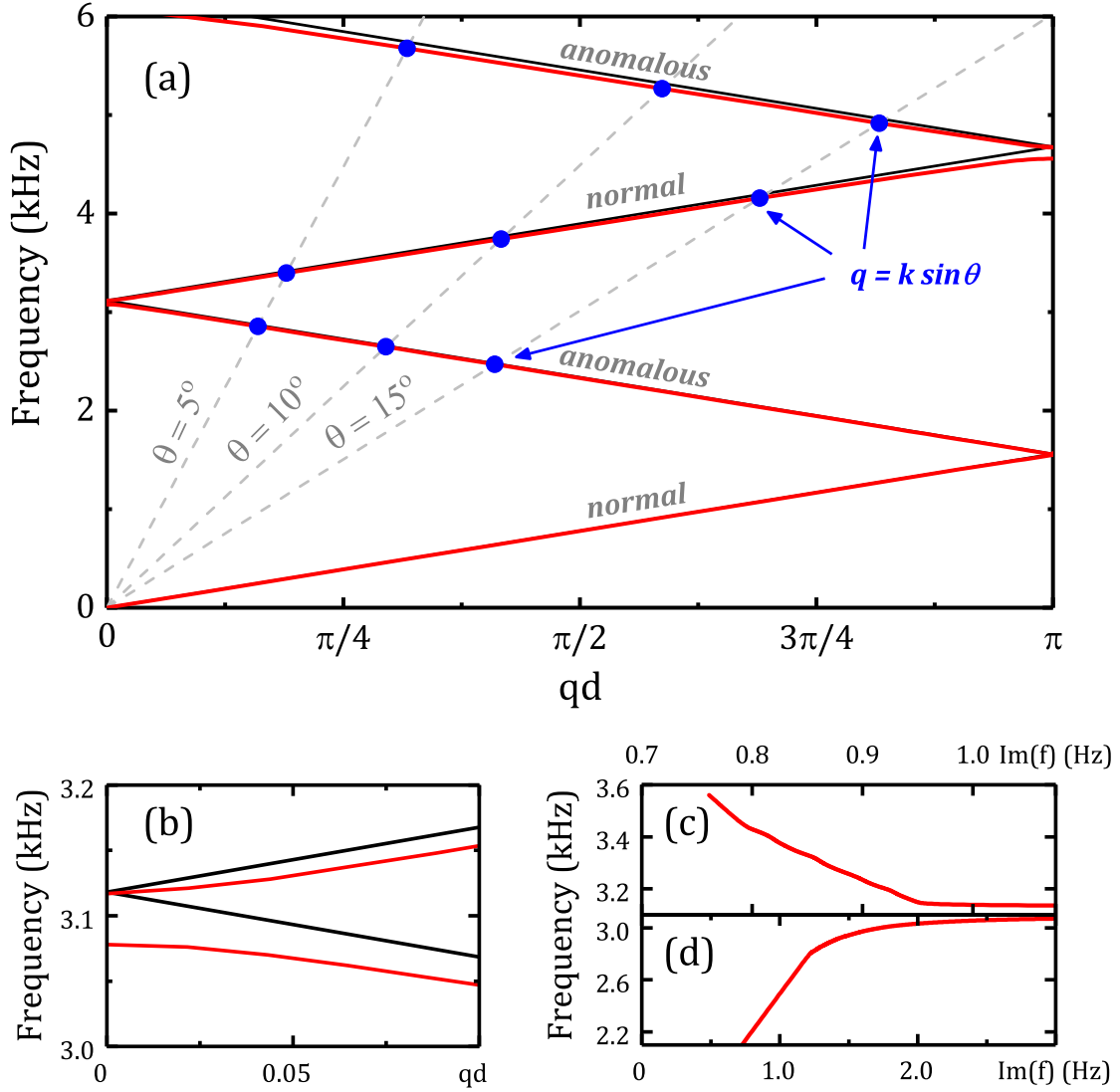
FIGURE 3.3. (a) Band structure of an infinite periodic chain of shells in in-viscid air environment. Straight black lines show linear dispersion in air. Red lines are the real parts of eigenfrequencies calculated from (3.36). Crossings of the dispersion curves with three dashed straight lines (3.54) give the frequencies of resonant coupling of the incident plane wave to the eigenmodes of the chain for three angles of incidence, $\theta = 5°$, $\theta = 10°$, and $\theta = 15°$. (b) Band splitting at the $\Gamma$-point near the frequency $f = 3.1$ kHz; the distance between the levels in the doublet is 35 Hz. (c),(d) Absolute value of the imaginary part of eigenfrequency vs its real part for the region near 3.1 kHz.

## 3.6. Eigenmodes of an Infinite Chain of Scatterers

### 3.6.1. Dispersion Relation

Here I analyze the eigenmodes that can be supported by the infinite chain of perforated shells in order to gain additional insights about its capability to suppress sound transmission. The eigenmodes are the waves propagating in either direction along the chain and are characterized by the wavevector $q$. They are the nontrivial solutions of (3.34), in which the right-hand side contains no incident wave. By equating the determinant of a corresponding homogeneous linear system to zero,

$$(3.36) \qquad \det |\mathcal{S}_n \delta_{nn'} + F(n' - n)| = 0,$$

one obtains the equation that defines the dispersion relation $\omega = \omega(q)$ of the eigenmodes.

Finding the solution to (3.36) is complicated by the necessity to calculate the determinant of an infinite matrix and by having to deal with the slow-converging series (3.35). The latter issue is addressed by identically replacing $F(n)$ with the fast-converging series originally found in [99] and subsequently used in [8, 25] (see Appendix D).

Fig. 3.3(a) visualizes the few lowest bands of the dispersion equation, which are calculated numerically. Due to perforated shells being weak scatterers, the resulting dispersion curve (shown in red) is almost identical to the band structure describing the empty-lattice model (shown in black). The differences between the two appear only near the $\Gamma$-point $q = 0$ (and also at the zone edge $q = \pi/d$), where the level doublet is formed due to the level repulsion, forming a gap. The gap size is approximately 35 Hz between the second and the third bands (which is near the frequency of 3.1 kHz). The first (lowest) band and other odd-numbered bands have normal dispersion, whereas every even-numbered band exhibits anomalous dispersion. As can be seen in Fig. 3.3(b), the dispersion of the bands becomes essentially nonlinear towards the $\Gamma$-point.

It is also peculiar that the two bands of the doublet exhibit different behavior: only for the lower band does the group velocity vanish when $q = 0$, thus making the gap opening strongly asymmetric. Moreover, the upper band exhibits a singularity which is not resolved

66

in Fig. 3.3. The behavior of both bands will be analyzed in more detail further in this chapter.

The solutions $\omega(q) = 2\pi f(q)$ of the transcendental dispersion equation (3.34), found for real values of the wave vector $q$, are complex. This makes the acoustic eigenmodes of an infinite chain leaky, regardless of whether the viscosity of the fluid is accounted for. Leaky eigenmodes are not strongly localized in the vicinity of the chain, instead they carry the acoustic energy away from it, and the imaginary part of the frequency describes the strength of radiative decay.

Nevertheless, the leaky modes may still be long-living excitations if the decay is very slow, i.e., if the imaginary part $\text{Im } f$ is small. As is shown in Fig. 3.3(c,d), the rate of radiative decay $|\text{Im } f|$ is smaller than the frequency of sound $f \approx \text{Re } f$ by at least two orders of magnitude. Namely, near the $\Gamma$-point this rate is about 1-3 Hz, which practically does not affect the width of the resonance minima in the transmission spectra, as will be discussed below. The use of the absolute value to characterize the decay rate $|\text{Im } f|$ indicates that the imaginary part of frequency is negative, $\text{Im } f < 0$, which is imperative in order to have the time-dependent term $e^{-i\omega t}$ exponentially decreasing and not increasing with time.

3.6.2. Analysis of the Asymmetric Band Gap

Here I will analyze the behavior of the two bands forming a doublet near the $\Gamma$-point (see Fig. 3.3(c)). This can be done using an approach that treats the perforated shells as a small perturbation to the uniform air background. In zero approximation, i.e., in the empty-lattice model, the dispersion bands are linear. When the small perturbations are introduced, the differences between the linear bands and the actual dispersion curves found by solving (3.36) are small, and are only significant in the vicinity of the $\Gamma$-point and the edges of the Brillouin zone, i.e., only near the points of degeneracy. In the theory of band structures, the perturbation theory for degenerate states is typically used to calculate such band corrections. However, the degeneracy is removed from the picture by the presence of weak scattering, and the narrow band gaps are formed. In solids, applying such perturbation theory results in the so-called nearly free electron model, where the unperturbed eigenfunc-

tions are represented by a basis of simple plane waves. In the case of a chain of perforated shells, the basis of cylindrical functions needs to be used, and thus the perturbation theory that will apply here will strongly differ from that in the nearly free electron model. Even though the final result — forming of narrow band gaps — is expected to be qualitatively the same, I will still obtain the explicit expressions for the level repulsion near the points of degeneracy and compare obtained formulas with the values found by solving the exact dispersion equation (3.36) numerically. I will show that the strength of the level repulsion is essentially different from what is known in the nearly free electron model. The reason behind this is the specific form of the boundary condition (3.25), which approximates the interaction of the shell with the background using the impedance approach and assumes a discontinuity of pressure on the two surfaces of the shell even for very thin shells.

The absence of the perforated shells, which implies no scattering of sound, can be obtained by decreasing the acoustic impedance to zero, $Z_p \to 0$. This fact makes it different from the situation where the absence of scattering from a solid cylinder is normally realized by matching the impedances $\rho c$ of the background fluid and the cylinder. The parameter $Z_p$ will serve as a small perturbation in the perturbation theory. The smallness of $Z_p$ also requires the shells to be extremely thin, $h = (a - b) \to 0$, however, the thickness cannot be used as a small parameter as the latter condition only is not sufficient itself (see (3.12) and (3.13)).

The coefficient $\mathcal{S}_n$ in (3.31) approaches infinity when $a \to b$ and $Z_p \to 0$, which allows rewriting the dispersion relation (3.36) in the following form:

$$(3.37) \qquad \det \left| \delta_{nn'} + \frac{F(n' - n)}{\mathcal{S}_n} \right| = 0.$$

Since $F(n' - n)/\mathcal{S}_n \ll 1$, the matrix in (3.37) is almost diagonal and its determinant can be approximated by

$$(3.38) \qquad \det \left| \delta_{nn'} + \frac{F(n' - n)}{\mathcal{S}_n} \right| \approx \det |\delta_{nn'}| + \mathrm{Tr} \left( \frac{F(n' - n)}{\mathcal{S}_n} \right) = 1 + F(0) \sum_{n=-\infty}^{+\infty} \mathcal{S}_n^{-1}.$$

I further expand the terms $\mathcal{S}_n^{-1}$ in the series (3.38) over the small parameters $h = a - b$ and

$Z_p$. In the linear approximation one arrives at the expression

$$(3.39) \quad \mathcal{S}_n^{-1} = \frac{J_n\left(ka\right) - J_n'\left(ka\right)\left(\dfrac{iZ_p}{\rho_0 c_0} + \dfrac{J_n\left(kb\right)}{J_n'\left(kb\right)}\right)}{H_n\left(ka\right) - H_n'\left(ka\right)\left(\dfrac{iZ_p}{\rho_0 c_0} + \dfrac{J_n\left(kb\right)}{J_n'\left(kb\right)}\right)} =$$

$$= \frac{-\dfrac{iZ_p}{\rho_0 c_0} J_n'\left(ka\right) J_n'\left(kb\right) + \left(J_n\left(ka\right) J_n'\left(kb\right) - J_n'\left(ka\right) J_n\left(kb\right)\right)}{-\dfrac{iZ_p}{\rho_0 c_0} J_n'\left(ka\right) J_n'\left(kb\right) + \left(H_n\left(ka\right) J_n'\left(kb\right) - H_n'\left(ka\right) J_n\left(kb\right)\right)} \approx$$

$$\approx \frac{-\dfrac{iZ_p}{\rho_0 c_0} J_n'^2\left(ka\right) + k(b-a)\left(J_n\left(ka\right) J_n''\left(ka\right) - J_n'\left(ka\right) J_n'\left(ka\right)\right)}{H_n\left(ka\right) J_n'\left(ka\right) - H_n'\left(ka\right) J_n\left(ka\right)} =$$

$$= \frac{-\dfrac{iZ_p}{\rho_0 c_0} J_n'^2\left(ka\right) + k(a-b)\left(J_n'^2\left(ka\right) - J_n\left(ka\right) J_n''\left(ka\right)\right)}{-\dfrac{2i}{\pi ka}} \approx$$

$$\approx \frac{\pi ka}{2i} \frac{iZ_p}{\rho_0 c_0} J_n'^2\left(ka\right) - \frac{1}{2i}\pi k^2 a(a-b)\left(J_n'^2\left(ka\right) - J_n\left(ka\right) J_n''\left(ka\right)\right).$$

As is seen from (3.39), the expansion goes over two dimensionless parameters, $z = \dfrac{\pi ka}{2} \dfrac{iZ_p}{\rho_0 c_0}$ and $\epsilon = \pi k^2 ah$. Here $k = \omega/c_0$, so these parameters are real if the background fluid is inviscid. Since the impedance $Z_p \propto \omega$ (see (3.12)), it follows that $z, \epsilon \propto \omega^2$ as well. Such quadratic growth invalidates the approximation (3.39) at high frequencies.

After the expansion (3.39) is substituted into the sum over $n$ in (3.38), one obtains the following result:

$$\sum_{n=-\infty}^{+\infty} \mathcal{S}_n^{-1} = \frac{\pi ka}{2i} \frac{iZ_p}{\rho_0 c_0} \sum_{n=-\infty}^{+\infty} J_n'^2\left(ka\right) - \frac{1}{2i}\pi k^2 ah \sum_{n=-\infty}^{+\infty} \left(J_n'^2\left(ka\right) - J_n\left(ka\right) J_n''\left(ka\right)\right) =$$

$$(3.40) \qquad = \frac{\pi ka}{4i} \frac{iZ_p}{\rho_0 c_0} - \frac{1}{2i}\pi k^2 ah = \frac{z - \epsilon}{2i}.$$

The identities $\displaystyle\sum_{n=-\infty}^{+\infty} J_n'^2(x) = -\sum_{n=-\infty}^{+\infty} J_n(x) J_n''(x) = \frac{1}{2}$ were employed here to simplify the latter expression. I finally rewrite (3.37) and (3.38) as

$$(3.41) \qquad\qquad \frac{1}{F(0)} = -\sum_{n=-\infty}^{+\infty} \mathcal{S}_n^{-1} = -\frac{z - \epsilon}{2i}.$$

In zero approximation, the right-hand side of (3.41) vanishes, and the dispersion is thus obtained from the condition $F(0) = \infty$. In order to satisfy this condition, one of the resonant terms with $\gamma_m = -i\sqrt{k^2 - q_m^2}$ in the denominator in (D.1) must become infinity as well. The divergence of any of these terms is achieved if their denominator is equal to 0, which leads to the condition

$$(3.42) \qquad\qquad \omega = c_0 \, |q \pm 2\pi m/d|, \;\; m = 0, 1, 2, \dots.$$

The obtained dispersion relation is exactly the linear dispersion for sound in the empty lattice approximation.

In the first (linear) approximation over $z$ and $\epsilon$, the same resonant terms need to remain in the lattice sum:

$$(3.43) \qquad\qquad F(0) \approx - \sum_{m=-\infty}^{\infty} \frac{2i}{\gamma_m d} \approx \frac{2}{d} \sum_{m=-\infty}^{\infty} \frac{1}{\sqrt{k^2 - (q + 2\pi m/d)^2}}.$$

Since I am analyzing the level splitting near the $\Gamma$-point, it is convenient to represent the parameter $k = \omega/c_0$ as $k = 2\pi m/d + \Delta k_m$, where $\Delta k_m$ is a small correction.

As was already established, the eigenmodes of the chain of perforated shells are leaky waves, and the numerically calculated dispersion bands $f(q)$ shown in Fig. 3.3 contain small negative imaginary part which causes the exponential decay of the signal intensity with time $t \to \infty$. However, evaluating the function $F(n)$ (see (3.35)) for the values of $k$ from the lower complex plane shows that the function is singular, which is due to the diverging sum of the Hankel functions of the complex argument. Indeed, since the Hankel function of the first kind asymptotically behaves as $H_n(kl'd) \approx \sqrt{2/(\pi kl'd)} \exp(ikl'd - i\pi n/2 - i\pi/4)$, and if $k$ has any negative imaginary part, the exponential term will grow infinitely with $l'$. This issue is addressed in Appendix D by means of analytical continuation of the function $F(n)$ into the region Im $k < 0$. The function $F(n)$ can further be replaced by the fast convergent series (D.1)-(D.3), with the only condition that one specifies which branch of $\sqrt{k^2 - q_m^2}$ is to be used.

As is elaborated in Appendix A, the branch cut defining how to calculate the complex square root function should be chosen along the negative imaginary axis, in order to guaran-

tee the correct behavior for propagating, leaky, and nonradiative waves. However, the latter argument was developed for the case of plane waves having spatial dependence $e^{ik_x x + ik_z z}$, and thus is not immediately applicable to the scattered sound expanded over cylindrical waves. Still, one may consider the acoustic field far away from the chain, where it can be expanded over the plane waves with the parallel to the chain wave vector components $q_m$ and perpendicular to the chain components $\gamma_m = \sqrt{k^2 - q_m^2}$. Consequently, if using the branch cut along the negative imaginary axis in $\sqrt{k^2 - q_m^2}$ provides the correct physical behavior of all waves in the expansion over plane waves, then this correct behavior is preserved after switching from the basis of plane waves to cylindrical waves.

Now, with the uniquely defined branch for $\gamma_m$ one can solve the dispersion equation (3.41) with $F(0)$ in the form (3.43). For any band in the band structure enumerated by the index $m$, one can omit all the terms in the sum in (3.43) except for the two with $m' = m$ and $m' = -m$ in order to calculate the level repulsion near the $\Gamma$-point. Note that if the repulsion is to be calculated near the edge of the Brillouin zone, one must keep the terms with $m' = m$ and $m' = -m - 1$, which give the principal contribution. In the region near the band gap opening at the $\Gamma$-point, where $k = \omega/c_0 \approx 2\pi m/d$ and $q \ll \pi/d$, it is possible to simplify the denominators in (3.43) to $\sqrt{k^2 - q_{\pm m}^2} \approx \sqrt{(4\pi m/d)(\Delta k_m \mp q)}$. The dispersion equation then takes the following form in the linear approximation:

$$(3.44) \qquad \frac{1}{\sqrt{\Delta k_m - q}} + \frac{1}{\sqrt{\Delta k_m + q}} = -i\sqrt{4\pi md}\,(z - \epsilon)^{-1}.$$

Obviously, only when both terms in the left-hand side are purely imaginary does this equation have a unique solution. Since the value of $q$ is assumed to be positive, one must require that $\Delta k_m < 0$ and also $|\Delta k_m| > q$. Negative values of $\Delta k_m$ describe the *lower branch* of the dispersion curve near the frequency $\omega = 2\pi m c_0/d$. The equation for $\Delta k_m$ can further be rewritten as

$$(3.45) \qquad \sqrt{|\Delta k_m| + q} + \sqrt{|\Delta k_m| - q} = 2\sqrt{\frac{\Delta k_m^2 - q^2}{\kappa_m}},$$

where $\kappa_m = (z - \epsilon)^2/\pi md$. This equation is valid for any value of the Bloch vector $0 < q < |\Delta k_m|$. I will solve this equation in the close vicinity of the $\Gamma$-point, where $q \ll |\Delta k_m|$,

as it is sufficient for calculations of the band gap width and the qualitative behavior of the dispersion branch. It immediately follows from (3.45) that $\Delta k_m(q=0) = \kappa_m$, which gives the level shift at the $\Gamma$-point. If the both parts of (3.45) are expanded in series over $q$ up to the quadratic terms, one obtains a quadratic equation for $|\Delta k_m|$. This equation has two solutions, but only the one which is physically meaningful must be chosen:

$$(3.46) \qquad \Delta k_m = -\kappa_m - \frac{3q^2}{4\kappa_m}.$$

Based on this result, I arrive at the dispersion relation for the lower branch of the doublet:

$$(3.47) \qquad \omega(q) = \frac{2\pi m c_0}{d} + \Delta k_m c_0 \approx \frac{2\pi m c_0}{d} - \kappa_m c_0 - \frac{3q^2}{4\kappa_m} c_0.$$

This dispersion relation possesses all the same properties as the one in the nearly free electron approximation. Specifically, at the $\Gamma$-point the group velocity vanishes, the band gap is formed due to the red shift of the eigenfrequency, and its width is proportional to the square of the perturbation parameter, $\kappa_m c_0 \propto (z - \epsilon)^2$. The obtained dispersion relation appears to be purely real and satisfying the nonradiative condition $k^2 - q_{\pm m}^2 < 0$. The imaginary part of the spectrum is recovered when the sum (3.43) is approximated more accurately by keeping the terms with $|m'| \neq m$.

As for the *upper* branch of the dispersion curve, one may not treat $\Delta k_m$ as a purely real value, so a complex solution of (3.44) has to be found. Since the exponential decay with time is expected for all complex solutions, the solution is restricted to the lower part of the complex plane, where $\mathrm{Im}\,\Delta k_m = \mathrm{Im}\,\omega/c_0 < 0$. However, the right-hand-side of (3.44) remains to be purely imaginary, and therefore the real parts of $(\Delta k_m - q)$ and $(\Delta k_m + q)$ need to have opposite signs. This implies that the term $(\Delta k_m - q)$ must lie in the third quadrant, and the term $(\Delta k_m + q)$ — in the fourth quadrant. Because of that the two inequalities $\mathrm{Re}\,(\Delta k_m + q) > 0$ and $\mathrm{Re}\,(\Delta k_m - q) > 0$ must be valid, which is achieved provided $|\mathrm{Re}\,\Delta k_m| < q$. The latter condition cannot be satisfied when $q = 0$, hence the upper band never reaches the $\Gamma$-point. In (3.44), the first and the second terms belong to the third and the first quandrants, respectively, given the chosen branch cut along the negative imaginary
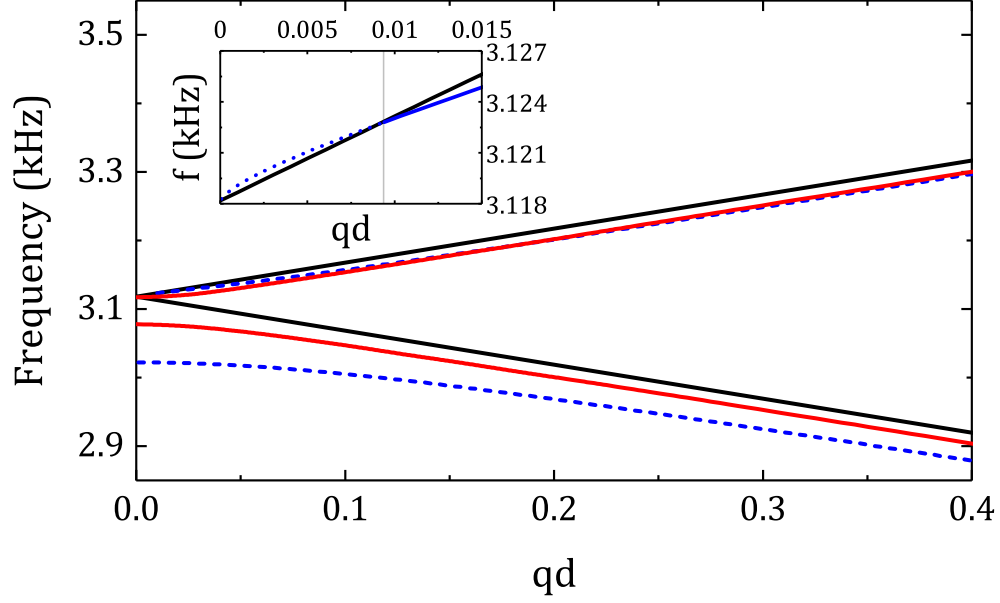
FIGURE 3.4. Band structure of an infinite periodic chain of shells in inviscid air environment. Solid black and red lines respectively show linear dispersion in air and dispersion calculated from (3.36) (same as in Fig. 3.3 (a)). Dashed blue lines show the dispersion obtained from the perturbation theory equations (3.47) and (3.51). The inset shows the narrow region $qd < q_c d \approx 0.01$ near the $\Gamma$-point where the upper band does not exist. The leaky upper mode beyond $q = q_c$ is shown by blue line.

axis. With that, I rewrite the dispersion equation (3.44) using the dimensionless variables $x = q/\kappa_m$ and $y = \Delta k_m/\kappa_m$ as

$$\frac{1}{\sqrt{y-x}} = -2i - \frac{1}{\sqrt{y+x}}. \tag{3.48}$$

This equation can be squared and brought to a biquadratic form over $x$, as both its left- and right-hand sides lie in the same (third) quadrant. After executing the transformation mentioned one obtains:

$$4x^4 + x^2(1 - 8y^2 - 4y) + 4y^4 + 4y^3 = 0. \tag{3.49}$$

The exact solution of this equation is not of much importance, whereas finding the behavior of $y(x)$ in the region of small $x$ and $y$ is crucial for understanding the features of the upper

dispersion band. The series solution that satisfies (3.49) runs over integer powers of $(x/2)^{2/3}$:

(3.50)
$$y(x) \approx e^{-i\pi/3} \left(\frac{x}{2}\right)^{2/3} + \frac{5}{3} e^{i\pi/3} \left(\frac{x}{2}\right)^{4/3} + \left(\frac{x}{2}\right)^2, \quad x << 1,$$

which defines the dispersion relation for the upper branch to be

(3.51)
$$\omega(q) = \frac{2\pi m c_0}{d} + \Delta k_m c_0 \approx \frac{2\pi m c_0}{d} + \kappa_m c_0 \left[ e^{-i\pi/3} \left(\frac{q}{2\kappa_m}\right)^{2/3} + \frac{5}{3} e^{i\pi/3} \left(\frac{q}{2\kappa_m}\right)^{4/3} + \left(\frac{q}{2\kappa_m}\right)^2 \right].$$

This relation is valid for small wavevectors, $q << \kappa_m$. Yet, the group velocity appears to grow infinitely close to the $\Gamma$-point, as $\partial\omega/\partial q \propto q^{-1/3}$, which is not a reasonable physical dependence here. However, there is no contradiction, as it was previously established that the condition Re $\Delta k_m < q$ must hold, which is numerically equivalent to $q > q_c \approx \kappa_m/20$. The latter indicates that within the interval $0 < q < q_c$, the solution does not exist and thus the mode does not propagate. The nonexisting part of the band is shown by the dashed line in the insert to Fig. 3.4 and is not visible in other figures, as the region $0 < q < q_c$ is extremely narrow. It is peculiar that, unlike the red-shifted lower band of the doublet, the upper branch is not blue-shifted as would be expected in the nearly free electron model. The width of the band gap is thus equal to

(3.52)
$$\Delta f = \frac{c_0 \kappa_1}{2\pi} = \frac{c_0 (z - \epsilon)^2}{2\pi^2 d},$$

making the gap opening strongly asymmetric. The gap width in the presented perturbation theory is calculated to be $\Delta f \approx 100$ Hz for the region near 3.1 kHz. This value is almost three times larger than the numerically obtained value of only 35 Hz (see Fig. 3.3). The observed mismatch arises from the fact that the small parameter of the perturbation theory $z = \frac{\pi k a}{2} \frac{i Z_p}{\rho_0 c_0}$ is not actually small, being $z \approx 0.95$ near the frequency $\omega = 2\pi c_0/d$. Even though the ratio of impedances $i Z_p/\rho_0 c_0$ is small, it does not guarantee that the parameter $z$ in the series of the perturbation theory is small as well, which results in poor estimation of the band gap. Nevertheless, the developed perturbation theory qualitatively recovers the asymmetry between the two bands in the doublet near the $\Gamma$-point, and is therefore of principal importance.

74

In general, the unusual structure of the band gap is caused by the two factors: the cylindrical geometry of the system and the weakness of the scattering, which is characterized by *imaginary* impedance $Z_p$. Similar effects have been discovered for leaky surface acoustic and electromagnetic waves propagating along periodically corrugated surfaces [64, 65]. The band structures in these cases also feature the asymmetric level repulsion and nonvanishing group velocity for the upper band in the doublet. The system described in this chapter exhibits the same anomalies as the systems with surface corrugations in [64, 65] since the eigenvalue problem for the periodic arrangement of shells in Fig. 3.2 requires expanding solutions over cylindrical functions, which is also the case for the surface modes being scattered by semi-cylindrical corrugations.

## 3.7. FEM Numerical Simulations

### 3.7.1. Transmission through the Finite Chain

In order to obtain the transmission properties of the finite chain of perforated shells, I numerically solve the set of equations (3.30) for different number of scatterers $2N + 1$ in the chain. The transmission coefficient, defined as

$$(3.53) \qquad T(f) = \frac{1}{2Np_0v_0} \int\limits_{-Nd}^{Nd} p_{tot}(d, y)v_{tot,x}^*(d, y)dy,$$

is then calculated and visualized in Fig. 3.5. Here $p_{tot}(x, y) = p + p_{sc}$ and $v_{tot,x}(x, y) = -(i/\omega\rho_0)\partial p_{tot}/\partial x$ are the the the total pressure and the $x$-component of the total velocity, respectively. I calculate the transmission spectrum for inviscid air (using (3.13) as the impedance of the shells) and for air with its real viscosity (using (3.12)). The value of the transmission coefficient is very close to one within a wide range of frequencies, which agrees with the numerical results reported in [32]. Still, there is a deep minimum around 3.1 kHz, and further I will show that it is caused by the resonant coupling of the incident sound with the eigenmodes of the chain. Comparing viscous and inviscid cases, one concludes that the deepness of the minimum is reduced by viscosity, and the resonance position is considerably red-shifted which is clearly visible in Fig. 3.5.
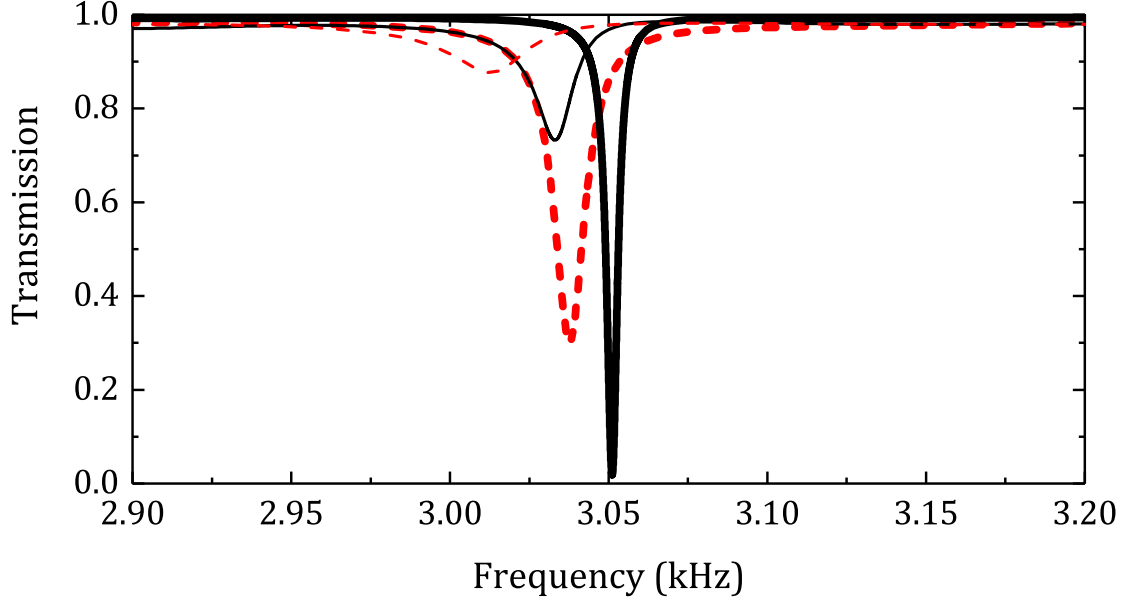
FIGURE 3.5. Transmission coefficient for the chain of 31 (dashed red lines) and 41 (solid black lines) perforated shells. Results for inviscid and viscous air are shown by thick and thin lines respectively.

Clearly, chains of perforated shells need to have sufficient length in order to establish the spectrum of eigenmodes, as the shells are weak scatterers. Otherwise, one will not achieve any pronounced behavior of the eigenmodes and therefore the minima in transmission, if any, will be quite shallow. Namely, even without the viscosity in the picture, there is hardly any visible minimum in the transmission spectrum of a 15-unit chain, and it will completely disappear when the viscosity is accounted for. Increasing the number of scatterers makes the resonant minimum deeper and sharper, and also blue-shifts it. For a very long chain, the minimum converges on a specific position. The minima shown in Fig. 3.5 approach the frequency of 3078 Hz as the length of the chain is increased. This frequency, 3078 Hz, is the first nonzero eigenfrequency at the $\Gamma$-point in the band structure of the infinite periodic chain of shells in ideal air environment (see Fig. 3.3). Fig. 3.6 shows how the deepness of the resonant minimum and its position depend on the number of units in the chain. It is interesting that the position of the resonance (left panel of Fig. 3.6) converges to 3078 Hz much slower than the transmission at minimum (right panel of Fig. 3.6) approaches zero,

76
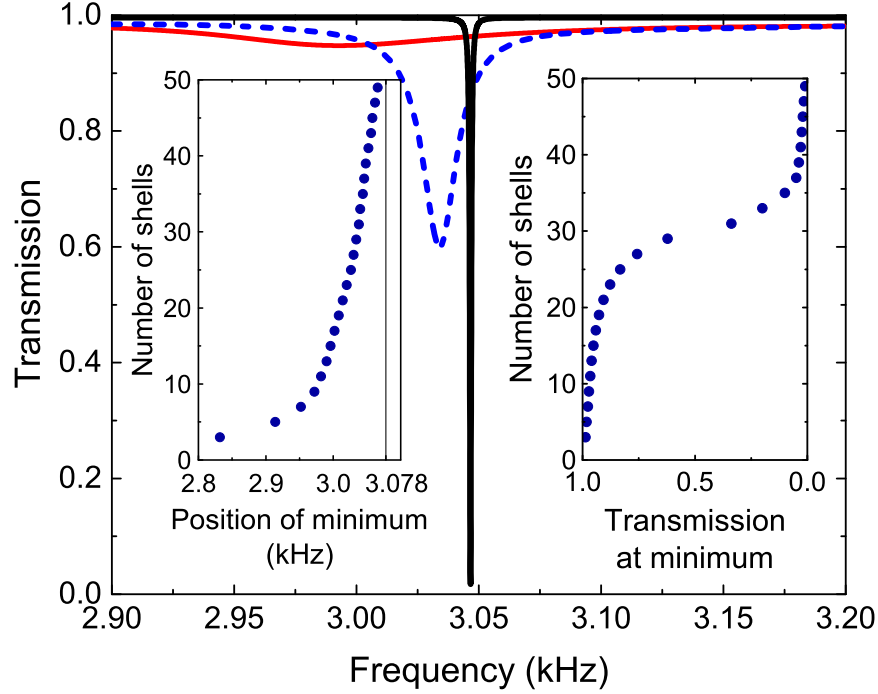
FIGURE 3.6. Transmission coefficient for the chain of 15 (solid red line), 29 (dashed blue line), and 37 (solid black line) perforated shells. Results are obtained for inviscid air. Inserts: position (left panel) of the transmission minimum and its deepness (right panel) vs number of shells in the chain.

making the latter more sensitive to the number of scatterers.

3.7.2. Transmission through the Infinite Chain

Now, I will calculate the transmission properties of the infinite chain of scatterers, which requires solving the set of equations (3.34). In the case of the normal incidence of sound, the transmission vanishes exactly at $f = 3078$ Hz, which corresponds to the frequency of the lower level in the doublet formed due to the level repulsion (see Fig. 3.3(b)). One can verify via numerical simulations that the distribution of pressure over the $y$-axis is symmetric (antisymmetric) for the eigenmodes describing the lower (higher) level of the doublet. It is known that an external plane wave can only excite symmetric modes at normal incidence. The antisymmetric modes, in particular, the upper level of the doublet, cannot be excited in such geometry. Such modes are commonly referred to as deaf modes [82, 104]. Once
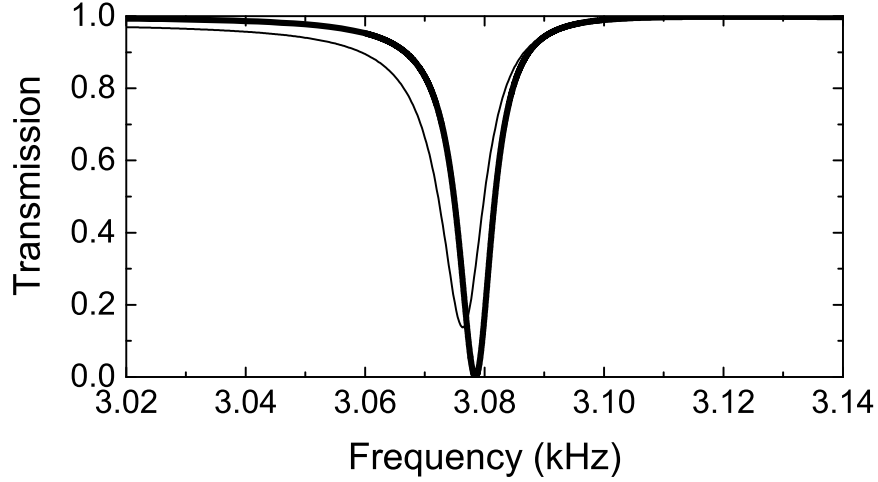
FIGURE 3.7. Transmission spectrum of an infinite chain of perforated cylindrical shells at normal incidence. Thick and thin lines are for inviscid and viscous air, respectively.

the symmetric mode in 1D chain of scatterers is directly excited, the transmission is practically 100% suppressed. The energy is then mostly reflected back (about 85%), or equally redirected by $\pm 90°$ towards both ends of the chain (remaining 15%).

Despite being a deaf mode, an antisymmetric mode may still be excited indirectly. As was reported in [97], one may achieve the effect of redirection of sound in a sonic crystal of elastic rods due to the Poisson-like effect. Namely, the incoming sound excited the flexural modes of the rods, and those modes coupled to the antisymmetric deaf modes via evanescent modes. Such indirect excitation allowed only a maximum of 46% of acoustic energy to be reflected or redirected at the frequency of the mid-gap.

It is important to note from Fig. 3.7 that the resonance in a chain surrounded by viscous air is not significantly altered by dissipation, specifically, there is only a slight red shift and almost no broadening of the resonance (the width remains approximately $\Delta f = 30$ Hz). As is seen from Fig. 3.5 and Fig. 3.6, the most important factor defining the shape of the resonant minimum is the length of the chain. The viscosity is then does not qualitatively change the observed phenomena, and only weakly contributes to the quantitative results. Due to viscosity, the transmission at the resonance does not reach zero and becomes finite.

Still, about 80% of acoustic energy experiences either reflection or redirection as the symmetric leaky modes of the chain are excited. The leaky modes are not proper spectral modes, and one benefits from this fact since such modes can be directly excited by external sound due to their interaction with the environment. Moreover, the inequality $\text{Im } f \ll \Delta f \ll \text{Re } f$ holds, and for that reason the resonant excitation is well established.

When the external acoustic plane wave is incident at an angle, there is no symmetry of the incoming wave over the $y$-axis, which makes the excitation of both symmetric and antisymmetric eigenmodes possible. For that reason, the two minima appear in the transmission spectra in Fig. 3.8. In order to find the position of each minimum, the wave vectors of the incoming sound $\mathbf{k}$ and the eigenmode $q$ must satisfy the following relation:

$$(3.54) \qquad\qquad k_y = (2\pi f/c_0)\sin\theta = q(f).$$

The latter condition, which requires matching of the tangential components of the wave vectors, is the mathematical form of the phenomenon known as the Wood's anomaly [68]. As an example, the resonant minimum in the transmission spectrum Fig. 3.7 can be considered as a Wood's anomaly since at the resonant frequency 3078 Hz, the wavelength of sound in air is 11.1 cm, which closely matches the period of the chain $d = 11$ cm [32]. In the reduced zone scheme, the condition (3.54) can be satisfied for multiple frequencies, depending on the angle of incidence $\theta$. For normal incidence, $\theta = 0°$, the corresponding value of the wave vector is $q = 0$, which formally enables any dispersion band to be excited by external sound. Together with the symmetry consideration one concludes that normal incidence only triggers excitation of lower levels of the doublets at the $\Gamma$-point.

In general, Fig. 3.3 shows the points of crossing of the straight dashed lines given by $q = 2\pi f \sin\theta/c_0$ with the dispersion bands, where the condition (3.54) is satisfied. The three dashed lines correspond to the angles of incidence $\theta = 5°$, $\theta = 10°$ and $\theta = 15°$. For $\theta = 5°$, the first two crossings occur at $f \approx 2.85$ kHz and $f \approx 3.40$ kHz. Consequently, the transmission minima in Fig. 3.8 are observed near these frequencies. These two minima are separated by the interval of about 550 Hz, which is significantly larger than either
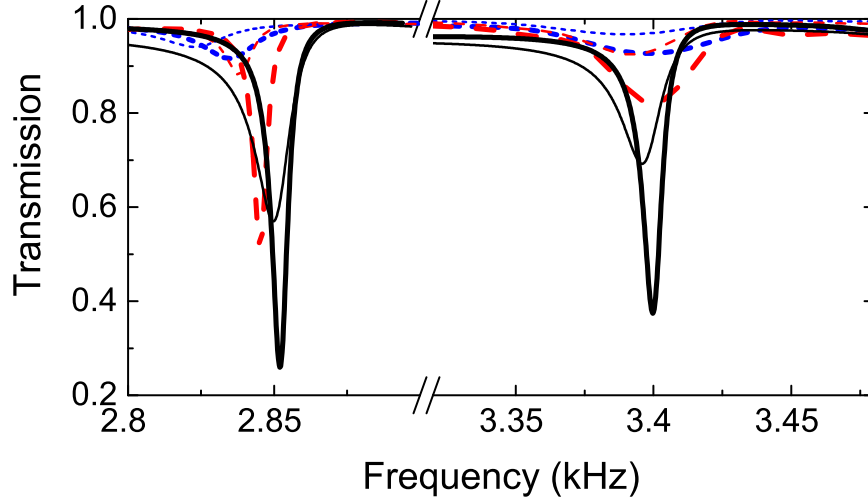
FIGURE 3.8. Transmission spectrum at oblique incidence, $\theta = 5°$. Blue short-dashed, red long-dashed, and black solid lines are for the chains containing 61, 121, and infinite number of cylindrical shells, respectively. Thick and thin lines show the results for inviscid and viscous air. Note that two resonances are separated by $\approx 550$ Hz in frequency (compare to the doublet width 35 Hz).

the width of each minimum or the width of the doublet at the $\Gamma$-point. The latter fact makes each minimum well-resolved, and is explained by the difference in the dispersion of the two bands. Since the upper (antisymmetric) and the lower (symmetric) bands are the continuations of the doublet levels at the $\Gamma$-point, they exhibit normal and anomalous dispersion, respectively, meaning the separation between their respective eigenfrequencies is increased away from the $\Gamma$-point.

An interesting anomaly arises in the scattering of sound by the chain of perforated shells as a result of the bands having different dispersion. One can see that the direction of the phase velocities for both eigenmodes is the same as the direction of the wave vector $\mathbf{q} = q\hat{y}$. The group velocity, however, acquires its sign from the slope of the corresponding band curve, so for the lower band it is opposite to $\mathbf{q}$. As the group velocity points in the direction of the energy flow, it appears that the scattering of the incoming wave occurs in the "wrong" direction.

Fig. 3.9 and Fig. 3.10 visualize the angular distribution of intensity of scattered sound

for the angle of incidence $\theta = 5°$. In Fig. 3.9, the frequency of 3.40 kHz is selected for the incoming wave to allow coupling with the upper dispersion band (see Fig. 3.3). The scattered sound propagates almost exclusively in the direction of the parallel component $k_y \hat{y}$ of the wave vector in the incoming wave, due to the normal dispersion of the band. In contrast with that, the scattering at the frequency of $f = 2.85$ kHz, where the matching condition (3.54) holds for the lower band with anomalous dispersion, occurs in the direction against $k_y \hat{y}$ and produces anomalous pattern for the scattered field (see Fig. 3.10).

Both Fig. 3.9 and Fig. 3.10 also show the results obtained for viscous air by green dashed lines. Due to viscosity of air, the scattered sound is of lower intensity in all the directions. Despite that, the coupling to the eigenmodes remains effective, and the spikes of intensity in the normal and "wrong" directions remain well-pronounced.

There is no great difference between the intensities of the normal and anomalous scattering for the angles of incidence $\theta \geq 5°$. The results in Fig. 3.7 serve as the evidence for the latter claim, showing that the values of the transmission coefficients in the minima differ by 10%, with the lower-frequency minimum being deeper. For smaller angles $\theta$, however, the eigenmode with normal dispersion produces much weaker minimum as it becomes a deaf mode towards $\theta = 0°$, and as a result the anomalous scattering dominates. When $\theta \to 0°$, the frequency interval between two resonant minima in the transmission spectra approaches the width of the doublet, which may be hard to see from the plots as the minimum corresponding to normal scattering vanishes completely.

The plots in Fig. 3.7-Fig. 3.10 clearly demonstrate the effect of redirection of incoming sound by an angle of about $90°$. This becomes possible in a chain of weak scatterers when the frequency and the angle of incidence satisfy the matching condition (3.54).

### 3.7.3. Splitting of Acoustic Signal

Additionally, the chain of perforated shells may serve as a splitter of a bi-frequency acoustic signal. Let us consider an acoustic beam which is created by mixing two monochromatic sound waves and is incident on the chain at a certain angle $\theta$. The described beam will produce two monochromatic signals propagating along the chain in the opposite directions,
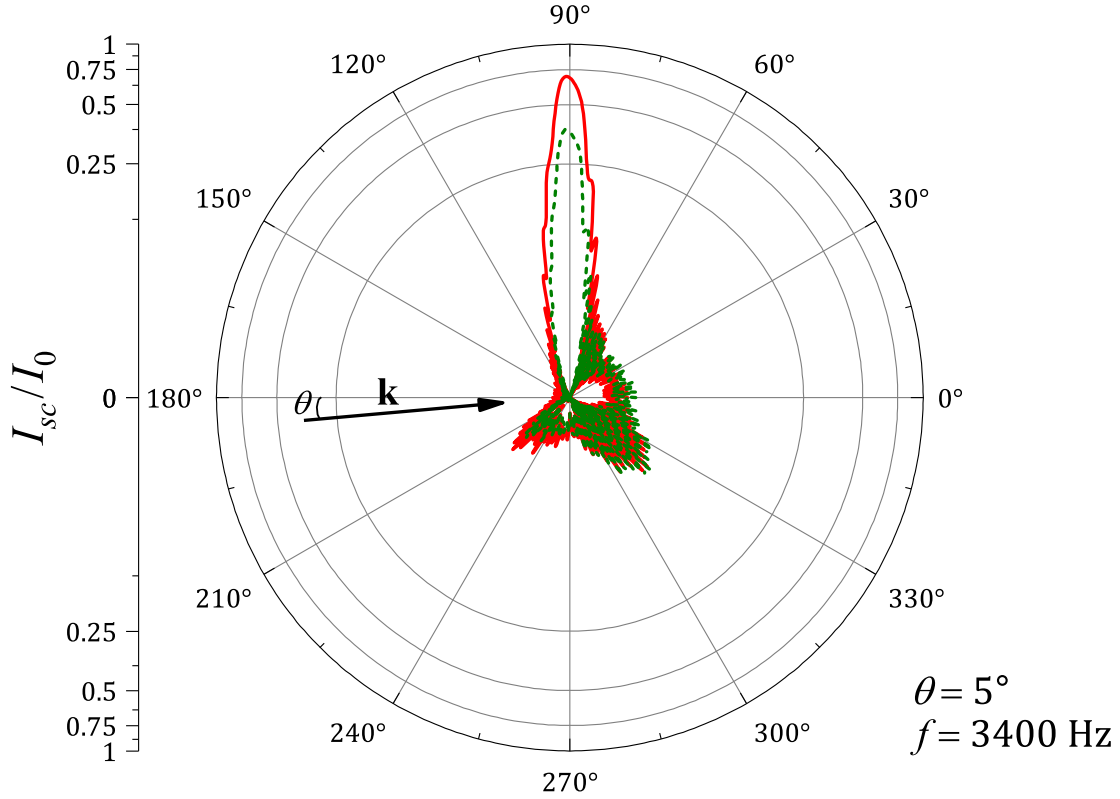
FIGURE 3.9. Polar diagram showing distribution of intensity of scattered sound of frequency $f = 3400$ Hz (upper band in the doublet having normal dispersion). Solid-red and green-dashed lines are for inviscid and viscous air, respectively. Black arrow shows the direction of the incident wave. An essential part of scattered sound wave propagates along the chain in the direction of the wave vector $\mathbf{k}_\parallel$. Note logarithmic scale along radius.

provided that both frequencies of its components are solutions of (3.54). In the case of almost normal incidence, the detuning between the components needs to be much smaller than their frequencies (such bi-frequency signal is called a beat). Due to closeness to the Γ-point, the redirection of the high-frequency component is suppressed and the overall efficiency of splitting is reduced.

In Fig. 3.11, a bi-frequency signal is incident at an angle of $10°$ on the finite-length chain containing 25 perforated shells. The two monochromatic components of the signal have frequencies of 2625 Hz and 3715 Hz, respectively, which are the frequencies of the two
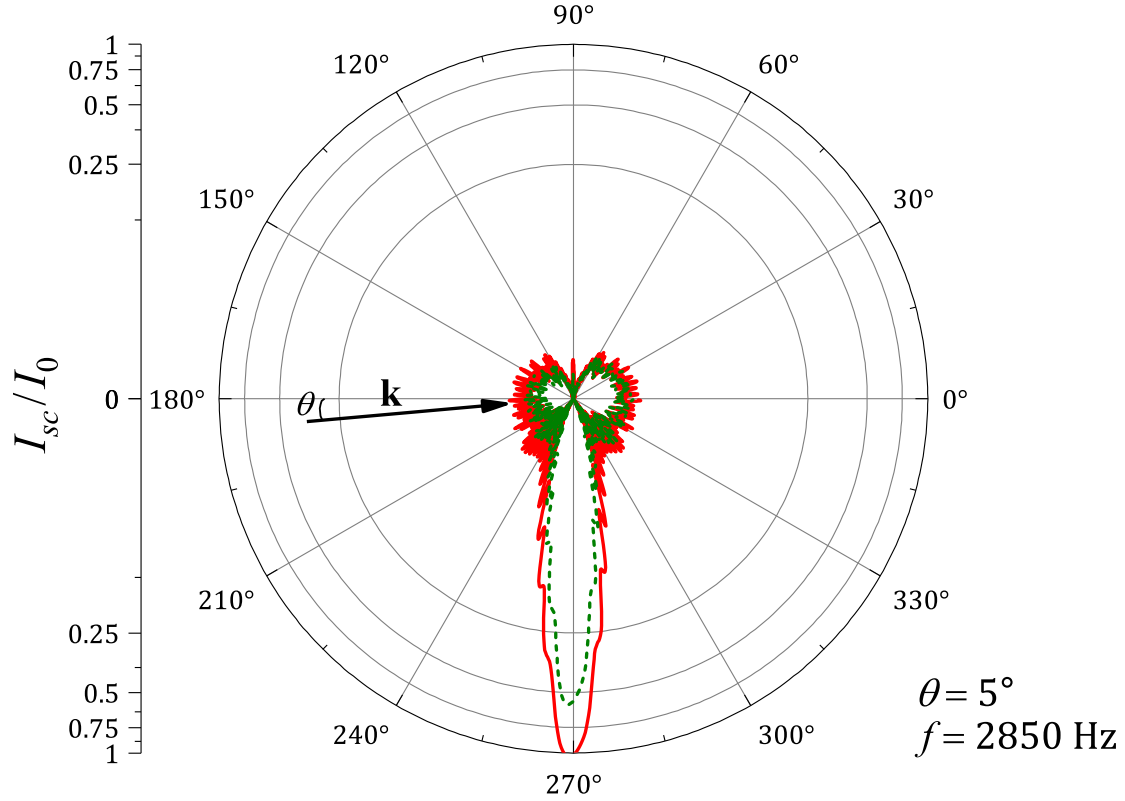
FIGURE 3.10. The same as in Fig. 3.9 but for the frequency $f = 2850$ Hz, corresponding to the lower band of the doublet, having anomalous dispersion. In this case the scattering occurs in the "wrong" direction, i.e., opposite to $\mathbf{k}_\parallel$.

eigenmodes of the chain that can be excited by the wave incident at $10°$ (see Fig. 3.3). A substantial part of acoustic energy propagates through the chain, as the angle of incidence is not very small and the number of shells is not very large. Nevertheless, one can observe a clear pattern of split fringes towards either end of the chain, for both ideal (Fig. 3.11a) and viscous (Fig. 3.11b) air.

The chain of perforated shells, being a purely mechanical system, demonstrates quite good efficiency of splitting. The amounts of energy that are converted into the low-frequency component, propagating down (anomalous scattering), and high-frequency component, propagating up (normal scattering), are as high as 8% (5%) and 10% (7%), respectively, for the chain in ideal (viscous) air environment.
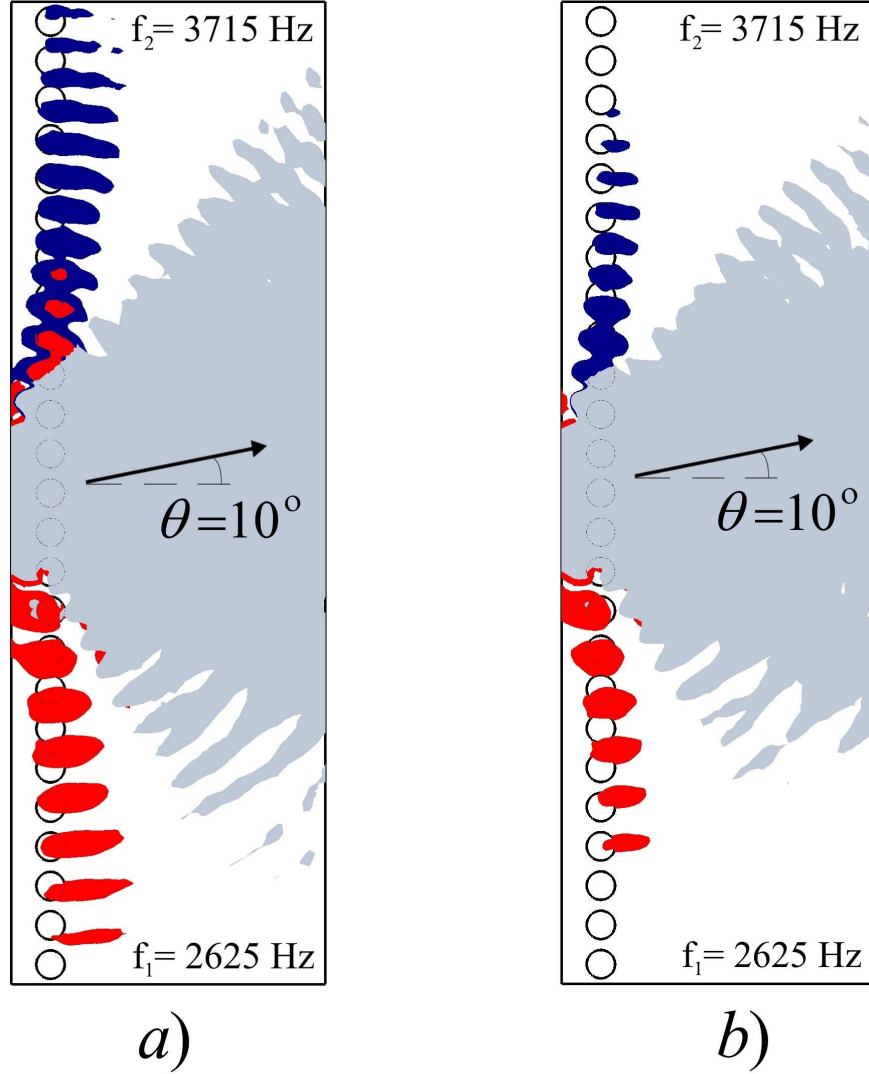
FIGURE 3.11. Distribution of intensity of a bi-frequency signal (with $f_1 = 2625$ Hz and $f_2 = 3715$ Hz) transmitted through a chain of 25 perforated shells. The angle of incidence is 10° and the background air is inviscid (a) and viscous (b). The central part of the diffraction pattern (shown in grey) is a mixture of two sound waves with frequencies $f_1$ and $f_2$. The red and blue fringes are the split monochromatic components. The low-frequency component (red) exhibits anomalous scattering, propagating against the "natural" direction. The high-frequency component (blue) follows the "natural" direction due to its normal dispersion.

## 3.8. Summary

This chapter presents a rigorous study of the interaction between the acoustic waves and the periodic chain of thin perforated cylindrical shells, which results in redirection and splitting of incident sound. The problem of diffraction of sound by the periodic arrangement of shells is solved analytically in impedance approximation, applicable for situations with both ideal and viscous background fluid. The transmission coefficient is calculated for infinite and finite-length chains within a wide range of frequencies, and agrees well with earlier numerical and experimental results reported in [32] and further expanded in [29].

To gain more insights into the predicted phenomena, the dispersion equation for the infinite periodic chain is derived, and the eigenmodes are then numerically obtained for aluminum scatterers in air. Weak coupling between the scatterers and sound causes the eigenmodes to be leaky modes, propagating with phase velocity close to the speed of sound in air and slowly radiating energy away from the chain. The eigenmodes can be resonantly excited by the incident sound, leading to sharp minima in the transmission spectrum at the frequencies satisfying specific matching condition.

At normal incidence, the coupling of a monochromatic acoustic wave is only possible to the symmetric chain eigenmode, which results in a single deep minimum in the transmission. The antisymmetric mode, no matter how close to the symmetric mode frequency-wise, cannot be excited via normal incidence. With this, equal parts of the incoming sound are redirected in both directions along the chain.

When the incidence is oblique, the external wave can couple to both symmetric and antisymmetric modes, and that causes two deep minima to appear in the transmission spectrum. These minima are well-resolved even for viscous air. Since the symmetric and antisymmetric modes exhibit anomalous and normal dispersion, respectively, the anomalous scattering is strongly manifested in the system. The scattering of acoustic energy along the chain in the opposite direction with respect to the direction of incidence is shown to be a strong effect, caused by the resonant coupling between the external sound and the symmetric mode. Consequently, the chain of perforated scatterers can effectively serve as a sound

splitter. Namely, a sound beam consisting of two (or more) monochromatic components, which match the frequencies of symmetric and antisymmetric modes and thus have different dispersion, is split into two parts propagating in opposite directions along the chain.

In order to back the theoretical predictions, one needs to perform further experimental work focused on designing and testing devices for filtering and splitting of sound waves at selected frequencies.

CHAPTER 4

EFFECTS OF THE EPSILON-NEAR-ZERO TRANSITION LAYER ON THE
PROPAGATION OF SURFACE PLASMON POLARITONS

4.1. Introduction

A system consisting of dielectric and conducting regions can support a specific type of electromagnetic excitations — surface plasmon polaritons (SPPs), — that are inherently confined in the vicinity of the interface between the two media. Such excitations propagate in a self-sustainable manner, where the electromagnetic field impinging the conductor (usually a metal) accelerates the charges below the the metallic surface, and in their turn, the oscillating charges emit the coherent radiation back into the dielectric. The amplitudes of both the charge and the field oscillations decay exponentially away from the interface, and for that reason the SPPs are extremely sensitive to the surface conditions. The SPPs find applications in a large number of areas of research and technology, ranging from optoelectronic devices and near-field imaging to tumor treatment and solar cell design [2, 3, 84].

The emergence of metamaterials allowed realization of unconventional material properties in physical devices, which led to the observation of quite unique electromagnetic phenomena such as, for example, negative index of refraction [102, 72, 86]. Besides the possibilities to achieve negative dielectric permittivity and/or magnetic permeability, metamaterials can be engineered to create regions where the refractive index is almost zero [83]. The latter manifests in either sophisticated metal-dielectric compounds or, what is more surprising, even in systems built from the dielectric materials only [70].

While the propagation of electromagnetic waves through such epsilon-near-zero (ENZ) regions has been studied to a certain extent [36], it is still of great interest to study the corresponding behavior of the surface plasmons. Moreover, I will explain in this chapter that a thin ENZ layer always emerges at any metal-dielectric interface which thus qualitatively modifies the SPP properties. Consequently, one will be able to tune the plasmonic properties by applying an external electrostatic field to the transition layer and thus gaining control

87

over its width.

## 4.2. Metal-Dielectric Interface

In the simplest case of the SPP propagation along the planar metal-dielectric interface, one typically views the two media as perfectly uniform materials, with the boundary between them being a flat and infinitesimally thin plane. Naturally, neither the unavoidable surface roughness of any real experimental sample, nor the possible material defects or impurities are accounted for in such a representation. The scattering of the SPP on the various types of surface defects is extensively discussed, for example, in the review [108], so in this chapter, I will restrict the discussion to the defect-free scenario, which, however, still allows for a nontrivial interface structure.

The material properties, e.g. the electron density $n$ and the dielectric permittivity $\epsilon$, must suffer a discontinuity in the case of the ideal interface, which is not physically sound for any real contact between the two media. Specifically, on a microscopic level, the electrons are confined within the bulk of the metal, yet the essentially quantum nature of their motion presents a nonzero probability of tunneling through the potential barrier of the ion lattice, and thus a sparse cloud of electrons is formed just above the surface of the metal. Together with the reduced electron population below the surface of the metal, this cloud forms a thin transition layer where the material properties now change smoothly from their respective values in metal to those in dielectric. Since the dielectric constants of the two media have different signs — for dielectrics $\epsilon_d > 0$, while for metals $\epsilon_m < 0$ within the wide range of frequencies, — a critical point where $\epsilon = 0$ emerges close to the surface of the metal.

The exact solution for the electron density profile is known to feature the so-called Friedel oscillations [28], but in this study, I will assume the electron density to be monotonically decreasing away from metal (see Fig. 4.1). This simplification is justified by the fact that the qualitative behavior of the SPP does not depend on the particular choice of the electron distribution within the transition layer (see the discussion in [73]). As a result, the analysis presented below does not rely on a particular choice of the dielectric permittivity profile, as opposed to the studies [6, 35, 56], and, moreover, can be generalized to 2D or 3D geometries.
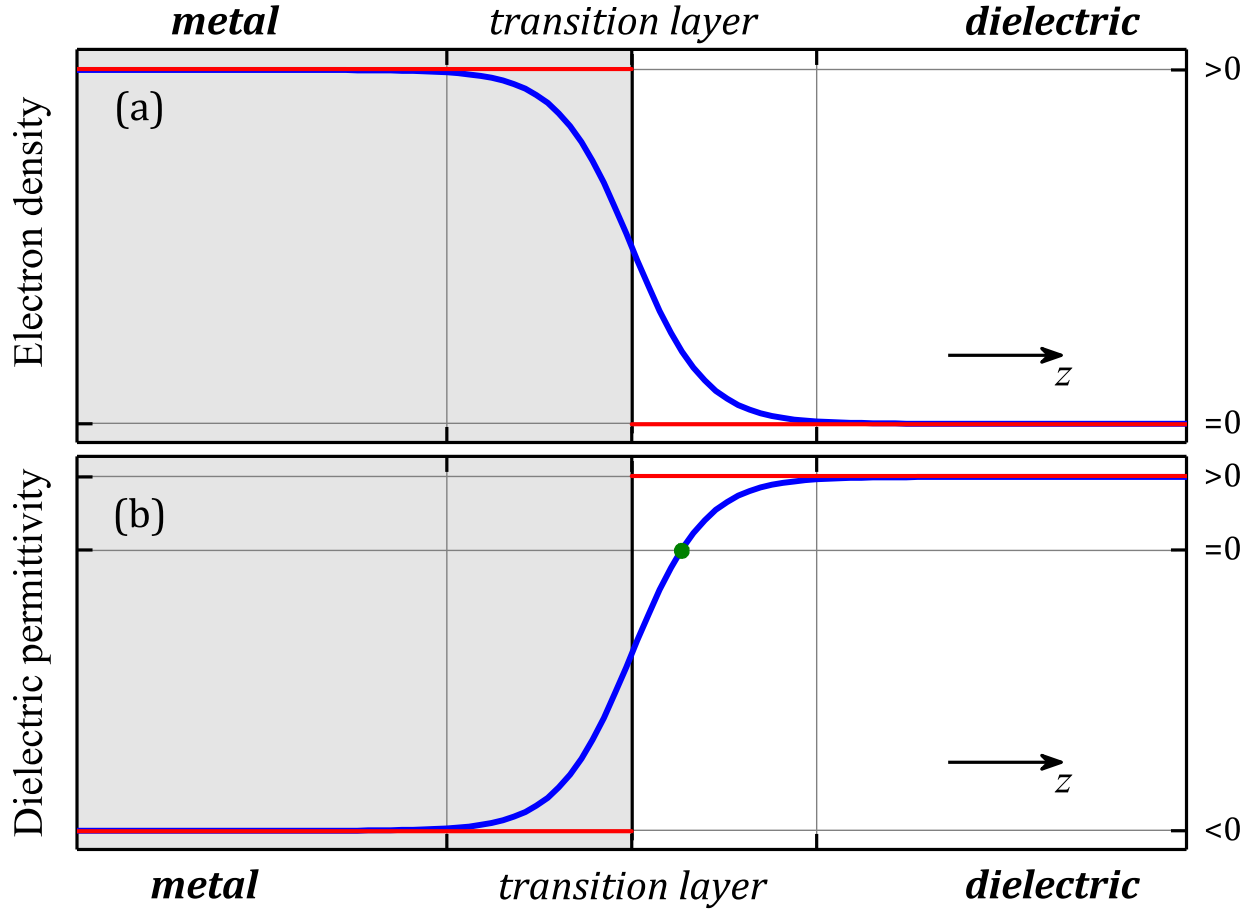
FIGURE 4.1. Electron density (a) and dielectric permittivity (b) profiles in the vicinity of the metal-dielectric interface. The qualitative behavior for these two quantities is shown assuming the ideally sharp boundary (red lines) and the smooth transition of material properties (blue curves). At some critical point located in the dielectric close to the metal surface, the dielectric permittivity becomes zero (green dot).

One may also wonder whether the use of macroscopic parameters to describe the ENZ layer is justified at all. Indeed, the typical size of the transition layer varies from several angstrom to several nanometers [6], which is at least an order of magnitude larger than the characteristic inter-atomic distance in the bulk of the media. This way the ENZ layer is populated by a sufficient number of spillout electrons, whose collective response to the electromagnetic field is then best described by the macroscopic dielectric permittivity.

## 4.3. Wave Equation for SPP Propagation

Let us consider a general case of a system consisting of dielectric and metallic regions, which alternate along the $z$-direction and are uniform and isotropic in $x$- and $y$-directions. In this system, the dielectric permittivity at any point can be written as $\epsilon = \epsilon(z)$, which may be either continuous or discontinuous function of the coordinate $z$.

The electromagnetic field in the system is a solution of the Maxwell's equations:

$$(4.1) \qquad \nabla \times \mathbf{E} = -\frac{1}{c}\frac{\partial \mathbf{H}}{\partial t},$$

$$(4.2) \qquad \nabla \times \mathbf{H} = +\frac{1}{c}\frac{\partial \mathbf{D}}{\partial t},$$

where the electric displacement is $\mathbf{D} = \epsilon\mathbf{E}$, and the uniform magnetic susceptibility of $\mu = 1$ is assumed.

It is well-known that any plasmonic mode supported by such structure must be a $p$-polarized (transverse magnetic or TM) wave propagating along the metal-dielectric interface. Therefore, without any loss of generality, one may seek the solutions for the SPP mode in the form of a monochromatic running wave

$$(4.3) \qquad \mathbf{H} = H_y(z)e^{ikx-i\omega t}\hat{\mathbf{e}}_y,$$

with the magnetic field $\mathbf{H}$ being parallel to the interface between media and perpendicular to the direction of propagation. Replacing thus the time derivative $\partial/\partial t$ with $-i\omega$ and eliminating the electric field from (4.1) and (4.2), one obtains the following wave equation:

$$\nabla \times \left(\frac{1}{\epsilon}\nabla \times \mathbf{H}\right) = \frac{\omega^2}{c^2}\mathbf{H},$$

which can be simplified and written down in terms of $H_y(z)$ as

$$(4.4) \qquad \frac{d}{dz}\left(\frac{1}{\epsilon(z)}\frac{dH_y}{dz}\right) + \left(\frac{\omega^2}{c^2} - \frac{k^2}{\epsilon(z)}\right)H_y(z) = 0.$$

This is the well-known equation for the $p$-polarized electromagnetic waves propagating in a nonuniform medium [54]. The subscript "$y$" will be omitted everywhere below as the magnetic field will be assumed to always point along the $y$-axis.

## 4.4. SPP Dispersion and Field Profiles: Ideal Case

Before addressing the SPP propagation problem along the transition layer, I will briefly summarize the main properties that are distinct to the SPP propagating along the sharp boundary. As will be seen further, knowing the SPP magnetic field distribution and its dispersion in the case of ideal boundary allows one to analytically calculate the SPP dispersion corrections due to the presence of the transition layer.

### 4.4.1. Single-Interface System

In the case of a discontinuous dielectric function profile

$$
(4.5) \qquad \epsilon_0(z) = \begin{cases} \epsilon_d, & z > 0, \\ \epsilon_m, & z < 0, \end{cases}
$$

which describes an ideal interface between metallic ($\epsilon_m < 0$) and dielectric ($\epsilon_d > 0$) semi-spaces, the plasmonic solution of the wave equation (4.4) is well-known [108]:

$$
(4.6) \qquad H_0(z) = H_0 \times \begin{cases} e^{-\kappa_d z}, & z > 0, \\ e^{+\kappa_m z}, & z < 0, \end{cases}
$$

where $\kappa_{d,m} = \sqrt{k^2 - \epsilon_{d,m}\omega^2/c^2}$, and the SPP dispersion $\omega = \omega_0(k)$ is given by

$$
(4.7) \qquad \frac{\epsilon_m}{\epsilon_d}\frac{\kappa_d}{\kappa_m} + 1 = 0
$$

or

$$
(4.8) \qquad k = \frac{\omega}{c}\sqrt{\frac{\epsilon_d \epsilon_m}{\epsilon_d + \epsilon_m}}.
$$

Note that in order to solve the wave equation with the discontinuous dielectric function, the boundary conditions for both magnetic and longitudinal electric fields must hold, namely, the functions $H_0(z)$ and $\epsilon_0^{-1}(z)\dfrac{dH_0}{dz}$ must be continuous.

From now on, the quantities with the subscript "0" will be describing the SPP properties in cases with ideal boundaries.

### 4.4.2. Double-Interface System

In the case of a discontinuous dielectric function profile

$$(4.9) \qquad \epsilon_0(z) = \begin{cases} \epsilon_{d+}, & z > +s, \\ \epsilon_m, & |z| < s, \\ \epsilon_{d-}, & z < -s, \end{cases}$$

which corresponds to a metal film of thickness $2s$ clad between two different bulk dielectrics (with permittivities $\epsilon_{d+}$ and $\epsilon_{d-}$, respectively), the SPP dispersion is implicitly given [108] by the following equation:

$$(4.10) \qquad \left( \frac{\epsilon_m}{\epsilon_{d+}} \frac{\kappa_{d+}}{\kappa_m} + 1 \right) \left( \frac{\epsilon_m}{\epsilon_{d-}} \frac{\kappa_{d-}}{\kappa_m} + 1 \right) = \left( \frac{\epsilon_m}{\epsilon_{d+}} \frac{\kappa_{d+}}{\kappa_m} - 1 \right) \left( \frac{\epsilon_m}{\epsilon_{d-}} \frac{\kappa_{d-}}{\kappa_m} - 1 \right) e^{-4\kappa_m s}.$$

Its solutions represent coupled modes, meaning that the SPP on one interface is intertwined with that on the other interface due to the small thickness of the film. For a sufficiently thick metal film, however, $s \to \infty$, the dispersion relation (4.10) naturally decouples into two:

$$(4.11) \qquad \frac{\epsilon_m}{\epsilon_{d\pm}} \frac{\kappa_{d\pm}}{\kappa_m} + 1 = 0,$$

which separately describe plasmonic modes existing independently on each interface (see the dispersion equation (4.7))

As for the SPP magnetic field, I write it down as follows:

$$(4.12) \qquad H_0(z) = H_0 \times \begin{cases} \mathcal{A} e^{-\kappa_{d+}(z-s)}, & z > +s, \\ \mathcal{B} e^{+\kappa_m z} + \mathcal{C} e^{-\kappa_m z}, & |z| < s, \\ \mathcal{D} e^{+\kappa_{d-}(z+s)}, & z < -s, \end{cases}$$

where the coefficients $\mathcal{A}$, $\mathcal{B}$, $\mathcal{C}$ and $\mathcal{D}$ are related through the boundary conditions at the interfaces $z = \pm s$. The continuity of $H_0(z)$ and $\epsilon_0^{-1}(z)\dfrac{dH_0}{dz}$ yields

$$(4.13) \qquad \mathcal{A} = \mathcal{B} e^{+\kappa_m s} + \mathcal{C} e^{-\kappa_m s}, \qquad -\frac{\kappa_{d+}}{\epsilon_{d+}}\mathcal{A} = \frac{\kappa_m}{\epsilon_m} \left( \mathcal{B} e^{+\kappa_m s} - \mathcal{C} e^{-\kappa_m s} \right),$$

$$(4.14) \qquad \mathcal{D} = \mathcal{B} e^{-\kappa_m s} + \mathcal{C} e^{+\kappa_m s}, \qquad +\frac{\kappa_{d-}}{\epsilon_{d-}}\mathcal{D} = \frac{\kappa_m}{\epsilon_m} \left( \mathcal{B} e^{-\kappa_m s} - \mathcal{C} e^{+\kappa_m s} \right).$$

The solvability of such homogeneous linear system is guaranteed when the dispersion equation (4.10) is satisfied, and thus one of the coefficients can be assigned an arbitrary value and the rest will be expressed through it.

Besides $s \to \infty$, there is another special case where the metal film is surrounded by the same dielectric, $\epsilon_{d+}, \epsilon_{d-} = \epsilon_d$. As a result, the plasmonic modes can be classified as either even (also called long-range) or odd (short-range) with respect to the coordinate $z$ (see [108] for additional details).

## 4.5. SPP Field Inside the Transition Layer

Despite the fact that the wave equation (4.4) has analytical solutions for only a few particular functions $\epsilon(z)$, it is possible to analyze the asymptotic behavior of the magnetic and electric fields within the ENZ transition layer in the general case. Let us assume first that in the vicinity of the critical point $z_c$, where the dielectric function vanishes, $\epsilon(z_c) = 0$, the latter can be expanded in series up to the first nonzero term as follows:

$$(4.15) \qquad \epsilon(z) \approx \epsilon'(z_c)(z - z_c).$$

Also, the term $\omega^2/c^2$ can be neglected in comparison with $k^2/\epsilon(z)$ in the wave equation. With these assumptions, the equation (4.4) can be written down as

$$(4.16) \qquad (z - z_c)\frac{d}{dz}\left(\frac{1}{z - z_c}\frac{dH}{dz}\right) - k^2 H(z) = 0,$$

and the solution for $H(z)$, when $|z - z_c| \ll \delta$, is expressed via modified Bessel functions as

$$(4.17) \qquad H(\xi) = k\xi \left(C^{(1)} I_1 (k\xi) + C^{(2)} K_1 (k\xi)\right),$$

where $\xi = z - z_c$. The parameter $\delta$ characterizes the width of the transition layer. From (4.17) the electric and magnetic fields asymptotically behave as

$$(4.18) \qquad H(\xi) \sim 1 + \frac{1}{2}k^2\xi^2 \ln k\xi,$$

$$(4.19) \qquad E_x(\xi) \sim \frac{1}{\epsilon(\xi)}\frac{\partial H}{\partial \xi} \sim \ln k\xi,$$

$$(4.20) \qquad E_z(\xi) \sim \frac{H(\xi)}{\epsilon(\xi)} \sim \frac{1}{\xi}.$$
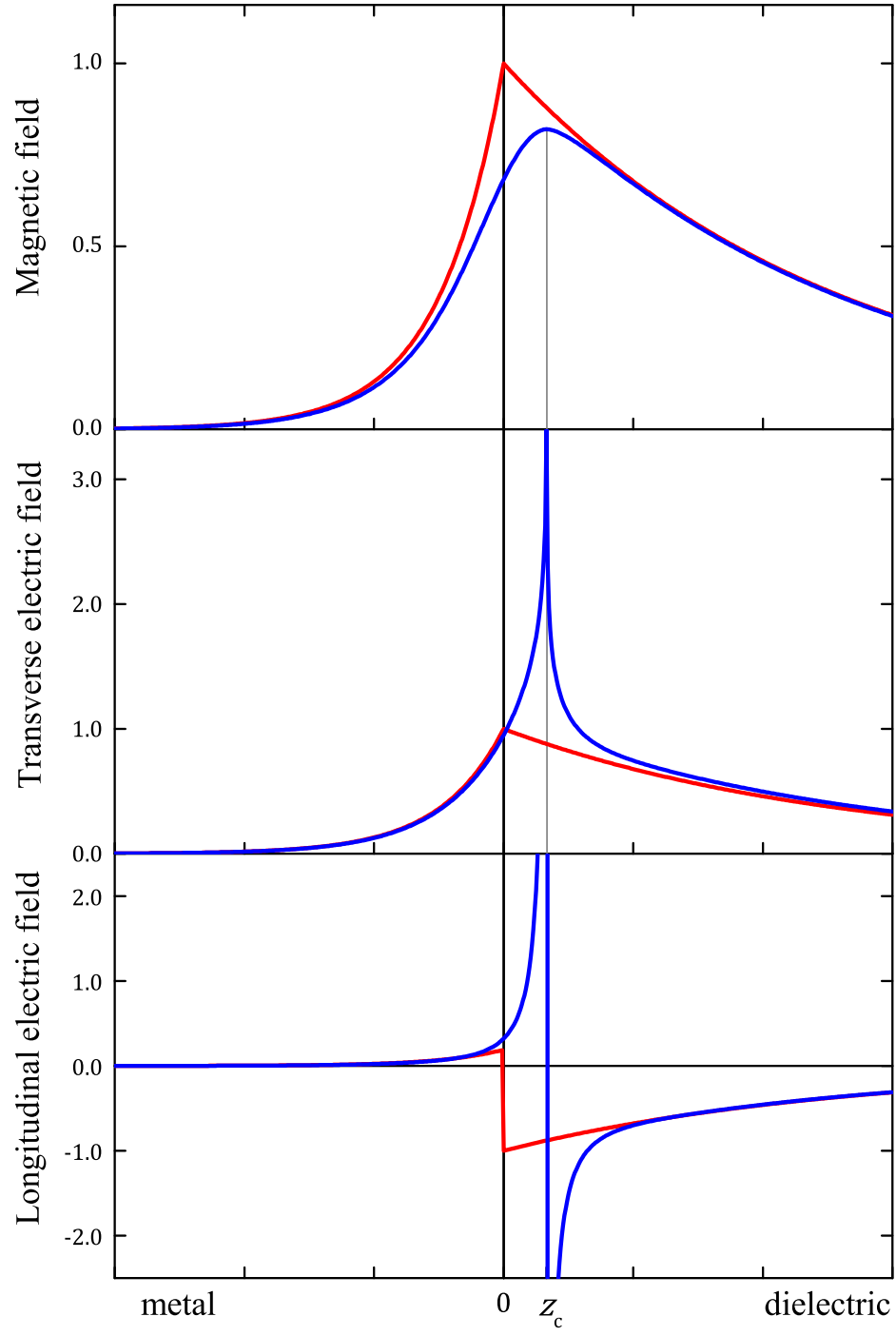
FIGURE 4.2. Asymptotic behavior of the SPP electromagnetic field (in a.u.) in the vicinity of the critical point $z_c$ (blue), in comparison with the case of no transition layer (red).

The analysis shows that both components of the electric field tend to infinity when $z \to z_c$ (see Fig. 4.2). Of course, such scenario is unrealistic, since there always are some inevitable losses within the real materials and one cannot have a pure real dielectric function, therefore the growth of the electric field is actually capped at a level determined by the imaginary part of $\epsilon(z_c)$ (see, e.g., [36]).

Nevertheless, the described electric field enhancement plays a defining role in opto-electronic devices. In particular, the processes of spontaneous photon emission, according to the Purcell effect, occur much more often when the emitter is placed in the strong electro-magnetic field [84].

### 4.6. Perturbation Theory

Since the thickness $\delta$ of the ENZ transition layer is typically of the order of several angstroms, this small parameter suggests that a perturbation theory can be developed to calculate the corrections to the plasmonic spectrum. From now on, the problem of the SPP propagation featuring ideal metal-dielectric interfaces will be considered an unperturbed problem, and the presence of the ENZ layers will be treated as a small perturbation. It is easy to see, however, that a continuous and smooth dielectric function $\epsilon(z)$ can never be represented as a sum of the unperturbed step-like function $\epsilon_0(z)$ and the small correction proportional to $\delta$, which means the wave equation (4.4) in its current form does not allow for the perturbative approach.

### 4.6.1. Integral Eigenvalue Problem

With this, the Fourier transformations of the magnetic field of the SPP and the dielectric function are introduced in the form of

$$(4.21) \qquad H(z) = \int\limits_{-\infty}^{+\infty} h(p)e^{ipz}dp, \quad \text{where} \quad h(p) = \frac{1}{2\pi}\int\limits_{-\infty}^{+\infty} H(z)e^{-ipz}dz,$$

and

$$(4.22) \qquad \frac{1}{\epsilon(z)} = \int\limits_{-\infty}^{+\infty} \eta(p)e^{ipz}dp, \quad \text{where} \quad \eta(p) = \frac{1}{2\pi}\int\limits_{-\infty}^{+\infty} \frac{e^{-ipz}}{\epsilon(z)}dz.$$

After applying the Fourier transform to the wave equation (4.4) as well, it takes the following integral form:

$$(4.23) \qquad \frac{\omega^2}{c^2} h\left(p\right) \;=\; \int\limits_{-\infty}^{+\infty} \left(k^2 + pp'\right) \eta(p - p') h(p') dp'.$$

Equation (4.23) can be regarded as an integral eigenvalue problem for the plasmonic spectrum $\omega = \omega(k)$, which is valid for the SPP on both ideal interface and interface with the ENZ transition. If the integral kernel $K(p, p') = (k^2 + pp')\,\eta(p-p')$ satisfies the condition $K(p, p') = K^*(p', p)$, which requires $\eta(p) = \eta^*(-p)$, the problem is then Hermitian, and its solutions are true SPP modes with real eigenfrequencies $\omega$.

For the unperturbed problem this is indeed the case, because the dielectric function $\epsilon_0(z)$ is pure real, and

$$(4.24) \qquad \eta_0(p) \;=\; \int\limits_{-\infty}^{+\infty} \frac{e^{-ipz}}{\epsilon_0(z)} dz$$

is clearly equal to its Hermitian conjugate.

In the presence of the ENZ transition, the function $1/\epsilon(z)$, while being still pure real, features a singularity, so that in the expression

$$(4.25) \qquad \eta(p) \;=\; \frac{1}{2\pi} \int\limits_{-\infty}^{+\infty} \frac{e^{-ipz}}{\epsilon(z)} dz$$

the integration path must be curved to avoid this pole (see Fig. 4.3). Therefore, the Fourier transform of the inverse dielectric function (4.25) can be rewritten as

$$(4.26) \qquad \eta(p) \;=\; \frac{1}{2\pi} \fint\limits_{-\infty}^{+\infty} \frac{e^{-ipz}}{\epsilon(z)} dz - \frac{i}{2} \operatorname*{res}_{z=z_0} \frac{e^{-ipz}}{\epsilon(z)},$$

where the integral is understood as its Cauchy principal value. The second term that appears due to the singularity clearly breaks the hermiticity of the kernel in (4.23), and the non-Hermitian eigenvalue problem thus results in complex eigenvalues $\omega = \omega(k) = \omega'(k) - i\omega''(k)$.

The imaginary part of the eigenvalue $\omega$ means that the SPP would inevitably lose energy even if the metal is lossless. The very existence of the critical point in the ENZ

transition layer results in the delocalization of the plasmon energy, which therefore gradually radiates away from the interface and depletes the plasmon. This novel mechanism of the SPP decay is in some sense similar to the Landau damping mechanism [54], since neither is due to the electron collisions in metal, and the difference is that the SPP does not channel energy to the resonant electrons, but rather couples to the bulk plasmons in the transition layer [6].

This radiative plasmonic decay was earlier reported to exist for some specially tailored dielectric permittivity profiles in a two-layered system (see, e.g., [6]), however, the goal of my work is to develop a theoretical approach that is capable of calculating the SPP dispersion for *any* function $\epsilon(z)$ and, specifically, for systems with *any* number of layers, and that can also be generalized for 2D or 3D problems.

### 4.6.2. Linear Perturbation

Let us now seek the solution of the integral eigenvalue problem (4.23) in the linear order of the perturbation theory in the form of

$$(4.27) \qquad \omega \;=\; \omega(k) \;=\; \omega_0(k) + \Delta\omega(k),$$

$$(4.28) \qquad \eta(p) \;=\; \eta_0(p) + \Delta\eta(p),$$

$$(4.29) \qquad h(p) \;=\; h_0(p) + \Delta h(p),$$

where $\omega_0(k)$, $\eta_0(p)$ and $h_0(p)$ describe the spectrum, the dielectric permittivity and the magnetic field of the SPP in the unperturbed case, and the corrections $\Delta\omega(k)$, $\Delta\eta(p)$ and $\Delta h(p)$ are proportional to the small parameter $\delta$.

Substituting (4.27)-(4.29) into (4.23) and discarding quadratic over $\delta$ terms, one arrives at the Fredholm integral equation of the second kind for $\Delta h(p)$:

$$(4.30) \qquad \frac{\omega_0^2}{c^2}\Delta h\,(p) - \int\limits_{-\infty}^{+\infty} \left(k^2 + pp'\right)\eta_0(p-p')\Delta h(p')dp' \;=\; -\frac{2\omega_0\Delta\omega}{c^2}h_0\,(p) + F(p),$$

where the last term in the right-hand side is

(4.31)
$$F(p) = \int\limits_{-\infty}^{+\infty} \left(k^2 + pp'\right) \Delta\eta(p - p')h_0(p')dp'.$$

According to one of the Fredholm's theorems [27], the solution of the inhomogeneous Fredholm equation (4.30) exists if and only if the inhomogeneous term is orthogonal to the solution of the adjoint homogeneous equation, i.e., if

(4.32)
$$\int\limits_{-\infty}^{+\infty} \left(-\frac{2\omega_0\Delta\omega}{c^2}h_0\left(p\right) + F(p)\right) h_0^*(p)dp = 0,$$

where the solution of the homogeneous equation is nothing else but the unperturbed magnetic field $h_0(p)$. This orthogonality condition immediately gives the spectrum correction $\Delta\omega$:

(4.33)
$$\frac{\Delta\omega}{\omega_0} = \frac{c^2}{2\omega_0^2} \frac{\int\limits_{-\infty}^{+\infty} F(p)h_0^*(p)dp}{\int\limits_{-\infty}^{+\infty} h_0(p)h_0^*(p)dp}.$$

The denominator can be further simplified using the relation (4.21):

(4.34)
$$\int\limits_{-\infty}^{+\infty} h_0(p)h_0^*(p)dp = \frac{1}{2\pi} \int\limits_{-\infty}^{+\infty} H_0(z)H_0^*(z)dz = \frac{1}{2\pi} \int\limits_{-\infty}^{+\infty} |H_0(z)|^2 \, dz,$$

which yields

(4.35)
$$\frac{\Delta\omega}{\omega_0} = \frac{\pi c^2}{\omega_0^2} \frac{\int\limits_{-\infty}^{+\infty} F(p)h_0^*(p)dp}{\int\limits_{-\infty}^{+\infty} |H_0(z)|^2 \, dz}.$$

In order to evaluate the numerator, I rewrite the expression for $F(p)$ as

$$
\begin{aligned}
F(p) &= \int_{-\infty}^{+\infty} dp'(k^2 + pp')\Delta\eta(p - p')h_0(p') = \\[2mm]
&= \frac{1}{2\pi} \int_{-\infty}^{+\infty} dp'(k^2 + pp')h_0(p') \left( \int_{-\infty}^{+\infty} dz\, e^{-i(p-p')z} \left( \frac{1}{\epsilon(z)} - \frac{1}{\epsilon_0(z)} \right) \right) = \\[2mm]
&= \frac{1}{2\pi} \int_{-\infty}^{+\infty} dz \left( \frac{1}{\epsilon(z)} - \frac{1}{\epsilon_0(z)} \right) e^{-ipz} \left( \int_{-\infty}^{+\infty} dp'(k^2 + pp')h_0(p')e^{ip'z} \right) = \\[2mm]
&,= \frac{1}{2\pi} \int_{-\infty}^{+\infty} dz \left( \frac{1}{\epsilon(z)} - \frac{1}{\epsilon_0(z)} \right) e^{-ipz} \mathcal{F}(z, p),
\end{aligned}
$$

(4.36)

where the order of integrations was changed to allow for the calculation of the inner integral over $p$. Using the identities for the Dirac delta function (E.3)-(E.6), this inner integral, $\mathcal{F}(z, p)$, is significantly simplified:

$$
\begin{aligned}
\text{(4.37)} \quad \mathcal{F}(z, p) &= \int_{-\infty}^{+\infty} dp'(k^2 + pp')h_0(p')e^{ip'z} = \\[2mm]
&= \int_{-\infty}^{+\infty} dp'(k^2 + pp')e^{ip'z} \left( \frac{1}{2\pi} \int_{-\infty}^{+\infty} dz'\, H_0(z')e^{-ip'z'} \right) = \\[2mm]
&= \frac{1}{2\pi} \int_{-\infty}^{+\infty} dz'\, H_0(z') \left( \int_{-\infty}^{+\infty} dp'(k^2 + pp')e^{ip'(z-z')} \right) = \\[2mm]
&= \int_{-\infty}^{+\infty} dz'\, H_0(z')\left( k^2\delta(z - z') + ip\delta'(z - z') \right) = k^2 H_0(z) - ipH_0'(z),
\end{aligned}
$$

Consequently, the numerator of (4.35) is reduced to

$$
\int\limits_{-\infty}^{+\infty} F(p)h_0^*(p)dp = \frac{1}{2\pi} \int\limits_{-\infty}^{+\infty} dp\, h_0^*(p) \left( \int\limits_{-\infty}^{+\infty} dz \left( \frac{1}{\epsilon(z)} - \frac{1}{\epsilon_0(z)} \right) e^{-ipz} \mathcal{F}(z,p) \right) =
$$

(4.38)
$$
= \frac{1}{2\pi} \int\limits_{-\infty}^{+\infty} dz \left( \frac{1}{\epsilon(z)} - \frac{1}{\epsilon_0(z)} \right) \left( \int\limits_{-\infty}^{+\infty} dp\, \mathcal{F}(z,p)h_0^*(p)e^{-ipz} \right) =
$$

$$
= \frac{1}{2\pi} \int\limits_{-\infty}^{+\infty} dz \left( \frac{1}{\epsilon(z)} - \frac{1}{\epsilon_0(z)} \right) G(z),
$$

with the function $G(z)$ being

(4.39) $\quad G(z) = \int\limits_{-\infty}^{+\infty} dp\, \mathcal{F}(z,p)h_0^*(p)e^{-ipz} =$

$$
= \int\limits_{-\infty}^{+\infty} dp \left( k^2 H_0(z) - ipH_0'(z) \right) e^{-ipz} \left( \frac{1}{2\pi} \int\limits_{-\infty}^{+\infty} dz'\, H_0^*(z')e^{ipz'} \right) =
$$

$$
= \frac{1}{2\pi} \int\limits_{-\infty}^{+\infty} dz'\, H_0^*(z') \left( k^2 H_0(z) \int\limits_{-\infty}^{+\infty} dp\, e^{ip(z-z')} - iH_0'(z) \int\limits_{-\infty}^{+\infty} dp\, p\, e^{ip(z-z')} \right) =
$$

$$
= \int\limits_{-\infty}^{+\infty} dz'\, H_0^*(z') \left( k^2 H_0(z)\delta(z-z') - H_0'(z)\delta'(z-z') \right) = k^2|H_0(z)|^2 + |H_0'(z)|^2,
$$

Ultimately, the eigenfrequency shift $\Delta\omega$ takes the form which explicitly depends on the magnetic field $H_0(z)$ and the dielectric permittivities $\epsilon_0(z)$ and $\epsilon(z)$ only:

(4.40)
$$
\frac{\Delta\omega}{\omega_0} = \frac{c^2}{2\omega_0^2} \frac{\int\limits_{-\infty}^{+\infty} \left( \frac{1}{\epsilon(z)} - \frac{1}{\epsilon_0(z)} \right) \left( k^2|H_0(z)|^2 + |H_0'(z)|^2 \right) dz}{\int\limits_{-\infty}^{+\infty} |H_0(z)|^2 dz}.
$$

4.6.3. Analysis of the Eigenfrequency Shift

Every term in the right-hand side of (4.40) is pure real, yet the integration in the numerator results in a complex value since one has to carefully handle the singularities in $\frac{1}{\epsilon(z)}$, which are located at the points where $\epsilon(z) = 0$. The integration path must therefore be bent into the complex $z$ plane in order to avoid the poles $z_\sigma$, $\sigma = 1, 2, 3, ...$, distributed along

100
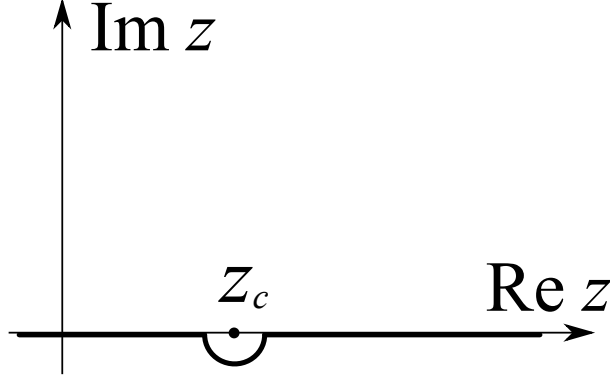
FIGURE 4.3. Integration path is curved into the lower semispace to avoid the pole $z_c$ on the real axis.

the real axis. Curving the integration path in the vicinity of the poles adds a small imaginary part to the function $\epsilon(z)$, and in order to perform the integration I make use of the following well-known identity from the complex analysis:

$$(4.41) \qquad \frac{1}{z - z_\sigma \pm i0^+} = P\frac{1}{z - z_\sigma} \mp i\pi\delta(z - z_\sigma),$$

which is a shorthand notation for

$$(4.42) \qquad \lim_{\alpha \to 0^+} \int_{-\infty}^{+\infty} \frac{f(z)}{z - z_\sigma \pm i\alpha}dz = \fint_{-\infty}^{+\infty} \frac{f(z)}{z - z_\sigma}dz \mp i\pi f(z_\sigma)$$

that is valid for an analytic function $f(z)$. The integral expression in the right is understood as its Cauchy principal value. The choice of the sign of the imaginary part for each $z_\sigma$ is determined by whether the pole must be circumflexed in the upper or lower semispace of the complex plane $z$ (see Fig. 4.3).

In general, the pole is integrated around in a way that is consistent with the causality, i.e., its contribution to $\Delta\omega$ must have negative imaginary part to guarantee that the SPP amplitude would not be exponentially increasing with time.

With that, one can separate the real part of $\Delta\omega$:

$$(4.43) \qquad \frac{\Delta\omega'}{\omega_0} = \frac{\mathrm{Re}\,\Delta\omega}{\omega_0} = \frac{c^2}{2\omega_0^2}\frac{\fint_{-\infty}^{+\infty}\left(\frac{1}{\epsilon(z)} - \frac{1}{\epsilon_0(z)}\right)\left(k^2|H_0(z)|^2 + |H_0'(z)|^2\right)dz}{\int_{-\infty}^{+\infty}|H_0(z)|^2dz},$$

101

from its imaginary part:

$$(4.44) \qquad \frac{\Delta\omega''}{\omega_0} = -\frac{\mathrm{Im}\ \Delta\omega}{\omega_0} = \frac{\pi c^2}{2\omega_0^2} \frac{\sum_\sigma |\epsilon'(z_\sigma)|^{-1} \left( k^2 |H_0(z_\sigma)|^2 + |H_0'(z_\sigma)|^2 \right)}{\int\limits_{-\infty}^{+\infty} |H_0(z)|^2 dz}.$$

Here I assumed the linear behavior of the dielectric function $\epsilon(z)$ in the vicinity of each critical point: $\epsilon(z) \approx \epsilon'(z_\sigma)(z - z_\sigma)$, so that the function $f(z)$ from the identity (4.42) corresponds to $\epsilon'(z)^{-1}(k^2|H_0(z)|^2 + |H_0'(z)|^2)$. The integration path bends into the lower semispace of the complex plane $z$ for the poles where $\epsilon'(z_\sigma) > 0$, and into the upper semispace otherwise.

In addition, I emphasize that the pure real nature of the functions $\epsilon(z)$ and $\epsilon_0(z)$ was only used to simplify the numerator in (4.40), which means the expression for the spectrum correction (4.40) is valid even if the dielectric functions are initially assumed to be complex, i.e., if they originally included the dissipation losses as their imaginary parts.

Also, since I did not assume any particular dependence of the dielectric function on the coordinate $z$, except its linear behavior close to the critical points, the result of (4.43) can formally take values of any sign. This raises the question of how to limit our consideration to only those choices for $\epsilon(z)$ that are realistic and physically meaningful. One way to do that is to obtain the plasmonic spectrum experimentally and extract the information about the sign of $\Delta\omega'$. Knowing the sign of the left hand side of (4.43), one will know the sign of the integral $\int\limits_{-\infty}^{+\infty} \left( \frac{1}{\epsilon(z)} - \frac{1}{\epsilon_0(z)} \right) \left( k^2|H_0(z)|^2 + |H_0'(z)|^2 \right) dz$ as well and thus can make an educated guess about the behavior of the dielectric function $\epsilon(z)$.

Finally, I note that in some situations it is more convenient to describe exactly the same behavior of the SPP by the pure real frequency $\omega$ and the complex wavevector $k = k(\omega) = k'(\omega) + ik''(\omega)$. With respect to the perturbation theory, the connection between the two approaches can be established for small corrections $\Delta\omega$ and $\Delta k$ in the form of

$$(4.45) \qquad \Delta\omega' = -\left| \frac{d\omega}{dk} \right| \Delta k', \qquad \Delta\omega'' = \left| \frac{d\omega}{dk} \right| \Delta k'',$$

via the group velocity $d\omega/dk$ of the unperturbed SPP mode. Alternatively, one can explicitly use a similar perturbative approach to calculate $\Delta k$ from (4.23).

102

4.7. SPP Dispersion

Validating the theoretical predictions requires performing a number of numerical simulations. In every simulation, I model the continuous metal-dielectric transitions with the dielectric function

(4.46) $$\epsilon(z) \;=\; \epsilon_d + \frac{\epsilon_m - \epsilon_d}{1 + e^{z/\delta}},$$

where the parameter $\delta$ defines the transition layer thickness (see Fig. 4.1).

Here I compare the predictions of the perturbation theory with the SPP dispersion corrections calculated numerically. In order to do that, I numerically find the eigenvalues $\omega$ of the wave equation (4.4) for given wavevector $k$ and permittivity $\epsilon(z)$ as follows. The eigenvalue $\omega$ is initially set equal to that of the unperturbed spectrum: $\omega = \omega_0(k)$. The wave equation is then independently solved in the two regions, $z > 0$ and $z < 0$, with the specified asymptotic behavior imposed towards both infinities according to $|H(z)| \xrightarrow[z \to \pm\infty]{} 0$. The two solutions are renormalized to satisfy the magnetic field continuity $H(0^+) = H(0^-)$, and the value of the goal function $|E_x(0^+) - E_x(0^-)|$ is computed. If the obtained value is lower than some set threshold, the longitudinal electric field $E_x(z)$ is considered to be continuous as well and the eigenvalue $\omega$ is thus found; otherwise, the optimization procedure is run to minimize the goal function, sweeping over the region of complex $\omega$.

I calculated the SPP dispersion for the cases of bulk and 50nm-thick silver slabs surrounded by air (see Fig. 4.4). For the dielectric permittivity of silver, I used the experimental data from [47] that was fit by the generalized Lorentz-Drude model as described in [76] (see Appendix F for details). Here $\delta = 0.02$ nm, so that the thickness of the ENZ layer is on the order of 1 Å.

In both cases, there were no drastic changes to the real part of the SPP dispersion due to including the ENZ transition layer into consideration, as seen from the main panels in Fig. 4.4. Instead, of particular interest are the results shown in the insets, where the imaginary part of $\omega$ is plotted in terms of the SPP propagation length. The propagation length $L$ measures the distance over which the plasmon energy decreases by a factor of $e$
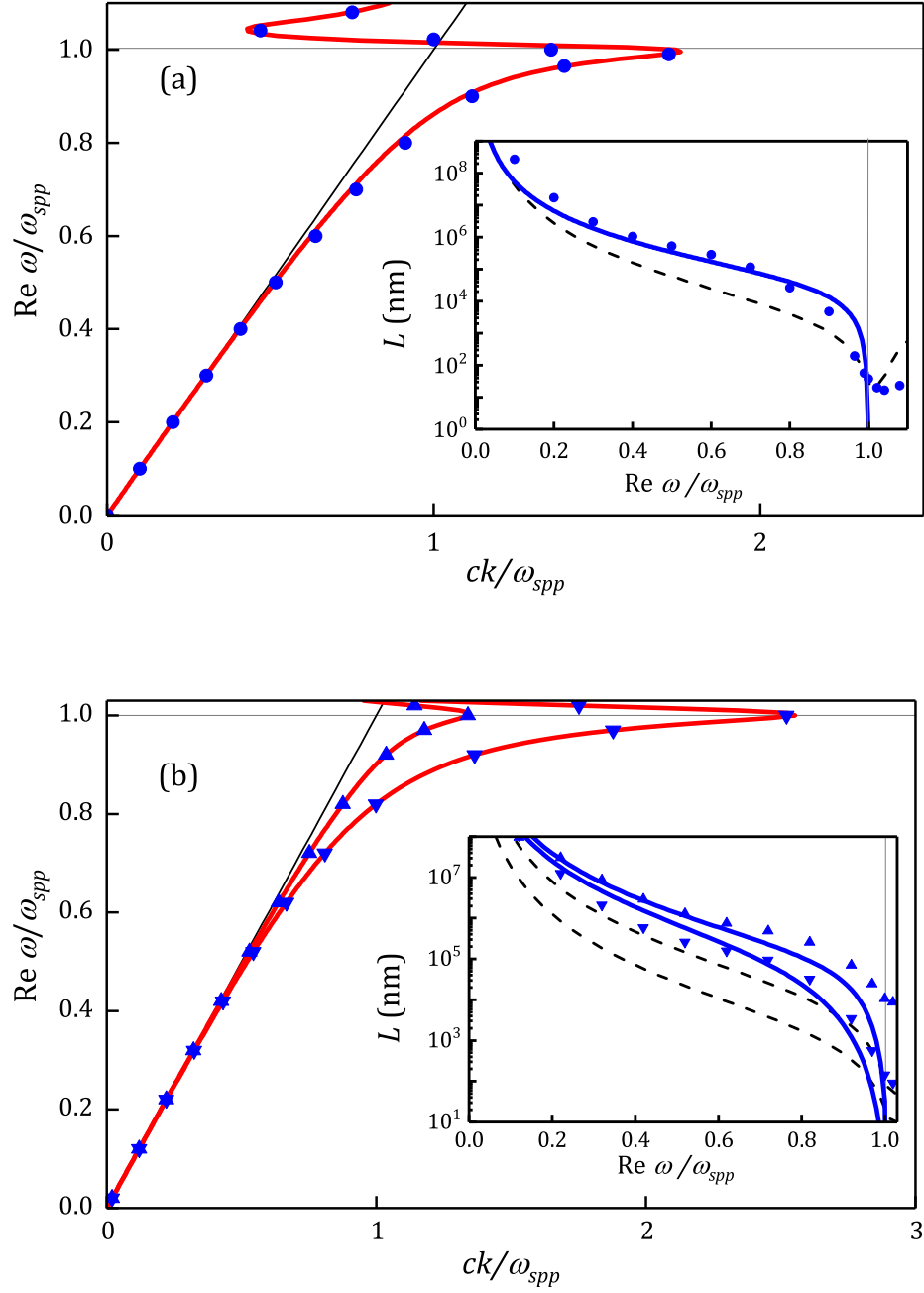
FIGURE 4.4. SPP dispersion for the bulk (a) and 50nm-thick (b) silver slabs in air. The red curves and blue data points show the dispersion for the cases of ideal and realistic (with $\delta = 0.02$nm) interfaces, respectively. The insets compare theoretical (blue lines) and numerical (blue data points) results for the SPP collisionless damping rates, expressed in terms of propagation length. The rate of Joule losses is shown with dashed black lines.

and can be expressed in terms of $\omega''$ as $L = (2\omega'')^{-1}|d\omega/dk|$.

For the bulk sample, there is a good agreement between the theoretical and numerical estimations of the SPP decay rate that is only due to the SPP radiation through the critical point where $\epsilon(z) = 0$. When approaching the plasmon resonance frequency, the perturbation theory predicts much faster decay than the numerical calculation. This happens because at high frequencies, one may no longer assume the perturbation to be small (the condition $k\delta \ll 1$ is not valid anymore), and the perturbation theory is no longer applicable.

For the thin film sample, there is also a good agreement for the high-frequency SPP mode, while the solution for the low-frequency SPP mode either under- or overestimates the numerically simulated propagation length, which is probably due to the perturbation theory exceeding its validity region.

For the reference, both insets also display the SPP propagation length that is only due to the Joule losses in metal in the Drude model. This dissipative decay rate grows with frequency considerably slower than the decay rate due to the SPP radiative losses, and above the certain frequency the radiative decay becomes the dominant channel for energy dissipation.

4.8. Excitation of SPP in the Transition Layer

4.8.1. Experimental Motivation

The two other simulations that were performed using the finite-element method modeled the excitation of the SPP by light. In experiment such scenario is typically realized in either Otto or Kretschmann configuration [75], where a laser beam propagates through a glass prism and is incident at an angle on a plasmonic sample. The material of the prism must be more optically dense than the dielectric of the sample, which is a necessary condition that allows matching between the SPP wavevector and the parallel to the sample component of the wavevector of the laser. In the absence of the prism the SPP excitation would never occur as the SPP wavevector $k_{SPP} > \omega/c$ would always be larger than the wavevector of light $k = \omega/c$. The latter expresses the fact that SPPs propagate with the phase speed that is lower than the speed of light in corresponding dielectric medium.

105
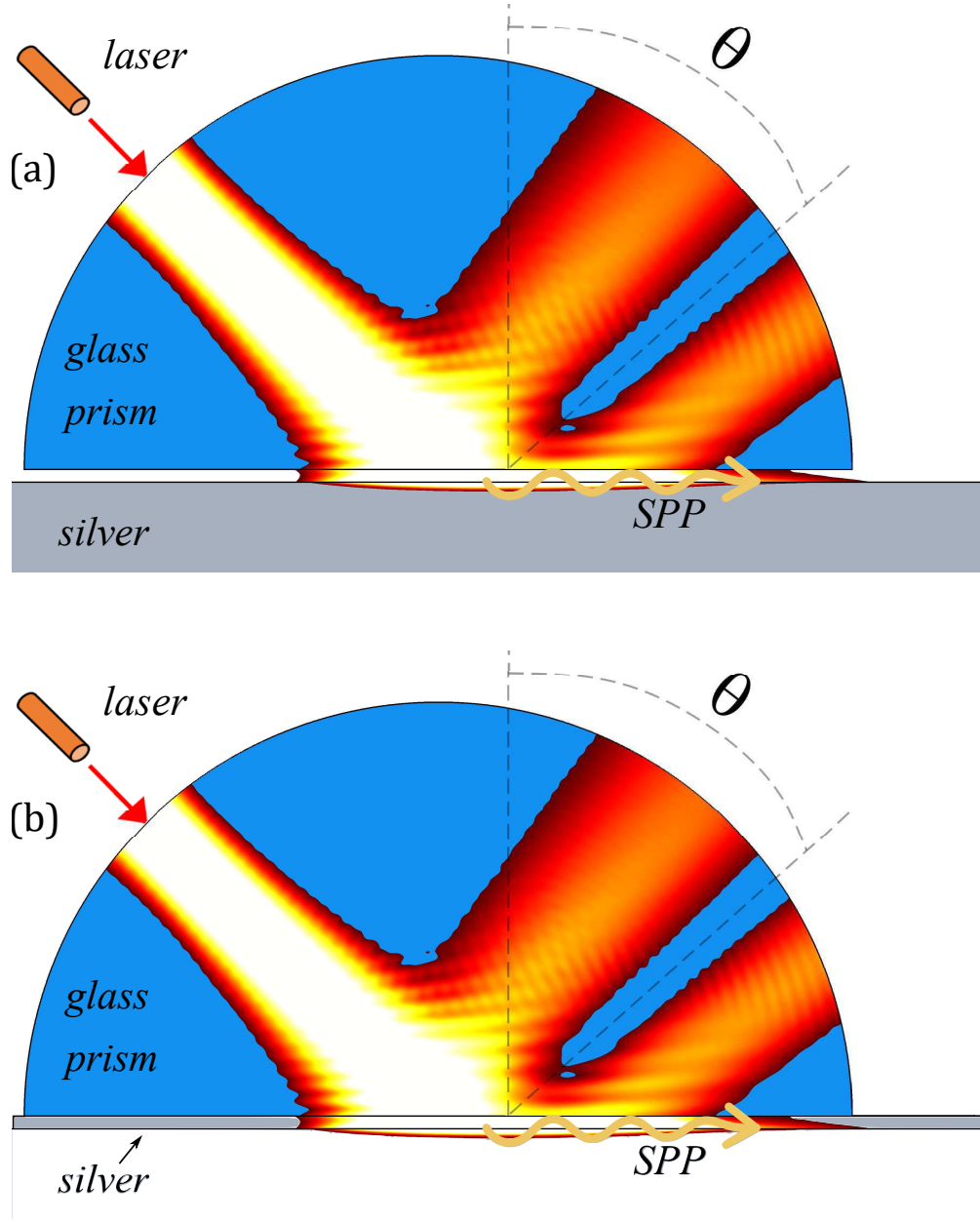
FIGURE 4.5. Excitation of the SPP (a) on the silver slab in Otto configuration and (b) on the thin film in Kretschmann configuration [75].

Fig. 4.5(a) shows the excitation of SPP in the Otto configuration, which differs from the Kretschmann configuration on Fig. 4.5(b) only in the position of the prism. Namely, in the Kretschmann configuration the prism sits on top of the metallic part of the plasmonic sample and the SPP is excited on the interface inside the sample, whereas in the Otto

configuration the prism is separated from the sample by the air (or other dielectric) gap which leads to the SPP excitation along the interface between the air and the sample. In the latter case the SPP may also be excited on the other interface of metal, provided the sample is relatively thin. If it were thick, though, no excitation would reach that other interface due to the exponential weakening of the electromagnetic field as it propagates across the metallic layer.

Now, since one must also incorporate into setup the ability to control the width of the transition layer on the metal-dielectric interface by applying external DC field, the real sample would actually be a multi-layered structure. Besides the possible dielectric substrate and index-matching layers, there have to be two outer layers serving as electrodes. Such layers must be transparent for light, but still be able to conduct electricity. Even though it is possible to find material that satisfies both these requirements (indium tin oxide, or ITO), one would need to carefully select the laser wavelength for the experiment in order to minimize losses in the auxiliary layers without getting too far from the SPP resonance.

It is for certain, however, that for the experiment with the bulk (thick) metallic sample only the Otto configuration is viable. On the contrary, exciting SPPs on a thin metallic film benefits from the Kretschmann configuration as it becomes possible to negate the unavoidable issues with the uneven contact between the prism and the sample due to the surface roughness, e.g., by submerging the sample in the index matching liquid.

4.8.2. Models for FEM Numerical Simulation

For the purpose of comparing the theoretical results (4.43) and (4.44) derived earlier with the possible outcome from the envisioned experiment, I simulate the SPP excitation on the air-silver interface using the following two models.

In the first model, the SPP is excited on top of the bulk silver slab in Otto configuration (see Fig. 4.5(a)). In this setup, the laser light is illuminating the hemicylindrical glass prism and is totally internally reflected from the glass-air interface. However, the evanescent electromagnetic field is still able to reach across the thin (125nm) air gap and excite the plasmon on the metal surface. In the second model, the bulk silver slab is replaced with

107

a thin silver film and the air gap is removed (Kretschmann configuration, see Fig. 4.5(b)), allowing the excitation of the plasmonic mode at the air-silver interface.

The laser wavelength is $\lambda = 370$nm, which is chosen to be close to the SPP resonance. I define the resonant frequency $\omega_{spp}$ by the condition $\text{Re } \epsilon_m(\omega_{spp}) + \epsilon_d = 0$, which makes $\omega_{spp}$ correspond to the wavelength of approximately 331nm. The actual plasmonic resonance is observed at a slightly lower frequency due to the dissipation in metal. The refractive index of the prism is set to $n = 1.75$ (a sapphire prism).

### 4.8.3. Simulation Results

In order to excite the SPP on the air-silver interface, the plasmon wavevector $k = k(\omega)$ must match the parallel to the interface component of the wavevector of the laser light: $k(\omega) = n\omega/c\sin\theta$. When this condition is satisfied, there will be a minimum in reflection at exactly the direction given by angle $\theta$ (see Fig. 4.5). For the chosen parameters, the minimum in reflection in the case with bulk sample is observed for $\theta = 46.0°$, and in the case of the 50nm-thick film the minimum is at $\theta = 40.0°$ and $\theta = 55.6°$ indicating the excitation of the plasmonic mode at the lower (air-silver) interface.

With that, I impose the continuous dielectric permittivity (4.46) on the air-silver interfaces and detect how the minimum in reflection shifts its angular position and how the plasmon propagation length changes when varying the parameter $\delta$.

Fig. 4.6 shows the results obtained for both samples. The minimum in reflection was identified by the angle $\theta$ at which the intensity of the reflected laser light along the circular surface of the prism is the lowest. As for the propagation length, its evaluation requires extracting the dependence of the SPP intensity on the coordinate along the interface. The logarithm of the intensity is expected to decay linearly with the distance, which follows from the relation $I(x) = I_0 e^{-2x/L}$. Then, if one fits a linear function to such data and finds its slope, the propagation length is calculated as $L = -2/\text{slope}$.

The data points from the numerical simulation indicate that the SPP propagation length is significantly reduced when increasing $\delta$, and the minimum in reflection shifts towards the larger angles $\theta$ which means the SPP dispersion shifts towards higher wavevectors
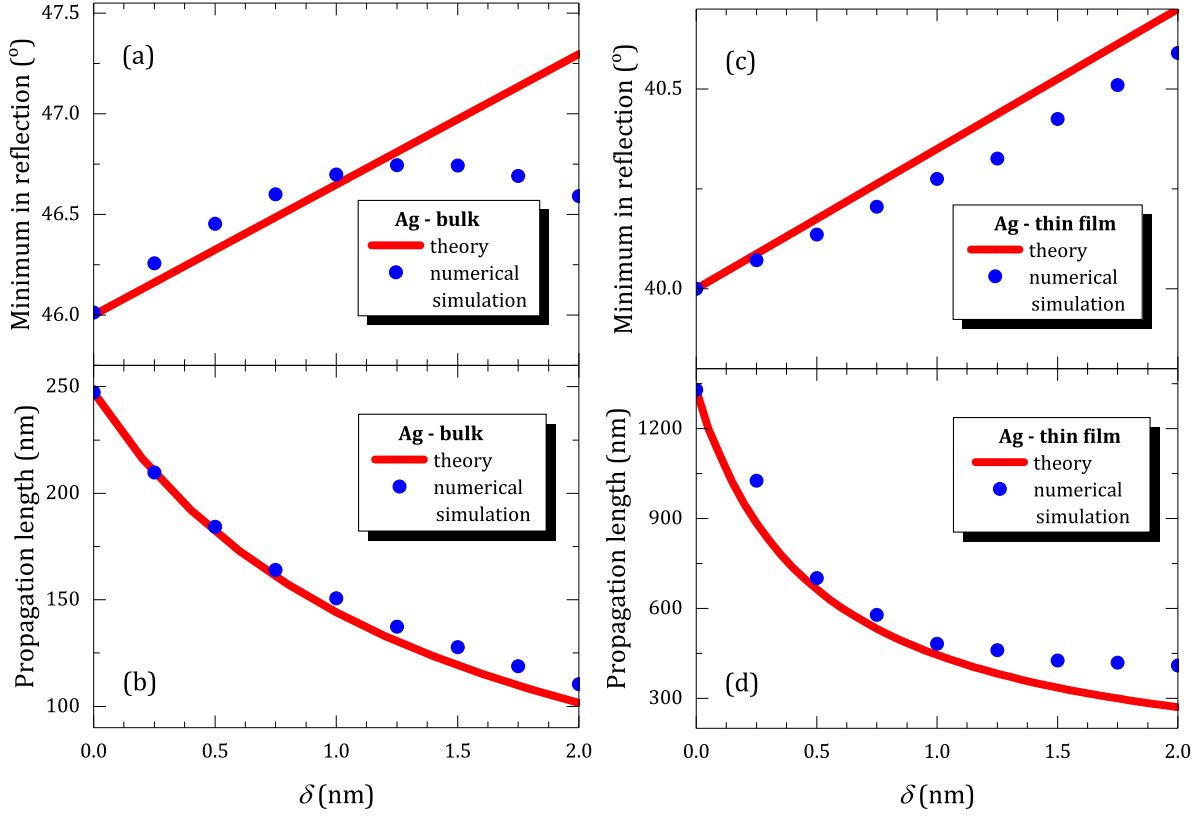
FIGURE 4.6. Angular positions of the reflected intensity minimum (a,c) and propagation lengths (b,d) for the SPP on the bulk (left panels) and 50nm-thick (right panels) silver slabs as a function of $\delta$. Red curves represent the theoretically calculated dependence and blue data points correspond to the numerical simulations. The results for the ideal interface are included as the data at $\delta = 0$.

$k$ for a given frequency $\omega$. The same can alternatively be thought of as a red-shift of the SPP eigenfrequencies $\omega$ for a given wavevector $k$. The theoretical results for the propagation length $L = (2\omega'')^{-1}|d\omega/dk|$ shown in Fig. 4.6 are calculated based on (4.44), while the resonant excitation condition $k(\omega) = n\omega/c\sin\theta$ together with (4.45) gives the angular shift $\Delta\theta = \Delta k'/k\tan\theta = -\Delta\omega'/k|d\omega/dk|\tan\theta$.

The theoretical calculations demonstrate good agreement with the numerical data, except for $\delta > 1$nm, when the numerically simulated angular position of the minimum

actually starts decreasing and the perturbation theory results become invalid. The reason for it is the strong modification of the SPP spectrum for large $\delta$. Namely, increasing the SPP damping always implies a reduction of the wavevector of the plasmon at the resonant frequency $\omega_{spp}$, and because of the significant SPP damping due to radiation losses the SPP excitation indeed occurs for smaller incident angle $\theta$.

Another factor to mention is the influence of the prism, which explicitly allows the SPP to leak out through itself and therefore introduces more modifications to the SPP spectrum which are unaccounted for by the perturbation theory. In the real experiment, there may also arise additional issues with the sample heating during the SPP excitation, the possible dielectric breakthrough and the charge leakage under influence of the applied DC electric field.

## 4.9. Summary

This chapter comprises of the comprehensive theoretical and numerical studies of the SPP propagation in layered systems along the interfaces featuring epsilon-near-zero transition regions. I developed the novel integral approach to the SPP eigenvalue problem, which is then applied to calculate the linear correction to the SPP spectrum. The obtained correction describes the spectrum difference with respect to the setting with "ideal" interfaces, i.e., where the transition layer is regarded as infinitesimally thin. I demonstrated that this correction is essentially complex, which means that even in a lossless environment the plasmon acquires a nonzero dissipation rate. In other words, the critical point within the epsilon-near-zero region opens a new energy decay channel for the SPP. This decay is due to neither the electron collisions in metal nor the metal surface roughness, as these factors were intentionally eliminated from the system. However, the SPP now has the possibility to excite the bulk plasmons via the critical point. The SPP thus eventually radiates its energy away from the interface, and adjusting the transition layer width presents a new means of manipulating the SPP resonant frequency as well as its propagation length. The obtained general expression for the spectrum correction is valid for the arbitrary dielectric function profile, and the proposed analytical approach may easily be extended to address

more complicated geometries, in particular, cylindrical or spherical layered structures.

I also numerically simulated the SPP propagation and excitation on top of the two silver samples — bulk metal and thin film, — and computed the changes to the plasmonic dispersion caused by the smooth transition of the dielectric function between the media. The theoretical predictions agree well with the numerical simulation for frequencies which are not too close to the SPP resonance.

These findings are of particular importance for designing the plasmonic-based optical devices which employ SPPs for the photon emission enhancement and for near-field imaging applications.

CHAPTER 5

RESULTS AND CONCLUSIONS

In this dissertation I investigated the implications of the physical processes occurring at the interfaces between media in three different acoustic and electrodynamic systems. There are two keystones that allow a comprehensive study of each system and provide insights to the nature of phenomena occurring in them. The first one is the analysis of the band structure together with the dispersion relation of the systems, and the other one is the calculation of the transmission properties that requires solving the inhomogeneous problem.

For the two acoustic systems — the fluid channel between two solid plates and the periodic chain of perforated metallic cylindrical shells — I analytically obtained their transmission spectra and explained the reasons for anomalously suppressed transmission at certain frequencies, which was experimentally observed previously. I also demonstrated how these systems can serve as passive antennas, redirecting or splitting the incident acoustic signal. The latter nontrivial effects are enabled by the surface modes excited at the interfaces in the systems: coupled Rayleigh waves in one case and quasi-surface waves confined along the chain in another case.

For the metal-dielectric slab having a realistic interface (essentially being an ENZ transition layer) I theoretically derived how the spectrum of the surface plasmon propagating along such interface is altered by the presence of the transition layer and discovered a new nonradiative mechanism of plasmonic decay which the plasmon thus unavoidably acquires. The numerical simulations that I performed visualized the excitation of the surface plasmon inside the ENZ layer between the metal and the dielectric when the layer thickness was controlled by an external electrostatic field. The results obtained from the simulations agreed with the theoretical analysis and helped understand how the effect can be observed experimentally.

An interesting question to discuss is whether the material properties and system

geometries can be optimized in order to achieve stronger manifestation of the described phenomena. I conclude that in each case one should run a corresponding optimization procedure to find the optimal values instead of simply pushing the material properties to their extremes. Namely, the fluid-channel system is able to redirect sound through the Rayleigh waves, the existence of which relies on the coupling between the fluid and the solid plates. If the density and stiffness of the solid are significantly increased, the plates become rigid and no propagation of Rayleigh waves is possible. In the other extreme case, when the impedance of the solid $\rho c$ is reduced to as low as the impedance of fluid, the whole system becomes virtually transparent for incoming sound, which does not facilitate emerging of Rayleigh waves. The same goes for the linear chain of perforated shells: the sound is redirected via one of the eigenmodes which would be much more dissipative if the shells were thicker or with smaller perforations, or would cease to exist for ultrathin shells with large perforations. The splitting of sound by the chain also relies on the weakness of the scatterers, since a better frequency resolution is achieved when the band gap is narrower, but, again, the scatterers too weak would not split any noticeable amount of incoming sound. In both cases changes to other parameters of the geometry only lead to scaling of the device operating frequency regions. As for the surface plasmon problem, it is desirable to stretch the transition layer as much as possible (while not causing a dielectric breakdown) to get stronger modifications of the plasmonic spectrum, however, the accompanying nonradiative losses would grow as well, extinguishing the plasmon before it is even formed.

Overall, I exposed several physical phenomena which are of fundamental significance to physical acoustics and electrodynamics, although they also have immediate value to bring to the real-world applications by furnishing design ideas for acoustic waveguides and antennas and establishing the limits of the plasmonic-based devices.

APPENDIX A

CHOICE OF THE BRANCH CUT FOR THE COMPLEX-VALUED SQUARE ROOT

FUNCTION

Here I consider a general case of a wave of a form

(A.1)
$$u(x, y, z, t) = u_0 e^{ik_x x + ik_z z - i\omega t}$$

propagating in a homogeneous and isotropic medium in the semispace $z > 0$ bounded by an interface $z = 0$. Suppose the dispersion of the wave is parabolic,

(A.2)
$$k_x^2 + k_z^2 = \frac{\omega^2}{c_{ph}^2},$$

with $c_{ph}$ being the phase velocity of the wave.

Now, if the value of the $x$-component of the wave vector, $k_x$, is determined by the physical process developing in the medium, one can find the $z$-component of the wave vector to be

(A.3)
$$k_z = \sqrt{\frac{\omega^2}{c_{ph}^2} - k_x^2}.$$

If the value of $k_x$ is real and $k_x < \omega/c_{ph}$, the value of $k_z$ is then also real, and the wave (A.1) is a simple plane wave running in the direction of $\mathbf{k} = (k_x, 0, k_z)$. In the case of $k_x > \omega/c_{ph}$ the value of $k_y$ is purely imaginary, $k_z = i\sqrt{k_x^2 - \omega^2/c_{ph}^2} = i\kappa_z$, $\kappa_z > 0$, which is typical for guided modes that propagate along an interface in the $x$-direction and decay in the perpendicular direction into the medium:

$$u(x, y, z, t) = u_0 e^{ik_x x - \kappa_z z - i\omega t}.$$

There are, however, two other possible wave behaviors that are described by the complex-valued $k_x$ and therefore require special attention. First of all, the energy carried with the wave can only dissipate, which corresponds to Im $k_x > 0$, and the case of Im $k_x < 0$ does not have any physical sense. This implies that $k_x$ lies in the first quadrant of the complex plane, and therefore $k_z^2 = \omega^2/c_{ph}^2 - k_x^2$ is in either third or fourth quadrants. On the other hand, the relationship (A.2) dictates that the signs of the real and imaginary parts of $k_z$ be opposite (with $k_z$ in the second or fourth quadrants), otherwise it cannot be satisfied for any given purely real $\omega$ and complex $k_x$ with both Re $k_x > 0$ and Im $k_x > 0$.

115

For the positive values of Re $k_z^2$, i.e., when Re $\left(\omega^2/c_{ph}^2 - k_x^2\right) > 0$, the correct behavior of the wave is the radiative one, with Re $k_z > 0$, so the square root should map the values of $k_z^2$ from the fourth quadrant into the fourth quadrant. Note that Im $k_z > 0$ in this case, which formally means an exponential growth of the wave amplitude away from the interface. However, the amplitude decay along the $x$-axis "compensates" for the growth along the $z$-axis [37, 45, 55], and, in fact, it can be shown that such a wave propagates with a constant amplitude along the direction of $\mathbf{k}' = (\text{Re } k_x, 0, \text{Re } k_z)$. This is a clear manifestation of the radiative behavior since the energy of the wave is not being transmitted along the interface but is rather carried away at an angle from it.

For the negative values of Re $k_z^2$, the wave must be nonradiative [64, 65], with positive Im $k_z$ providing the exponential decay away from the interface, and the corresponding mapping for the square root function is from the third into the second quadrant.

One possibility to satisfy all the conditions outlined above is to define the complex-valued square root function with the branch cut along the negative imaginary axis. Alternatively, one can use the conventional square-root function (with the branch cut along the negative real axis) and, instead, explicitly specify the sign ("+" or "−") in front of the square root in (A.3) in each case.

APPENDIX B

CALCULATION OF FOURIER TRANSFORMS FOR PROPAGATING AND LEAKY

RAYLEIGH EIGENMODES

Consider the integral

(B.1)
$$\mathcal{F}(k, \varkappa) \;=\; \frac{e^{\varkappa d/2}}{2} \left( \int\limits_{-\infty}^{-d/2} e^{-ikz+\varkappa z} dz + \int\limits_{+d/2}^{+\infty} e^{-ikz-\varkappa z} dz \right)$$

which arises when the Fourier transforms of (2.84)-(2.85) are calculated. If the parameter $\varkappa$ describes the propagating Rayleigh eigenmode, i.e., if Re $\varkappa > 0$ and Im $\varkappa = 0$, the calculation of (B.1) is trivial:

(B.2)
$$\mathcal{F}(k, \varkappa) \;=\; \frac{e^{\varkappa d/2}}{2} \left( \int\limits_{-\infty}^{-d/2} e^{-ikz+\varkappa z} dz + \int\limits_{+d/2}^{+\infty} e^{-ikz-\varkappa z} dz \right) \;=$$

$$= \; \frac{e^{\varkappa d/2}}{2} \int\limits_{+d/2}^{+\infty} \left( e^{+ikz-\varkappa z} + e^{-ikz-\varkappa z} \right) dz \;=$$

$$= \; \frac{e^{\varkappa d/2}}{2} \left( \frac{e^{(ik-\varkappa)d/2}}{\varkappa - ik} + \frac{e^{(-ik-\varkappa)d/2}}{\varkappa + ik} \right) \;=$$

$$= \; \frac{1}{k^2 + \varkappa^2} \left( \varkappa \cos \frac{kd}{2} - k \sin \frac{kd}{2} \right).$$

However, for the leaky Rayleigh eigenmode with Re $\varkappa < 0$ and Im $\varkappa < 0$ the integral (B.1) diverges. Its value can be written as a limit

(B.3)
$$\mathcal{F}(k, \varkappa) \;=\; \frac{e^{\varkappa d/2}}{2} \left( \frac{e^{(ik-\varkappa)d/2}}{\varkappa - ik} + \frac{e^{(-ik-\varkappa)d/2}}{\varkappa + ik} \right) - \lim_{Z \to +\infty} \frac{e^{\varkappa d/2}}{2} \left( \frac{e^{(ik-\varkappa)Z/2}}{\varkappa - ik} + \frac{e^{(-ik-\varkappa)Z/2}}{\varkappa + ik} \right).$$

It was shown in [46] that the divergence can be avoided with the introduction of perfectly matched layers (PMLs) in the regions $|z| > L$, where $L$ is a characteristic distance beyond which the physical processes are of no interest. In the problem of sound transmission through a fluid channel between two elastic plates, $L$ could be the size of the actual plates in the direction away from the channel. Within the PML the signal undergoes fast attenuation, and the PML behavior is typically modeled by a complex coordinate transform. Namely, the integral in the original limits is split into two parts

(B.4)
$$\int\limits_{d/2}^{+\infty} f(z) dz \to \int\limits_{d/2}^{L} f(z) dz + \int\limits_{L}^{+\infty} f(z') g(z') dz',$$

where the attenuation in the PML is added by the factor $g(z')$, and the latter integral must be identical to the integral along the line in the complex plane $z$:

$$(\text{B.5}) \qquad \int\limits_{L}^{+\infty} f(z')g(z')dz' \equiv \int\limits_{L}^{L+(1+i\alpha)\infty} f(z)dz.$$

The integrands in (B.1) are analytical functions, so the contour integral

$$(\text{B.6}) \qquad \mathcal{F}(k,\varkappa) = \frac{e^{\varkappa d/2}}{2} \int\limits_{+d/2}^{L+(1+i\alpha)\infty} \left( e^{+ikz-\varkappa z} + e^{-ikz-\varkappa z} \right) dz$$

is evaluated to

$$(\text{B.7})$$
$$\mathcal{F}(k,\varkappa) = \frac{e^{\varkappa d/2}}{2} \left( \frac{e^{(ik-\varkappa)d/2}}{\varkappa - ik} + \frac{e^{(-ik-\varkappa)d/2}}{\varkappa + ik} \right) - \lim_{Z \to L+(1+i\alpha)\infty} \frac{e^{\varkappa d/2}}{2} \left( \frac{e^{(ik-\varkappa)Z/2}}{\varkappa - ik} + \frac{e^{(-ik-\varkappa)Z/2}}{\varkappa + ik} \right).$$

The value of $\alpha$, which characterizes the PML, must be chosen to guarantee the finite value of the limit in the latter expression.

For $k \geq 0$ and $\alpha > |\text{Re } \varkappa / \text{Im } \varkappa|$ the limit in (B.7) is zero and

$$(\text{B.8}) \qquad \mathcal{F}(k,\varkappa) = \frac{1}{k^2 + \varkappa^2} \left( \varkappa \cos \frac{kd}{2} - k \sin \frac{kd}{2} \right).$$

The final result is the same for negative values of $k$ as well, as the function $\mathcal{F}(k,\varkappa)$ is even with respect to its first argument.

APPENDIX C

GRAF'S ADDITION THEOREM
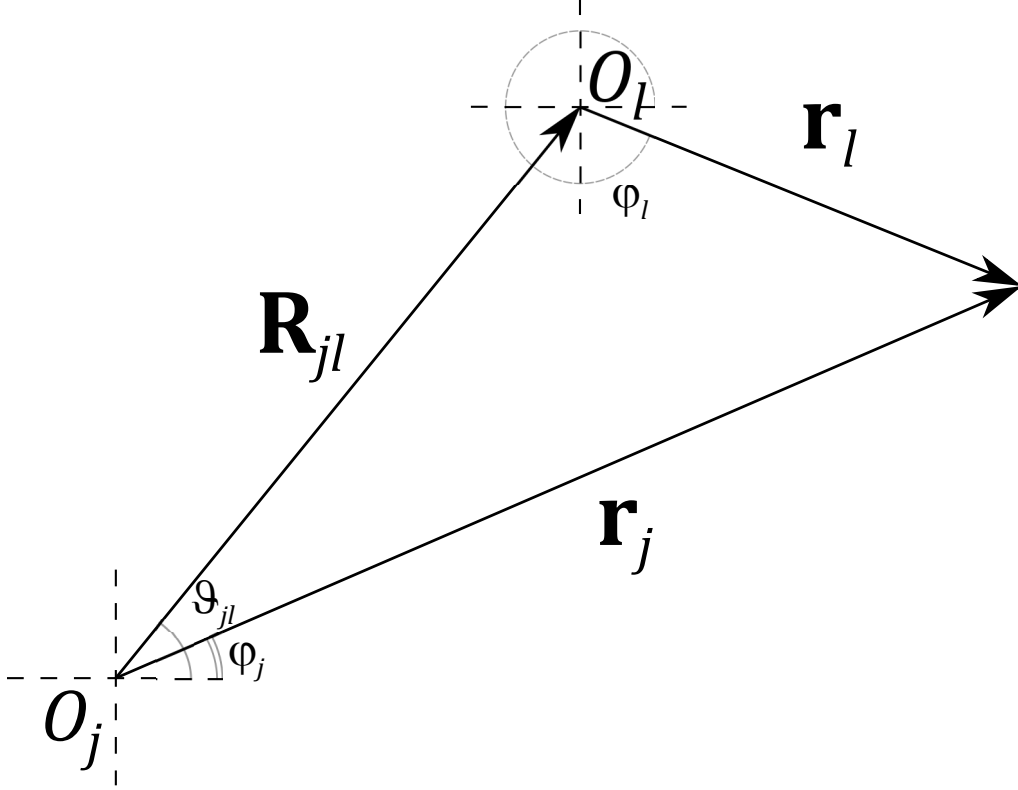
FIGURE C.1. The three vectors $\mathbf{r}_j$, $\mathbf{r}_l$, and $\mathbf{R}_{jl}$. The properties of these vectors can be related using Graf's theorem.

Let there be a triangle formed by the vectors $\mathbf{r}_j$, $\mathbf{r}_l$, and $\mathbf{R}_{jl} = \mathbf{r}_j - \mathbf{r}_l$ as shown in the Fig. C.1. Suppose that $\mathbf{r}_l$ has the coordinates $(r_l, \varphi_l)$ in the polar coordinate system with the origin in $O_l$, while $\mathbf{r}_j = (r_j, \varphi_j)$ and $\mathbf{R}_{jl} = (R_{jl}, \vartheta_{jl})$ in the polar coordinate system with the origin in $O_j$.

Then, according to [4], the addition rule exists for the Hankel functions of the first kind $H_n$, and it can be written down in the following form:

$$(C.1) \qquad H_n\left(kr_j\right) e^{in\left(\varphi_j - \vartheta_{jl}\right)} = \sum_{n'=-\infty}^{+\infty} H_{n+n'}\left(kR_{jl}\right) J_{n'}\left(kr_l\right) e^{in'\left(\pi - \varphi_l + \vartheta_{jl}\right)},$$

with the only restrictions that $j \neq l$ and $r_l < R_{jl}$ [1].

121

APPENDIX D

FAST CONVERGING SERIES FOR THE LATTICE SUM

The lattice sum (3.35)

$$F(n) = \sum_{l=1}^{+\infty} H_n\left(kld\right)\left(e^{iqld} + (-1)^n e^{-iqld}\right)$$

converges slowly because of the slow decay $|H_n(kld)| \propto 1/\sqrt{kld}$ of the Hankel functions for $l \gg 1$. Nevertheless, the calculation of this sum is possible since an equivalent but fast converging representation was found in [99]:

$$\text{(D.1)} \qquad F(0) = -1 - \frac{2i}{\pi}\left[\gamma + \ln\frac{k}{2p}\right] - \frac{2i\left(k^2 + 2q^2\right)}{p^3 d}\zeta(3)$$

$$- \frac{2i}{\gamma_0 d} - \frac{2i}{d}\sum_{m=1}^{+\infty}\left(\frac{1}{\gamma_m} + \frac{1}{\gamma_{-m}} - \frac{2}{mp} - \frac{k^2 + 2q^2}{m^3 p^3}\right),$$

$$\text{(D.2)} \qquad F(2n) = -\frac{2ie^{-2in\alpha_0}}{\gamma_0 d} + \frac{i}{n\pi} - \frac{2i(-1)^n}{\pi}\left(\frac{k}{2p}\right)^{2n}\zeta(2n+1)$$

$$- 2i\sum_{m=1}^{+\infty}\left(\frac{e^{-2in\alpha_m}}{\gamma_m d} + \frac{e^{2in\alpha_{-m}}}{\gamma_{-m}d} - \frac{(-1)^n}{m\pi}\left(\frac{k}{2mp}\right)^{2n}\right)$$

$$+ \frac{i}{\pi}\sum_{m=1}^{n}\frac{(-1)^m 2^{2m}(n+m-1)!}{(2m)!(n-m)!}\left(\frac{p}{k}\right)^{2m}\mathcal{B}_{2m}\left(\frac{q}{p}\right),$$

$$\text{(D.3)} \qquad F(2n-1) = \frac{2ie^{-i(2n-1)\alpha_0}}{\gamma_0 d} + \frac{2i(-1)^n qdn}{\pi^2}\left(\frac{k}{2p}\right)^{2n-1}\zeta(2n+1)$$

$$+ 2i\sum_{m=1}^{+\infty}\left(\frac{e^{-i(2n-1)\alpha_m}}{\gamma_m d} - \frac{e^{i(2n-1)\alpha_{-m}}}{\gamma_{-m}d} + \frac{i(-1)^n qdn}{m^2 \pi^2}\left(\frac{k}{2mp}\right)^{2n-1}\right)$$

$$- \frac{2}{\pi}\sum_{m=0}^{n-1}\frac{(-1)^m 2^{2m}(n+m-1)!}{(2m+1)!(n-m-1)!}\left(\frac{p}{k}\right)^{2m+1}\mathcal{B}_{2m+1}\left(\frac{q}{p}\right).$$

Here $\mathcal{B}_m$ is the Bernoulli polynomial, $\gamma = 0.577$ is Euler's constant and

$$\text{(D.4)} \qquad p = \frac{2\pi}{d}, \qquad q_m = q + mp, \qquad \gamma_m = -i\sqrt{k^2 - q_m^2}, \qquad \alpha_m = \arcsin\frac{q_m}{k}.$$

These representations are valid for $n > 0$ and for any complex $k$ with nonnegative imaginary part. Calculating the lattice sum for $n < 0$ is based on (D.2) and (D.3) and relies on the observation that $F_{-n} = (-1)^n F_n$.

When Im $k < 0$, the original series (3.35) exponentially diverges. Nevertheless, since the expressions (D.1)-(D.3) match the the function $F(n)$ for every $k$, Im $k \geq 0$, they can be considered as an analytic continuation of $F(n)$ to the lower semispace of the complex $k$ plane. Also, in the case of complex values of $k$, one must identify how the complex square root in $\gamma_m$ is calculated due to the concerns outlined in Appendix A. The branch cut for the square root function in this particular situation must be chosen along the negative imaginary axis.

APPENDIX E

IDENTITIES FOR THE DIRAC DELTA FUNCTION

This appendix contains some useful properties of the Dirac delta function defined as

(E.1)
$$\delta(x) = \begin{cases} +\infty, & x = 0, \\ 0, & x \neq 0, \end{cases}$$

where additionally

(E.2)
$$\int\limits_{-\infty}^{+\infty} \delta(x)dx = 1.$$

The following identities exist for the delta function:

(E.3)
$$f(x_0) = \int\limits_{-\infty}^{+\infty} f(x)\delta(x - x_0)dx,$$

(E.4)
$$\delta(x - x_0) = \frac{1}{2\pi} \int\limits_{-\infty}^{+\infty} e^{ip(x-x_0)}dp,$$

and for its derivative:

(E.5)
$$f'(x_0) = -\int\limits_{-\infty}^{+\infty} f(x)\delta'(x - x_0)dx,$$

(E.6)
$$\delta'(x - x_0) = \frac{i}{2\pi} \int\limits_{-\infty}^{+\infty} pe^{ip(x-x_0)}dp,$$

Here $f(x)$ is an arbitrary function. The identity (E.6) is obtained from (E.4) by calculating its derivative with respect to $x$.

APPENDIX F

LORENTZ-DRUDE MODEL FIT

FOR THE DIELECTRIC PERMITTIVITY OF SILVER

In the generalized Lorentz-Drude model the material response to the electric field is given by the dielectric function

(F.1)
$$\epsilon(\omega) = \epsilon_\infty - \sum_{n=0}^{N} \frac{f_n \omega_p^2}{\omega^2 - \omega_n^2 + i\omega\gamma_n}.$$

Here $\epsilon_\infty$ is the limit of the dielectric permittivity at infinite frequency, $\omega_n$ represent the frequencies of internal resonances, $\gamma_n$ are the damping rates, and $f_n$ are the coefficients that scale the contribution from each term in the sum. The parameters of the Lorentz-Drude model found in [76] provide a good fit to the experimental data, in particular, to the data from [47] in the wavelength range from $0.3\mu$m to $2.1\mu$m.

The best fit parameters are as follows: the dielectric permittivity is $\epsilon_\infty = 1$, the plasma frequency is $\omega_p = 9.01$ eV, the number of terms in the series is $N = 5$, and the rest of the parameters are summarized in the Table F.1 below.

| $n$ | $\omega_n$ (eV) | $\gamma_n$ (eV) | $f_n$ |
|-----|-----------------|-----------------|-------|
| 0   | 0               | 0.048           | 1     |
| 1   | 0.816           | 3.886           | 0.065 |
| 2   | 4.481           | 0.452           | 0.124 |
| 3   | 8.185           | 0.065           | 0.011 |
| 4   | 9.083           | 0.916           | 0.840 |
| 5   | 20.29           | 2.419           | 5.646 |

TABLE F.1. Lorentz-Drude model parameters.

Note: the term $\omega_p$ in (F.1) serves as a fitting parameter; it should not be confused with the actual plasma frequency of a conductor which characterizes the density of the valence electrons and their oscillations.

# REFERENCES

[1] Graf's addition theorem. `http://www.wikiwaves.org/Graf's_Addition_Theorem`, 2009 (accessed October 5, 2017). 120

[2] A small world full of opportunities. *Nat. Mater.* **9** (2010). Editorial. 2, 86

[3] Not so small. *Nat. Photon.* **8** (2014). Editorial. 2, 86

[4] Abramowitz, M., and Stegun, I., Eds. *Handbook of Mathematical Functions With Formulas, Graphs, and Mathematical Tables*, vol. **55** of *Applied Mathematics Series*. Dover, New York, 1970, p. 363. 120

[5] Achenbac, D., Ed. *Wave propagation in elastic solids*. North-Holland, Amsterdam, 1973. 8, 29

[6] Akimov, Y., and Chu, H. Plasmon coupling effect on propagation of surface plasmon polaritons at a continuous metal/dielectric interface. *Phys. Rev. B* **83** (2011). 87, 88, 96

[7] Ash, E., and Paige, E., Eds. *Rayleigh-wave theory and applications*. Springer-Verlag, New York, 1985. 7

[8] Belan, S., and Vergeles, S. Plasmon mode propagation in array of closely spaced metallic cylinders. *Opt. Mat. Express* **5** (2015). 48, 58, 63, 65

[9] Bobrovnitskii, Y. Orthogonality relation for Lamb waves. *Soviet Phys. - Acoustics* **18** (1973). 29

[10] Bozhko, A., García-Chocano, V., Sánchez-Dehesa, J., and Krokhin, A. Redirection of sound in straight fluid channel with elastic boundaries. *Phys. Rev. B* **91** (2015). 46

[11] Brandstetter-Kunc, A., Weick, G., Downing, C., Weinmann, D., and Jalabert, R. Nonradiative limitations to plasmon propagation in chains of metallic nanoparticles. *Phys. Rev. B* **94** (2016). 48

[12] Brongersma, M., Hartman, J., and Atwater, H. Electromagnetic energy transfer and switching in nanoparticle chain arrays below the diffraction limit. *Phys. Rev. B* **62** (2000). 48

[13] Cai, W., and Shalaev, V. *Optical Metamaterials: Fundamentals and Applications.* Springer, New York, 2010. 2

[14] Chen, X., et al. Squeezing millimeter waves through a single, nanometer-wide, centimeter-long slit. *Scientific Reports* **4** (2014). 22

[15] Christensen, J., Fernandez-Dominguez, A., de Leon-Perez, F., Martín-Moreno, L., and García-Vidal, F. Collimation of sound assisted by acoustic surface waves. *Nat. Phys.* **3** (2007). 6

[16] Christensen, J., Martin-Moreno, L., and García-Vidal, F. Theory of resonant acoustic transmission through subwavelength apertures. *Phys. Rev. Lett.* **101** (2008). 1, 6

[17] Christensen, J., Martín-Moreno, L., and García-Vidal, F. Enhanced acoustical transmission and beaming effect through a single aperture. *Phys. Rev. B* **81** (2010). 6

[18] Compaijen, P., Malyshev, V., and Knoester, J. Surface-mediated light transmission in metal nanoparticle chains. *Phys. Rev. B* **87** (2013). 48

[19] Crandall, I. *Theory of vibrating systems and sound.* D. Van Nostrand, New York, 1926. 55

[20] Cummer, S., Christensen, J., and Alú, A. Controlling sound with acoustic metamaterials. *Nat. Rev. Mater.* **1** (2016). 48

[21] Ebbesen, T., Lezec, H., Ghaemi, H., Thio, T., and Wolff, P. Extraordinary optical transmission through sub-wavelength hole arrays. *Nature* **391** (1998). 1, 3, 6

[22] Estrada, H., Bravo, J., and Meseguer, F. High sound screening in in low impedance slit arrays. *New Journal of Physics* **13** (2011). 6, 9

[23] Estrada, H., et al. Extraordinary sound screening in perforated plates. *Phys. Rev. Lett.* **101** (2008). 1, 6, 9

[24] Estrada, H., et al. Angle-dependent ultrasonic transmission through plates with sub-wavelength hole arrays. *Phys. Rev. Lett.* **102** (2009). 6, 9

[25] Evans, D., and Porter, R. Trapping and near-trapping by arrays of cylinders in waves. *Journal of Engineering Mathematics* **35** (1999). 63, 65

[26] Folk, R., and Herczynski, A. Solutions of elastodynamic slab problems using a new orthogonality condition. *J. Acoust. Soc. Am.* **80** (1986). 29

[27] Fredholm, E. Sur une classe d'équations fonctionnelles. *Acta Math.* **27** (1903). 97

[28] Friedel, J. The distribution of electrons round impurities in monovalent metals. *Phil. Mag.* **43** (1951), pp. 153–189. 87

[29] García-Chocano, V. *New devices for noise control and acoustic cloaking*. PhD thesis, Universitat Politècnica de València, Valencia, Spain, 2015. 84

[30] García-Chocano, V., et al. Resonant coupling of Rayleigh waves through a narrow fluid channel causing extraordinary low acoustic transmission. *J. Acoust. Soc. Am.* **132** (2012). 8, 17, 30, 38

[31] García-Chocano, V., López-Rios, T., Krokhin, A., and Sánchez-Dehesa, J. Resonant excitation of coupled Rayleigh waves in a short and narrow fluid channel clad between two identical metal plates. *AIP Advances* **1** (2011). 3, 7

[32] García-Chocano, V., and Sánchez-Dehesa, J. Anomalous sound absorption in lattices of cylindrical perforated shells. *Appl. Phys. Lett.* **106** (2015). 3, 49, 50, 52, 61, 74, 78, 84

[33] García-Chocano, V. M., Cabrera, S., and Sánchez-Dehesa, J. Broadband sound absorption by lattices of microperforated cylindrical shells. *Appl. Phys. Lett.* **101** (2012). 52, 56, 61

[34] García-Vidal, F., Martin-Moreno, L., Ebbesen, T., and Kuipers, L. Light passing through subwavelength apertures. *Rev. Mod. Phys.* **82** (2010). 7

[35] Gibson, E., Pennybacker, M., Maimistov, A., Gabitov, I., and Litchinitser, N. Resonant absorption in transition metamaterials: parametric study. *J. Opt.* **13** (2010). 87

[36] Ginzburg, V. *Propagation of Electromagnetic Waves in Plasma*. Gordon and Breach, New York, 1961. 86, 94

[37] Glass, N., and Maradudin, A. Leaky surface-elastic waves on both flat and strongly corrugated surfaces for isotropic, nondissipative media. *J. Appl. Phys.* **54** (1998). 7, 115

[38] Gumbs, G., Iurov, A., Huang, D., and Pan, W. Tunable surface plasmon instability leading to emission of radiation. *Journal of Applied Physics* **118(5)** (2015). 2

[39] Guo, Y., Allam, S., and Åbom, M. Acoustical study of micro-perforated plates for vehicle applications. *SAE Technical Paper No. 2009-01-2037* (2009). 55

[40] Haberman, M., and Guild, M. Acoustic metamaterials. *Phys. Today* **69(6)** (2016), p. 42. 48

[41] Hou, B., et al. Tuning Fabry-Perot resonances via diffraction evanescent waves. *Phys. Rev. B* **76** (2007). 6

[42] Huang, H., and Sun, C. Wave attenuation in an acoustic metamaterial with negative effective mass density. *New J. Phys.* **11** (2009). 48

[43] Huang, H., and Sun, C. Anomalous wave propagation in one-dimensional acoustic metamaterial having simaltaneously negative mass density and Young's modulus. *J. Acoust. Soc. Am.* **132** (2012). 48

[44] Ingard, U. On the theory and design of acoustic resonators. *J. Acoust. Soc. Am.* **25** (1953). 55

[45] Ingebrigtsen, K., and Tonning, A. Elastic surface waves in crystals. *Phys. Rev.* **184** (1969). 115

[46] Jia, H., Xie, Y., Liu, H., and Zhong, Y. Analytical model for the excitation of leaky surface plasmon polaritons in the attenuated total reflection configuration. *J. Opt.* **18** (2016). 117

[47] Johnson, P., and Christy, R. Optical constants of the noble metals. *Phys. Rev. B* **6** (1972). 102, 127

[48] Kaina, N., Lemoult, F., Fink, M., and Lerosey, G. Negative refractive index and acoustic superlens from multiple scattering in single negative metamaterials. *Nature* **525** (2015). 48

[49] Kelders, L., Allard, J., and Lauriks, W. Ultrasonic surface waves above rectangular-groove gratings. *J. Acoust. Soc. Am.* **103** (1998). 6

[50] Khurgin, J. How to deal with the loss in plasmonics and metamaterials? *Nat. Nanotech.* **10** (2015). 2

[51] Khurgin, J., Tsai, W.-Y., Tsai, D., and Sun, G. Landau damping and limit to field confinement and enhancement in plasmonic dimers. *ACS Photonics* **4**(11) (2017). 2

[52] Kinsler, L., Frey, A., Coppens, A., and Sanders, J. *Fundamentals of Acoustics*. John Wiley & Sons, New York, 1982. 5

[53] Landau, L., Pitaevskii, L., Kosevich, A., and Lifshitz, E. *Theory of Elasticity (Third Edition)*, vol. **7** of *Course of Theoretical Physics*. Pergamon Press, New York, 1986. 11, 14, 16

[54] Landau, L., Pitaevskii, L., and Lifshitz, E. *Electrodynamics of Continuous Media (Second Edition)*, vol. **8** of *Course of Theoretical Physics*. Pergamon Press, New York, 1984. 89, 96

[55] Lim, T., and Farnell, G. W. Character of pseudo surface waves on anisotropic crystals. *J. Acoust. Soc. Am.* **45** (1969). 115

[56] Litchinitser, N., Maimistov, A., Gabitov, I., Sagdeev, R., and Shalaev, V. Metamaterials: electromagnetic enhancement at zero-index transition. *Opt. Lett.* **33**(20) (2008). 87

[57] Lloyd, P., and Redwood, M. Wave propagation in a layered plate composed of two solids with perfect contact, slip, or a fluid layer at their interface. *Acustica* **16** (1965). 13

[58] Lu, M.-H., et al. Extraordinary acoustic transmission through a 1D grating with very narrow apertures. *Phys. Rev. Lett.* **99** (2007). 1, 6

[59] Lyon, R. Response of an elastic plate to localized driving forces. *J. Acoust. Soc. Am.* **27** (1955). 29

[60] Maa, D.-Y. Theory and design of microperforated panel sound absorbing constructions. *Sci. Sin.* **18** (1975). 53

[61] Maa, D.-Y. Potential of microperforated panel absorber. *J. Acoust. Soc. Am.* **104**(5) (1998). 53, 54

[62] Maier, S. *Plasmonics: Fundamentals and Applications*. Springer, New York, 2007. 2

[63] Maier, S., et al. Local detection of electromagnetic energy transport below the diffraction limit in metal nanoparticle plasmon waveguides. *Nat. Mater.* **2** (2003). 48

[64] Maradudin, A., and Simonsen, I. Rayleigh and Wood anomalies in the diffraction of acoustic waves from the periodically corrugated surface of an elastic medium. *Low Temperature Physics* **42** (2016). 74, 115

[65] Maradudin, A., Simonsen, I., and Zierau, W. Leaky surface electromagnetic waves on a high-index dielectric grating. *Opt. Lett.* **41(10)** (2016). 74, 115

[66] Markel, V., and Sarychev, A. Propagation of surface plasmons in ordered and disordered chains of metal nanospheres. *Phys. Rev. B* **75** (2007). 48

[67] Martin, T., Layman, C., Moore, K., and Orris, G. Elastic shells with high-contrast material properties as acoustic metamaterial components. *Phys. Rev. B* **85** (2012). 49

[68] Maystre, D. Theory of Wood's anomalies. In *Plasmonics*, S. Enoch and N. Bonod, Eds., vol. **167** of *Springer Series in Optical Sciences*. Springer-Verlag, Berlin, 2012, p. 39. 78

[69] McPhedran, R., and Maystre, D. On the theory and solar application of inductive grids. *Appl. Phys.* **14** (1977). 7

[70] Moitra, P., et al. Realization of an all-dielectric zero-index optical metamaterial. *Nat. Photon.* **7** (2013). 86

[71] Norris, A., and Luo, H. Acoustic radiation and reflection from a periodically perforated rigid solid. *J. Acoust. Soc. Am.* **82** (1987). 6, 9

[72] Pendry, J. Negative refraction makes a perfect lens. *Phys. Rev. Lett.* **85** (2000). 86

[73] Prigogine, I., and Rice, S., Eds. *Aspects of the study of surfaces*, vol. **27** of *Advances in Chemical Physics*. Wiley, New York, 1974. 87

[74] Quinten, M., Leitner, A., Krenn, J., and Aussenegg, F. Electromagnetic energy transport via linear chains of silver nanoparticles. *Opt. Lett.* **23** (1998). 3, 48

[75] Raether, H. *Surface Plasmons on Smooth and Rough Surfaces and on Gratings*, vol. 11

of *Springer Tracts in Modern Physics*. Springer-Verlag, Berlin Heidelberg, 1988. 104, 105

[76] Rakić, A., Djurišic, A., Elazar, J., and Majewski, M. Optical properties of metallic films for vertical-cavity optoelectronic devices. *Appl. Opt. 37(22)* (1998). 102, 127

[77] Rayleigh, Baron, J. W. S. On waves propagated along the plane surface of an elastic solid. *Proc. London Math. Soc. 17* (1887). 5, 13

[78] Rayleigh, Baron, J. W. S. *Theory of sound (Second Edition)*. Dover Publications, New York, 1945. 54

[79] Sainidou, R., and Stefanou, N. Guided and quasiguided elastic waves in phononic crystal slabs. *Phys. Rev. B 73* (2006). 7

[80] Sainidou, R., Stefanou, N., Psarobas, I., and Modinos, A. Scattering of elastic waves by a periodic monolayer of spheres. *Phys. Rev. B 66* (2002). 58

[81] Sánchez-Dehesa, J., et al. Noise control by sonic crystal barriers made of recycled materials. *J. Acoust. Soc. Am. 129* (2011). 52

[82] Sánchez-Pérez, J., et al. Sound attenuation by a two-dimensional array of rigid cylinders. *Phys. Rev. Lett. 80* (1998). 50, 76

[83] Schilling, J. Fundamental optical physics: The quest for zero refractive index. *Nat. Photon. 5(449)* (2011). 86

[84] Schuller, J., et al. Plasmonics for extreme light concentration and manipulation. *Nat. Mater. 9* (2010). 2, 86, 94

[85] Seo, M., et al. Terahertz field enhancement by a metallic nano slit operating beyond the skin-depth limit. *Nat. Photon. 3* (2009). 22

[86] Shalaev, V. Optical negative-index metamaterials. *Nat. Photon. 1(41)* (2007). 86

[87] Shockley, W. On the surface states associated with a periodic potential. *Phys. Rev. 56(4)* (1939). 2

[88] Spence, R. The diffraction of sound by circular disks and apertures. *J. Acoust. Soc. Am. 20* (1948). 5

[89] Stockman, M. Nanoplasmonics: past, present, and glimpse into future. *Opt. Express* **19** (2011). 2

[90] Sturman, B., Podivilov, E., and Gorkunov, M. Eigenmodes for metal-dielectric light-transmitting nanostructures. *Phys. Rev. B* **76** (2007). 8

[91] Sturman, B., Podivilov, E., and Gorkunov, M. Transmission and diffraction properties of a narrow slit in a perfect metal. *Phys. Rev. B* **82** (2010). 7

[92] Sun, G., Khurgin, J., and Soref, R. Practicable enhancement of spontaneous emission using surface plasmons. *Appl. Phys. Lett.* **90** (2007). 2

[93] Tamm, I. On the possible bound states of electrons on a crystal surface. *Phys. Z. Soviet Union* **1: 733** (1932). 2

[94] Tinti, S. Diffraction by a thick slitted screen. *J. Acoust. Soc. Am.* **65** (1979). 5

[95] Titovich, A., and Norris, A. Tunable cylindrical shell as an element in acoustic metamaterial. *J. Acoust. Soc. Am.* **136** (2014). 49

[96] Titovich, A., and Norris, A. Acoustic scattering from an infinitely long cylindrical shell with an internal mass attached by multiple axisymmetrically distributed stiffeners. *J. Sound. Vib.* **338** (2015). 49

[97] Titovich, A., and Norris, A. Acoustic Poisson-like effect in periodic structures. *J. Acoust. Soc. Am.* **139** (2016). 49, 50, 77

[98] Tserkezis, C., Papanikolaou, N., Almpanis, E., and Stefanou, N. Tailoring plasmons with metallic nanorod arrays. *Phys. Rev. B* **80** (2009). 48

[99] Twersky, V. Elementary function representation of the Schlömilch series. *Arch. Ration. Mech. Anal.* **8** (1961). 65, 122

[100] van der Aa, B., and Forssén, J. Upward refraction of sound propagating outdoors by a graded index sonic crystal noise barrier. *Applied Acoustics* **74** (2013). 50

[101] van der Aa, B., and Forssén, J. Scattering by an array of perforated cylinders with a porous core. *J. Acoust. Soc. Am.* **136** (2014). 56

[102] Veselago, V. The electrodynamics of substances with simultaneously negative values of $\epsilon$ and $\mu$. *Sov. Phys. Usp.* **10(509)** (1968). 86

[103] Viktorov, I., Ed. *Rayleigh and Lamb Waves: Physical Theory and Applications.* Plenum, New York, 1967. 7

[104] Ward, G., Hibbins, A., Sambles, J., and Smith, J. Acoustic transmission through compound subwavelength slit arrays. *Phys. Rev. B* **94** (2016). 50, 76

[105] Weber, W., and Ford, G. Propagation of optical excitations by dipolar interactions in metal nanoparticle chains. *Phys. Rev. B* **70** (2004). 48

[106] Wilson, G., and Soroka, W. Approximation to the diffraction of sound by a circular aperture in a rigid wall of finite thickness. *J. Acoust. Soc. Am.* **37** (1965). 5

[107] Zakharov, D. Dirichlet-Neumann conditions and the orthogonality of three-dimensional guided waves in layered solids. *Computational Mathematics and Mathematical Physics* **50** (2010). 29

[108] Zayats, A., Smolyaninov, I., and Maradudin, A. Nano-optics of surface plasmon polaritons. *Physics Reports* **408** (2005). 87, 90, 91, 92

[109] Zhang, X. Acoustic resonant transmission through acoustic gratings with very narrow slits: Multiple-scattering numerical simulations. *Phys. Rev. B* **71** (2005). 6

[110] Zhang, Y., and Wei, P. The scattering of acoustic wave by a chain of elastic spheres in liquid. *Journal of Vibration and Acoustics* **136** (2004). 58

[111] Zhou, Y., et al. Acoustic surface evanescent wave and its dominant contribution to extraordinary acoustic transmission and collimation of sound. *Phys. Rev. Lett.* **104** (2010). 6